Average Strain Estimation for Ultrasound Elastography Using Exponentially Weighted Nearest Neighbors

A thesis submitted to the Department of Electrical and Electronic Engineering

of

Bangladesh University of Engineering and Technology

in partial fulfillment of the requirement for the degree of

MASTER OF SCIENCE IN ELECTRICAL AND ELECTRONIC ENGINEERING

by

Mohammad Arafat Hussain

DEPARTMENT OF ELECTRICAL AND ELECTRONIC ENGINEERING

BANGLADESH UNIVERSITY OF ENGINEERING AND TECHNOLOGY

2013

The thesis entitled **"Average Strain Estimation for Ultrasound Elastography Using Exponentially Weighted Nearest Neighbors"** submitted by Mohammad Arafat Hussain, Student No.: 0411062235, Session: April, 2011 has been accepted as satisfactory in partial fulfillment of the requirement for the degree of MASTER OF SCIENCE IN ELECTRICAL AND ELECTRONIC ENGINEERING on April 23, 2013.

BOARD OF EXAMINERS

1. —————————————————

   (Dr. Md. Kamrul Hasan)   **Chairman**
   Professor   (Supervisor)
   Department of Electrical and Electronic Engineering
   Bangladesh University of Engineering and Technology
   Dhaka - 1000, Bangladesh

2. —————————————————

   (Dr. Pran Kanai Saha)   **Member**
   Professor and Head   (Ex-officio)
   Department of Electrical and Electronic Engineering
   Bangladesh University of Engineering and Technology
   Dhaka - 1000, Bangladesh

3. —————————————————

   (Dr. Mohammed Imamul Hassan Bhuyian)   **Member**
   Associate Professor
   Department of Electrical and Electronic Engineering
   Bangladesh University of Engineering and Technology
   Dhaka - 1000, Bangladesh

4. —————————————————

   (Dr. Sharmin Akter Rupa, *MBBS, M.Phil., FCPS*)   **Member**
   Associate Professor   (External)
   Department of Radiology and Imaging
   Enam Medical College and Hospital
   Savar, Dhaka - 1342, Bangladesh

CANDIDATE'S DECLARATION

It is hereby declared that this thesis or any part of it has not been submitted elsewhere for the award of any degree or diploma.

Signature of the candidate

_____

(Mohammad Arafat Hussain)

DEDICATION

To my beloved family,
And my teacher, Prof. Dr. Md. Kamrul Hasan

ACKNOWLEDGEMENTS

I would like to commence this thesis by expressing my gratitude towards Almighty Allah, Who blessed us with His endless mercy, Filled us with diligence and perseverance, and most importantly, the kindness in my honorable supervisor, Dr. Md. Kamrul Hasan, Professor, Department of Electrical and Electronic Engineering, Bangladesh University of Engineering and Technology (BUET) who provided me with the necessary support I required. I am greatly indebted to him for his guidance, limitless patience and constant support that was critical for completing this research. It was an honor working with him.

I am grateful to the Head of the department of Electrical and Electronic Engineering, BUET, for all time lab facilities in the DSP research Lab which contributed greatly to my research works of this thesis.

And I thank my parents for teaching me the meaning of life, keeping me steady in this path with their affection that instilled the spirit of this work.

Contents

List of Figures

xi

List of Tables

ABSTRACT

Strain imaging, also known as elastography, is an emerging medical imaging modality for detection and diagnosis of pathologic soft tissue via its stiffness measurement. Assuming the tissue stiffness as a continuous function in a physical proximity, a cost function maximization based approach is adopted in this thesis to develop a gradient-based (GBASE) and direct average strain estimation (DASE) techniques for high quality average strain imaging. The cost function is defined from exponentially weighted neighboring window pre- and post-compression radio-frequency (RF) normalized cross-correlation (NCC) peaks in the lateral (for GBASE) or in both the axial and the lateral (for DASE) directions to estimate an average strain. The proposed techniques are robust to decorrelation noise and have a built-in smoothing feature to ensure controlled continuity in displacement/strain in neighborhood tissues.

It is also seen that with increased stress, the non-axial motions of tissue elements increase that result in noisier strain images. At high strain, envelope of the RF signal exhibits robustness to this signal decorrelation though the precision of the estimated strain is much worse compared to that using the RF signals. In this thesis, we also propose a novel approach for robust strain estimation by combining weighted RF NCC and envelope NCC functions. An applied strain dependent piecewise-linear-weight is used to combine them. In addition, we introduce non-linear diffusion filtering to further enhance the resulting strain image.

While strain continuity can be ensured using the proposed weighted nearest neighbor approach or by using other regularization/smoothing based techniques, the lesion edge blurring cannot be prevented as they are not intelligent enough to detect and preserve edges while smoothing. In this thesis, a novel approach with built-in lesion edge preservation technique is proposed for direct average strain imaging. An edge detection scheme, conventionally used in diffusion filtering is modified here for extracting edge information while ensuring strain continuity. Based on the extracted edge information, lesion edges are preserved by modifying the strain determining cost function in the proposed DASE method in such a way that only the NCC peaks of similar stiffer region to that of the interrogative tissue point are incorporated into it.

The proposed algorithms demonstrate significantly better performance, in terms of both quantitative and qualitative indices, than the other reported strain estimation techniques for a wide range of applied strain in finite element modeling (FEM) simulation, phantom experiment, and also with *in vivo* breast data.

Chapter 1

Introduction

1.1 Background of Ultrasound Strain Imaging

1.1.1 Motivation

The term "elastography" is first introduced by Professor Jonathan Ophir in 1991 [1]. It refers to the method of imaging the mechanical property (i.e., elastic modulus) of tissue. The tissue elasticity change has deep correlation with the pathology change and clinicians practices manual palpation to feel for stiff lumps since 400 BC [2]. In recent years, digital palpation in terms of imaging technology have paved the way for accurate quantitative visualization of the deep-lying structures' stiffness. The stiffness measuring technique has been being used in clinical diagnosis in many anatomical areas. It is now well established that an elastogram may distinguish between benign and malignant masses, and categories among different types of malignancy [3]–[8]. In addition, elastography often perform better in accurate diagnosis than the conventional B-mode ultrasound imaging [9]. The novel application aims include discriminating between complex cysts and malignant breast lesions without biopsy [10], observing atherosclerosis [11], [12], detecting deep vein thrombosis [13], assessing the skin pathologies [14] and evaluating myocardial fitness [15]. Hence, most of the ultrasound machine manufacturers now offer a form of elastography imaging in their flagship ultrasound systems.

1.1.2 Techniques in Elastography

Elastography involves estimation of local tissue displacement subject to some sort of applied external mechanical pressure or stress. The tissue deforming patterns provide information about the mechanical properties of the investigating tissue. The elastography techniques are loosely categorized according to how the stress is applied and how the tissue deformation is measured. For example, stress can be applied externally by means of the probe [1] or internally via acoustic radiation force [16]. On the other hand, tissue deformation can be measured using magnetic resonance imaging (MRI) [17] or ultrasound [1]. In quasi-static ultrasound elastography, the deformation is caused by applying external pressure on the tissue surface with the transducer, and estimated using ultrasound backscatter echoes. Such techniques are known by various commercial names as eSieTouch (Siemens Healthcare, Malvern, PA), ElastoQ (Toshiba Medical Systems, Tustin, CA), Elastoscan (Samsung Medison, Samsung Electronics Ltd., Suwon, South Korea) and simply elastography (GE Healthcare, Waukesha, WI; Philips Healthcare, Andover, MA; and Ultrasonix Medical Corporation, BC, Canada). Though, there are more quantitative techniques based on shear wave speed [18], quasi-static elastography is a qualitative technique that is unsuitable for measuring absolute tissue stiffness. However, it is possible to relate stiffness of a lesion to that of the background tissue. In addition, it has a high spatial resolution, is real time, and does not require any modifications to conventional ultrasound hardware. For elastogram generation, B-mode images are steadily acquired, with a slight varying pressure applied on the tissue surface by means of the ultrasound probe. A typical quasi-static ultrasound elastography process is shown in Fig. 1.1. RF data are acquired with and without external pressure applied vertically on the tissue surface. However, for scanning up to 4 or 5 cm deep, physiological tremor is often enough to generate this pressure variation. Since the probe is in continuous motion but with sufficiently low velocity and acceleration, hence the term "quasi-static" is derived. Typically, the RF ultrasound echo signals from each frame are compared with the previous one in order to estimate the tissue displacement at multiple locations along each scan-lines. The axial strain is then estimated by taking the gradient of this deformation map. When an elastogram is
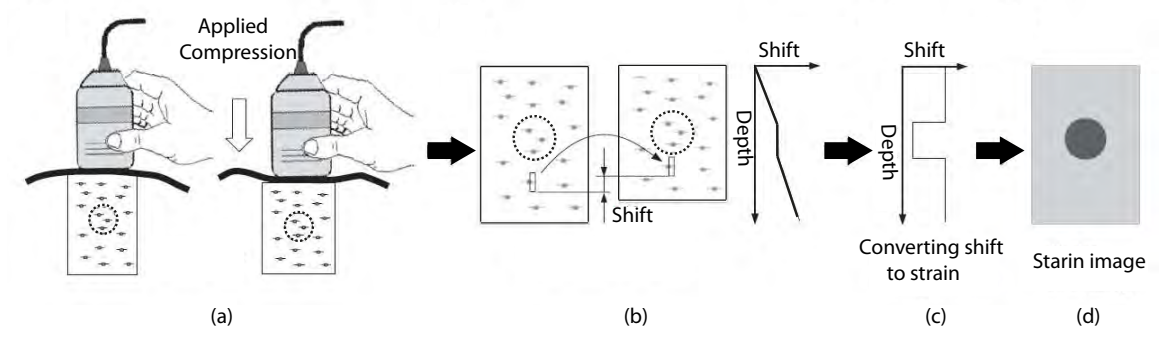
Figure 1.1: Illustration of the quasi-static elastography technique. (a) The tissue is scanned with a traditional ultrasound probe, with no and a little compression applied vertically. Note that the dashed circle is meant to be stiffer than the background material. (b) Tissue deformation in the axial direction is estimated throughout the ultrasound image. (c) Gradient operation along the axial direction results an estimate of axial strain. (d) A strain image with the indication of black as stiffer and white as softer.

displayed, it is nothing but a processed version of this strain data mapped with a grey scale. Stiffer regions are compressed less when subject to pressure and hence exhibit lower strain values.

1.1.3 Mechanics of Tissue

As the mechanics of tissue are very complex, therefore, various assumptions have to be made in order to relate measurable values to a mechanical material property. Sometimes, these assumptions introduce various artifacts into the strain image, which are often incorrectly interpreted. The assumed linear viscoelastic model [19]–[21] relates stress to strain by describing anisotropic material properties with respect to time. This properties are often related to biochemical changes in the tissue [22]. Due to the quasi-static nature of the scanning process, the viscous effects can be ignored that gives rise to the linear elastic model [19], [20]. Thereafter, living tissues are generally assumed to be isotropic that paves the way to model the stress and strain as a simple function of the Young modulus E and the Poisson ratio ν. Typically, it is assumed that ν is close

to 0.5 in most tissue, leaving E alone to characterize an incompressible, isotropic material's stiffness. It is reported that E accounts almost entirely for the useful information accessible by manual palpation [23], [24]. Even with this single parameter model, estimating E is still problematic as it relies on both stress and strain, and the stress field is often not known. However, even though the strain image does not directly relate to stiffness, it is apparent in literature that the strain in the hard and soft lesions has good contrast and high spatial accuracy. In fact, almost all elastograms are actually the versions of their respective strain images, rather than true stiffness images.

1.1.4   Quasi-static Elastography: Overview

The most vital part of an elastographic imaging system is the algorithm used to estimate tissue deformation between two frames of ultrasound RF data. The transducer movement in quasi-static elastography is seldom purely in the axial direction. In addition, the axial deformation contains most of the useful mechanical information, and it can be measured more accurately than the out of plane motions [25]. Hence, lateral or elevational tracking only can further aid in improving the estimation of the axial deformation.

There are a number of types of displacement estimators [26], [27]. Most strain estimators are concerned with the matching of blocks of RF ultrasound data by relative movement of them until some similarity metric is optimized. Correlation estimation was the first such metric proposed [1], [28] and remains the most widely used one. Other metrics include sum of absolute differences (SAD) [29], [30], sum of squared differences (SSD) [31], correlation phase [32]–[34], and weighted phase separation [35]. For accurate strain estimation, displacement must be estimated to sub-sample precision, either by interpolating the similarity metric before finding the peak [31], [33], [36] or by interpolation of the RF data before the matching process [35], [37]. In phase-based matching processes, optimal matching is understood by the zero correlation phase [32] or zero phase separation [35]. If a non-zero result arises, then the knowledge of the transducer's center frequency allows a rapid iteration towards the more optimal matching provided that the initial alignment is within half a wavelength

of the zero-phase shift [33]. Moreover, an inaccurate center frequency estimate does not affect the accuracy of the displacement estimate but the speed of convergence is a bit slowed [33].

In cross-correlation-based techniques, correlation maximization can be achieved by exhaustive search process [38] or using an uphill search from a predicted initial displacement. The initial prediction can be achieved from the inter-window continuity, either by dynamic programming [39] or by minimizing a global cost function that penalizes discontinuous displacements [31], [40], or by tracking the displacements among consecutive windows [35], [41].

Because of the out-of-plane motion during the application of the external pressure, pre- and post-compression RF windows can match poorly. Several techniques have been developed to increase the correlation between the windows. These can be variously referred to as 'temporal stretching' [42], 'adaptive stretching' [36], and 'companding' [30]. Companding increases the precision of deformation data at a huge computational cost. The main advantage of this approach is not so much the increase in correlation, but the ability to match each window at all points simultaneously [43]. However, the performance of all displacement estimators varies with the relative strain between the pre- and post-deformation data.

1.1.5 Categories of Quasi-static Elastography Techniques and Their Limitations

Visualization of discriminant elastic properties in the art of pathological diagnosis of tissue abnormality is performed in the form of elastography. In quasi-static elasticity imaging, ultrasound echoes are acquired before and after applying gentle external pressure on the surface, typically by means of an ultrasound transducer. Different algorithms are developed to calculate strain from these pre- and post-compression echoes. These strain-estimation algorithms can be broadly categorized into 1) gradient-based strain estimation [1], [41], [44]–[47], and 2) direct strain estimation [36], [48]–[50]. In most cases, gradient-based techniques are developed with a target of real-time imaging

whereas direct strain estimation techniques focus on the development of high-quality strain image at the cost of increased computational complexity. However, RF echo decorrelation and noise degrade the performance of the algorithms for both categories.

The gradient-based strain estimation relies on calculating displacement from the cross-correlation between pre- and post-compression RF windowed echo segments. It always introduces a significant amount of noise in the strain due to small window selection and/or large overlap between successive choice of windows of the same echo line [36]. According to [51], equal or greater than 90% overlap between successive windows can generate strain image of high axial resolution but it also introduces noise in the form of "worm" artifacts [48]. High frequency noise is generally amplified by the gradient-based techniques [47], [49]. Temporal stretching of post-compression echo improves the cross-correlation between pre- and post-compression signals by minimizing the strain noise [45], but it is effective only in low strain [42] and has a high probability to miss the hard lesion. Before gradient operation, a smoothing technique based on least-squares-based linear regression [52] or least-squared-error-based smoothing-spline [47] can be applied on displacement matrix. Median filtering is also effective before gradient operation to remove the shot noise and some false peak noise. For smoothing the strain image, some recent literature [39]–[41], [53] proposes to consider the previous windows or sample characteristic values in computing the present displacement value to maintain continuity of strain. But these smoothing algorithms are not intelligent enough to detect and preserve the lesion edge.

In direct strain estimation, the strain is directly calculated from a pair of pre- and post-compression RF-echo segments in 1) time domain [36] or 2) in frequency domain [49], [50]. The adaptive stretching-based direct strain estimation is better in the time domain than in the frequency domain. Direct spectral strain estimation is a non-coherent technique because it ignores the signal phase. But it is robust on the undesired scanning motion from unstable hand-held probe and undesired internal tissue motion [54]. It is considered that the post-compression echo is a compressed and delayed version of its counterpart pre-compression echo [36]. This signal model inspires the idea of stretching the post-compression echo or shifting the pre-compression signal

spectrum before the cross-correlation calculation. These techniques can generate strain image with higher signal-to-noise ratio (SNR) than the gradient-based techniques, but the elastogram produced by the direct strain estimation techniques has no strain continuity guarantee among neighboring pixels of a particular area of the strain image.

Some reported strain estimators use only the envelope signal or the RF signal in conjunction with the envelope for strain estimation [55]-[58]. In [55], a theoretical framework is discussed for envelope cross-correlation based strain estimation by characterizing the noise performance. [56] uses the pre- and post-compression envelope window cross-correlation to calculate the sparse displacement (seed) in the tissue at the preliminary stage and in the subsequent stages the primary seeds are used to track the displacement in a gradual finer grid by using envelope cross-correlation. In [57], down-sampled 2-dimensional envelope signal is used to track the tissue motion upon physical compression and using the tracking, strain is calculated from the 2-dimensional pre- and post compression rf echo cross-correlation. But according to [55], strain estimation variance is high and SNRe is low for the envelope signal compared to that of the RF signal at low strain. So, the preliminary estimated seeds or tracking parameters used in [56] and [57] may be misleading at low strain. [58] uses RF autocorrelation to find phase shift followed by unwrapping it by the extracted information from envelope cross-correlation.

1.2 Objective of This Thesis

The objectives of this thesis are:

1. To develop time domain techniques for direct and gradient-based average strain estimation using the exponentially weighted nearest neighbors. Unlike as in the conventional algorithms, the continuity of estimated strain will be ensured without using any prior estimate of the displacement or strain.

2. To develop an improved approach for robust strain estimation by combining the RF normalized cross-correlation (NCC) and envelope NCC functions in a novel way. An applied strain-dependent piecewise-linear-weight will be formulated for mixing the two functions.

3. To develop a new approach with built-in lesion edge preservation technique for high quality direct average strain imaging. Here, lesion edges will be detected and preserved while ensuring the strain continuity among the neighboring tissue points.

The developed methods are expected to be more robust for a wide range of applied strain values than the other reported time domain techniques for elastography. Because of robustness to signal decorrelation, the masses with low stiffness can be viewed in the strain image and the lesion boundary can be clearly identified compared with the other methods.

1.3   Organization of This Thesis

This thesis consists of six chapters. Chapter 1 gives a brief description about the motivation and background of the quasi-static elastography. This chapter also discusses the objective of the thesis.

Chapter 2 consists of brief descriptions of some previous strain imaging techniques.

In Chapter 3, we present two time domain techniques for direct and gradient-based average strain estimation using the exponentially weighted nearest neighbors. Different from the conventional algorithms, here, the continuity of estimated strain is ensured without using any prior estimate of the displacement or strain. This chapter also presents the efficacy and performance comparison of these developed methods with the other reported techniques.

In Chapter 4, we describe an improved approach for robust strain estimation by combining the RF NCC and envelope NCC functions. An applied strain-dependent piecewise-linear-weight is formulated for mixing these two functions. The efficacy and performance of the method is compared with that of other reported techniques.

We present a new approach with built-in lesion edge preservation technique for high quality direct average strain imaging in chapter 5. Here, lesion edges are detected and preserved while ensuring the strain continuity among the neighboring tissue points. The performance comparison among the proposed and other comparing techniques are also presented here.

Chapter 6 concludes the thesis by presenting the overall view of the thesis and pointing out some scope for future improvements.

Chapter 2

Previous Strain Imaging Techniques: Literature Review

2.1 Introduction

Elasticity imaging is an emerging medical diagnostic tool for displaying mechanical properties of biological tissues. It is well recognized by medical practitioners that tissue mechanical properties such as stiffness change significantly with changes in tissue pathology. For example, cancerous tissues may be orders of magnitude stiffer than the surrounding normal tissues [3]. Stiffness can be estimated by sophisticated techniques such as elastography, which is showing great promise in the detection and/or characterization of breast and prostate tumors [1], [3], [44], [45], liver cirrhosis [59], and vascular plaques [60]. The strain image is typically computed as the spatial gradient of local tissue displacements [1], [41], [44]–[47]. Other approaches estimate strain directly from the pre- and post-compression RF echo waveforms or spectra [36], [48]–[50].

The gradient-based strain estimation relies on calculating displacement from the cross-correlation between pre- and post-compression RF windowed echo segments. The strain is then computed from the derivative of the displacement field. In direct strain estimation, the strain is directly calculated from a pair of pre- and post-compression RF echo segments in 1) time domain [36] or 2) in frequency domain [49], [50]. The

adaptive stretching-based direct strain estimation is better in the time domain than in the frequency domain. Direct spectral strain estimation is a non-coherent technique because it ignores the signal phase. But it is robust on the undesired scanning motion from unstable hand-held probe and undesired internal tissue motion [54]. It is considered that the post-compression echo is a compressed and delayed version of its counterpart pre-compression echo [36]. This signal model inspires the idea of stretching the post-compression echo or shifting the pre-compression signal spectrum before the cross-correlation calculation.

Some reported strain estimators use only the envelope signal or the RF signal in conjunction with the envelope for strain estimation [55]–[58]. [55] discuss a theoretical framework for envelope cross-correlation based strain estimation by characterizing the noise performance and demonstrates a composite strain filter approach to increase the dynamic range in the elastogram by using a combination of RF and envelope signals to estimate strain.

2.2 Direct Strain Estimation Techniques

2.2.1 Adaptive Strain Estimation [36]

The simplified 1-D model of the backscattered ultrasound RF signals before and after compression are given by:

$$r_1(t) = s_1(t) + v_1(t) = s(t) * p(t) + v_1(t), \tag{2.1}$$

$$r_2(t) = s_2(t) + v_2(t) = s\left(\frac{t}{a} - t_0\right) * p(t) + v_2(t), \tag{2.2}$$

where $r_1(t)$ and $r_2(t)$ are the pre- and post-compression RF echo signals, respectively, $s(t)$ is the 1-D ultrasound scattering function, $p(t)$ denotes the point spread function (PSF) or ultrasound system response, a denotes the compression factor caused by mechanical deforming pressure to the medium, $v_1(t)$ and $v_2(t)$ are the uncorrelated random noise profiles and * sign is used to denote the convolution operation. It is to be noted that this model assumes no out of plane motion upon compression and, in

addition, the post-compression RF echo is assumed to be the scaled and shifted replica of the pre-compression RF echo in the absence of noise. According to [28], the strain s is related to the compression factor $1/a$ as $s = 1 - a$, where $a \leq 1$ and $s << 1$. Now the post-compression signal is stretched by a factor δ, i.e., $r_\delta(t) = r_2(\delta t)$. By neglecting the noise term (i.e., $v_\delta(t) = 0$), the normalized cross-correlation (NCC) peak $\zeta_\delta(\tau)$ (≤ 1) can be defined as [42], [61],

$$\zeta_\delta(\tau) = \frac{\int_{-\infty}^{\infty} r_1(t) r_\delta(t + \tau) dt}{\sqrt{\int_{-\infty}^{\infty} r_1^2(t) \int_{-\infty}^{\infty} r_\delta^2(t) dt}}. \tag{2.3}$$

Eqn. (2.3) becomes maximum for $\delta = a$ with the assumption of $p(\delta t) \cong p(t)$. Then the effective strain can be directly calculated from the stretching factor $s = 1 - \delta_o$ where,

$$\delta_o = arg \max_\delta \{\zeta_\delta(\tau)\}. \tag{2.4}$$

2.2.2 Adaptive Spectral Strain Estimation from Power Spectral Centroid Shift [54]

Assuming that $s(t)$ and $p(t)$ in Eqns. (2.1) and (2.2) can be described by their auto-correlation functions that may be modeled by modulated Gaussian functions as

$$s(t) = \frac{1}{\sqrt{2\pi} L_h} exp(-\frac{t^2}{2L_h^2}) sin(k_h t), \tag{2.5}$$

$$p(t) = \frac{1}{\sqrt{2\pi} L_e} exp(-\frac{t^2}{2L_e^2}) cos(k_e t), \tag{2.6}$$

Here L_h and L_e are the resolution lengths of the PSF and the scattering function, respectively. k_h is the central spatial frequency of the PSF and k_e is the central spatial frequency of the scattering function.

Now, the power spectra of the pre- and post-compression RF signals defined in Eqns. (2.1) and (2.2) (only considering the positive frequency) are given, respectively, by:

$$R_1(k) = \frac{1}{4} exp\left(-\frac{1}{4}[(k - k_h)^2 L_h^2 + (k - k_e)^2 L_e^2]\right) + N_1(k), \tag{2.7}$$

$$R_2(k) = \frac{1}{4a} exp\left(-\frac{1}{4}[(k - k_h)^2 L_h^2 + (k - k_e)^2 \frac{L_e^2}{a^2}]\right) + N_2(k). \tag{2.8}$$

From the one sided power spectra, f_{c1} and f_{c2}, the center frequency of pre- and post-compression signals, respectively can be calculated from the spectral peaks. Finally, the local strain is calculated as

$$f_{c1} - f_{c2} = \frac{c/2\pi}{ak_e - k_e} = (a-1)f_{c1},$$ (2.9)

or,

$$\frac{f_{c1} - f_{c2}}{f_{c1}} \cong s,$$ (2.10)

where c is the sound speed and s is the local strain.

2.2.3 Adaptive Spectral Strain Estimation from Power Spectral Cross-correlation [49]

The cross-correlation between the pre- and the post-compression power spectra defined in Eqns. (2.7) and (2.8) can be given by:

$$S(k_o) = \int_{-\infty}^{\infty} R_1(k+k_o)R_2(k)dk,$$ (2.11)

where k_o is the spectral shift between the pre- and post-compression power spectra. Finally, the local strain "s" is calculated from the following equation derived from the cross-correlation in Eqn. (2.19) as

$$k_o \approx -\frac{k_h}{2}s.$$ (2.12)

2.2.4 Hybrid Spectral Strain Estimation [62]

It is previously shown in Eqns. (2.5) and (2.6) that $s(t)$ and $p(t)$ can be described by their autocorrelation functions that may be modeled by modulated Gaussian functions as

$$s(t) = \frac{1}{\sqrt{2\pi}L_h}exp(-\frac{t^2}{2L_h^2})sin(k_h t),$$ (2.13)

$$p(t) = \frac{1}{\sqrt{2\pi}L_e}exp(-\frac{t^2}{2L_e^2})cos(k_e t),$$ (2.14)

13

where L_h and L_e are the resolution lengths of the PSF and the scattering function, respectively. k_h is the central spatial frequency of the PSF and k_e is the central spatial frequency of the scattering function. Now, the bandwidths corresponding to the pre- and post-compression power are given by [54]:

$$B_1 = \frac{c}{2\pi} \frac{2.35}{\sqrt{L_h^2 + L_e^2}}, \tag{2.15}$$

$$B_2 = \frac{c}{2\pi} \frac{2.35}{\sqrt{L_h^2 + \frac{L_e^2}{a^2}}}, \tag{2.16}$$

where c is the speed of sound in tissue. The bandwidth broadening β (for Gaussian spectra) is described as

$$\beta = \frac{B_1}{B_2} = \frac{\sqrt{L_h^2 + \frac{L_e^2}{a^2}}}{\sqrt{L_h^2 + L_e^2}}. \tag{2.17}$$

Eqn. (2.17) can be simplified as

$$\beta = \sqrt{\frac{1}{2}\left(1 + \frac{1}{a^2}\right)} = \sqrt{\frac{1}{2}(1 + (1 - s)^2)}. \tag{2.18}$$

Now, the strain estimation technique can be described with a two-stage process as

1. The first stage locally scales the post-compression power spectra by a factor estimated using Eqn. (2.18).

2. Using the knowledge from first stage in estimating the strain as

$$f_{c1} - f_{c2} = \frac{c/2\pi}{ak_e - k_e} = (a - 1)f_{c1}, \tag{2.19}$$

or,

$$\frac{f_{c1} - f_{c2}}{f_{c1}} \cong s, \tag{2.20}$$

where c is the sound speed and s is the local strain.

14

2.2.5 Adaptive Spectral Stretching-based Strain Estimation [50]

Pre- and post-compression echo spectra, respectively, are modeled as

$$R_1(f) = B(f)H(f), \tag{2.21}$$

$$R_2(f) = |a|B(af)H(f), \tag{2.22}$$

where, $B(f)$ is the Fourier Transform of 1-D scattering distribution of elastic target, $H(f)$ is the Fourier Transform of impulse response of the Ultrasound system, additive noise are ignored and the constant, $a = 1 - \epsilon$. Here, ϵ is the local strain.

After frequency scaling by a factor α_f, the post-compression signal spectrum becomes

$$R_3(f) = R_2(f/\alpha_f) = |a|B(af/\alpha_f)H(f/\alpha_f). \tag{2.23}$$

After stretching the post-compression spectrum by α_f, the cross-correlation between the pre- and post-compression spectra can be estimated as

$$\rho_{13}(k) = \frac{\sum_{m=1}^{N/2} P_1(m) \cdot P_3(m+k)}{\sqrt{\sum_{m=1}^{N/2} P_1(m) \cdot \sum_{m=1}^{N/2} P_3(m)}} \tag{2.24}$$

where N is the number of Fourier points. Eqn. (2.24) becomes maximum for $\alpha_f = a$ with the assumption of $H(f/\alpha_f) \cong H(f)$. Then the effective strain can be directly calculated from the stretching factor $s = 1 - \alpha_{fo}$ where,

$$\alpha_{fo} = arg \max_{\alpha_f} \{\rho_{13}(k)\}. \tag{2.25}$$

2.3 Gradient-based Strain Estimation Techniques

2.3.1 Combined Autocorrelation Method [63]

The RF signals before and after compression can be modeled as

$$i_1(t, x) = A(t, x)e^{j(\omega_0 t - \theta)}, \tag{2.26}$$

$$i_2(t, x) = A(t - \tau, x - u_x)e^{j[(\omega_0(t-\tau) - \theta)]}, \tag{2.27}$$

where $i_1(t, x)$ and $i_2(t, x)$ denote the complex RF signals measured before and after deformation, respectively, $A(t, x)$ denotes the envelope, ω_0 denotes the transducer's center angular frequency, τ denotes the time shift, and u_x denotes the lateral displacement.

The IQ signals $s_1(t, x)$ and $s_2(t, x)$ can be obtained after demodulating RF signals using quadrature detector. The complex cross-correlation function between $s_1(t, x)$ and $s_2(t + nT/2, x + mL)$ is defined as

$$R_{12}(t, x; n, m) = \int \int_D s_1(t + v, x + w) \times s_2(t + nT/2 + v, x + mL + w)^* dv dw, \quad (2.28)$$

where $(n = -N_{min}, \wedge, -1, 0, 1, \wedge, N_{max})$ and $(n = -M_{min}, \wedge, -1, 0, 1, \wedge, M_{max})$, T denotes the period of the ultrasonic signal, L denotes the interval of scan lines, and D is the correlation window size.

Substituting $s_1(t, x)$ and $s_2(t, x)$ into Eqns. (2.26) and (2.27), and then from Eqn. (2.28), $R_{12}(t, x; n, m)$ can be found as

$$R_{12}(t, x; n, m) = R_A(t, x; \tau - nT/2, u_x - mL)e^{j\omega_0(\tau - nT/2)}, \quad (2.29)$$

where $R_A(t, x; \tau, u_x)$ is the autocorrelation function of the envelope.

Here, the first step is coarse estimation that searches maximum envelope correlation. The second step is a fine estimation by using the unwrapped phase $\phi(t, x; k, l)$ of R_{12} which is obtained from the first step. The time shift τ, the axial displacement u_y and the lateral displacement u_x at a measurement point (t, x) are then given, respectively, by

$$\tau = -\frac{\phi(t, x; k, l)}{\omega_0} + \frac{kT}{2} \quad (2.30)$$

$$u_y = \frac{c\tau}{2} \quad (2.31)$$

$$u_x = lL R_A \quad (2.32)$$

where, c is the ultrasound velocity in the tissue.

2.3.2   1-D Displacement Estimation Using Dynamic Programming [39]

In this method, 1-D tissue deformation is estimated by dynamic programming (DP) approach. Considering two echo signals and corresponding to two scan-lines acquired

before and after compression, each signal sampled at $i = 1, 2, \cdots m$. The difference between the two signals Δ can be quantified using the SAD as

$$\Delta(i, d) = |g(i) - g'(i + d)| \tag{2.33}$$

where $d_{min} \leq d \leq d_{max}$ is the displacement at the sample i, and d_{min} and d_{max} denote the allowed displacements. To reduce the effect of gain on Δ, both pre- and post-compression ultrasound images are divided by the maximum value of one of the images.

The smoothness of the displacements is S:

$$S(d_i, d_{i-1}) = (d_i - d_{i-1})^k \tag{2.34}$$

where d_i is the displacement at the sample i and d_{i-1} is the displacement at the sample $i - 1$ of the $g(i)$. The cost function C at a point i and associated displacement d_i is defined as a recursive function

$$C(i, d_i) = min_{d_{i-1}}\{C(i - 1, d_{i-1}) + \omega S(d_i, d_{i-1})\} + \Delta(i, d_i) \tag{2.35}$$

where ω is a regularization weight which governs smoothness. The values of the function are stored in a $(d_{max} - d_{min} + 1) \times m$ matrix.

Generally, the optimum value of d_{i-1} should be sought in the entire $[d_{min}, d_{max}]$ range. However, since the strain value is low in elastography, it is expected and desired that at each sample of RF data, the change between the displacement of a sample and its previous sample is not more than 1. Therefore, the search range of optimum value for d_{i-1} is limited to the three values of d_{i-1}, d_i and d_{i+1}, which results in a significant gain in speed. This limit on the search range does not affect the results even in a high strain of 10%. The value of d_{i-1} that minimizes the cost is also "memorized" in a function M for later use

$$M(i, d_i) = \arg\min_{d_{i-1}}\{C(i - 1, d_{i-1}) + \omega S(d_i, d_{i-1})\} \tag{2.36}$$

The cost function C is calculated for $i = 1 \cdots m$. The minimum cost at $i = m$ gives the displacement of this point, which is traced back to $i = 1$ using the M function to

calculate all the displacements (D)

$$D(i) = \arg \min_{d_i}\{C(i, d_i)\}, \quad i = m \tag{2.37}$$

$$D(i) = M(i + 1, D(i + 1)), \quad i = 1 \cdots m - 1 \tag{2.38}$$

2.3.3   2-D Displacement Estimation Using Dynamic Programming [39]

A 2-D smoothness regularization that considers the displacements between adjacent scan-lines is more natural. The DP algorithm of 1-D strain estimation is modified here to allow for 2-D displacement estimation and 2-D smoothness regularization. Assuming that ultrasound images consist of scan-lines, the distance between the pre and post-compression signals is

$$\Delta(i, j, d_a, d_l) = |g_j(i) - g'_{j+di}(i + d_a)| \tag{2.39}$$

where $d_{a,min} \leq d_a \leq d_{a,max}$ and $d_{l,min} \leq d_l \leq d_{l,max}$ are the axial and lateral displacements, respectively, and $j = 1 \cdots n$ refers to jth scan-line and $i = 1 \cdots m$

$$S(d_{a_i}, d_{l_i}, d_{a_{i-1}}, d_{l_{i-1}}) = (d_{a_i} - d_{a_{i-1}})^2 + (d_{l_i} - d_{l_{i-1}})^2 \tag{2.40}$$

is the smoothness regularization with subscripts a and l referring to axial and lateral. The cost function at the ith sample of the ith scan-line is:

$$C_j(d_a, d_l, i) = \arg \min_{d_a, d_l}\left\{\frac{C_j(\delta_a, \delta_l, i - 1) + C_{j-1}(\delta_a, \delta_l, i)}{2} + \omega S(d_a, d_l, \delta_a, \delta_l)\right\} + \Delta(d_a, d_l, i) \tag{2.41}$$

For memorization, δ_a and δ_l values that minimize the cost function are stored for all d_a, d_l and i values. The specific form of the cost function allows the calculation of the displacement of each scan-line using the cost values of the previous scan-line. The cost function of the jth line, $C_j(d_a, d_l, i)$, is calculated and is minimized, resulting in its displacement map.

18

2.4   Conclusion

Tissue elasticity has always been an important concept in the fields of medicine and biology. Quasi-static ultrasound elastography is a modern idea that digitally measure the tissue elasticity for patient diagnosis. It requires surprisingly complex techniques to properly visualize the stiffness variation inside a tissue system. Some of these techniques have been briefly outlined in this chapter. Although, the elastography is sufficiently mature to allow successful commercialization, a number of issues remain unanswered and require further study in future. However, it is evident that many assumptions are required in the estimation of an elastogram, particularly in the mechanics of the tissue deformation. On going research has already paved some ways to relax some of these assumptions in successful elasticity imaging.

Chapter 3

Average Strain Estimation Using Weighted Nearest Neighbor Cross-Correlation Peaks

3.1 Introduction

In quasi-static elasticity imaging, different algorithms are developed to calculate strain that can be broadly categorized into 1) gradient-based strain estimation [1], [41], [44]–[47], and 2) direct strain estimation [36], [48]–[50]. The gradient-based strain estimation relies on calculating displacement from the cross-correlation between pre- and post-compression RF windowed echo segments. High frequency noise is generally amplified by the gradient operation [47], [49]. Therefore, before gradient operation, a smoothing technique based on least-squares-based linear regression [52] or least-squared-error-based smoothing-spline [47] can be applied on displacement matrix. Median filtering is also effective before gradient operation to remove the shot noise and some false peak noise. For smoothing the strain image, some recent literature [39]–[41], [53] proposes to consider the previous window estimates in computing the present displacement value to maintain continuity of strain. But these smoothing algorithms are not intelligent enough to detect and preserve the lesion edge. In direct strain estimation, the strain

is directly calculated from a pair of pre- and post-compression RF-echo segments in 1) time domain [36] or 2) in frequency domain [49], [50]. It is considered that the post-compression echo is a compressed and delayed version of its counterpart pre-compression echo [36]. This signal model inspires the idea of stretching the post-compression echo or shifting the pre-compression signal spectrum before the cross-correlation calculation. These techniques can generate strain image with higher SNR than the gradient-based techniques, but the elastogram produced by the direct strain estimation techniques has no strain continuity guarantee among neighboring pixels of a particular area of the strain image.

In this chapter, we propose two novel techniques for strain estimation; 1) the direct average strain estimation (DASE) and 2) the gradient-based average strain estimation (GBASE). In both techniques, regularization of strain continuity is ensured without using any prior estimates of the displacement or strain; both make use of a cost function to apply exponential weights to normalized cross-correlation peaks in the lateral (for GBASE) or in both the lateral and the axial (for DASE) directions. Due to the similarity of the physical properties of the neighboring tissue elements, it is assumed that the strain at a particular point has similarity with its neighbor in both the axial and the lateral directions while displacement at a particular point is almost coherent with its neighbor in the lateral direction. The average displacement or strain value is calculated from the corresponding cost function defined for each of the pixels. The exponential weight attached with the cost function ensures less distortion at the lesion boundary. The performance of this algorithm is evaluated using a FEM phantom, experimental phantom as well as *in vivo* data and compared to other recently reported gradient-based and direct strain estimation algorithms.

3.2 The Signal Model

Symbols and acronyms used in this thesis are presented in Table 3.1.

The simplified 1-D model of the backscattered ultrasound RF signals before and after

Table 3.1: Symbols and acronyms.

Symbols	Definitions
L_v	Inter-window shift between two consecutive radio-frequency echo segments
L_i	Length of radio-frequency echo segments
L_w	Width of 2-D windowed radio-frequency echo segment
N_c	Number of scan lines in a single ultrasound image
s_{avg}	Applied strain
ν	Poisson's ratio
$\{L_a, L_l\}$	Nearest neighbor factors in the axial and lateral directions, respectively
$\{\chi_a, \chi_l\}$	Weighting factors of the exponential weight function in the axial and lateral directions, respectively
AM	Analytic minimization
AS	Adaptive-stretching strain estimator
NCC	Normalized cross-correlation
CNRe	Elastographic contrast-to-noise ratio
DASE	Direct average strain estimation
FEM	Finite element modeling
GBASE	Gradient-based average strain estimation
MSE	Mean square error
SSIM	Structural similarity
MSSIM	Mean structural similarity
NN	Nearest neighbor
PSF	Point spread function
PSNR	Peak signal-to-noise ratio
RF	Radio-frequency
NSAD	Normalized sum of absolute differences
SNR	Signal-to-noise ratio
SNRe	Elastographic signal-to-noise ratio
NSSD	Normalized sum of squared differences
TGC	Time-gain-compensation

compression are given by [36]:

$$r_1(t) = s_1(t) + v_1(t) = s(t) * p(t) + v_1(t) \tag{3.1}$$

$$r_2(t) = s_2(t) + v_2(t) = s\left(\frac{t}{a} - t_0\right) * p(t) + v_2(t) \tag{3.2}$$

where, $r_1(t)$ and $r_2(t)$ are the pre- and post-compression RF echo signals, respectively, $s(t)$ is the 1-D ultrasound scattering function, $p(t)$ denotes the point spread function (PSF) or ultrasound system response, a denotes the compression factor caused by mechanical deforming pressure to the medium, $v_1(t)$ and $v_2(t)$ are the uncorrelated random noise profiles and * sign is used to denote the convolution operation. It is to be noted that this model assumes no out of plane motion upon compression and, in addition, the post-compression RF echo is assumed to be the scaled and shifted replica of the pre-compression RF echo in the absence of noise. According to [28], the strain s is related to the compression factor $1/a$ as $s = 1 - a$, where $a \leq 1$ and $s << 1$. Now the post-compression signal is stretched by a factor δ, i.e., $r_\delta(t) = r_2(\delta t)$. By neglecting the noise term (i.e., $v_\delta(t) = 0$), the normalized cross-correlation (NCC) peak $\zeta_\delta(\tau)$ (≤ 1) can be defined as [42], [61],

$$\zeta_\delta(\tau) = \frac{\int_{-\infty}^{\infty} r_1(t) r_\delta(t + \tau) dt}{\sqrt{\int_{-\infty}^{\infty} r_1^2(t) \int_{-\infty}^{\infty} r_\delta^2(t) dt}} \tag{3.3}$$

Equation (3.3) becomes maximum for $\delta = a$ with the assumption of $p(\delta t) \cong p(t)$. Then the effective strain can be directly calculated from the stretching factor $s = 1 - \delta_o$ where,

$$\delta_o = arg \max_\delta \{\zeta_\delta(\tau)\}. \tag{3.4}$$

3.3   Average Strain Estimation Using the Weighted Nearest Neighbor Method

To reduce the signal de-correlation that results from non-axial motion and introduce a built-in smoothing feature, we propose the direct average strain estimation (DASE) using the weighted nearest neighbor method. Due to the similarity of the physical

properties of the tissue with its surrounding, calculated strain from a pair of windowed RF segments for a particular tissue point is assumed to be close to the strains in the neighboring tissues. This assumption is valid unless there is a sharp change in the tissue stiffness. To make the algorithm intelligent enough to cope with the situation, our proposed method incorporates an exponentially decaying weight that allows the tracking of a sharp change in the strain on the lesion boundary (to be discussed in the next section).

3.3.1   1-Dimensional Direct Average Strain Estimation

Let $F_1(i,j)$ and $F_2(i,j)$ denote the pre- and post-compression ultrasound RF frames, respectively. Here, i denotes the axial depth index and j denotes the scan line or RF A-line indices (Fig. 3.1). To calculate the effective strain at a point (i_s, j_s) of the strain image, a corresponding pair of 1-D windowed RF segments $r_1^{(i_s,j_s)}$ and $r_2^{(i_s,j_s)}$ are selected from the pre- and post-compression ultrasound image frames as:

$$r_1^{(i_s,j_s)}(i) = F_1((i_s - 1)L_v + i, j), \tag{3.5}$$
$$\text{for } 1 \leq i \leq L_i \text{ and } j = j_s$$

$$r_2^{(i_s,j_s)}(i) = F_2(round((i_s - 1)(1 - s_{avg})L_v) + i, j), \tag{3.6}$$
$$\text{for } 1 \leq i \leq L_i \text{ and } j = j_s + (j_s - \frac{N_c}{2})s_{avg}\nu$$

where ν is the Poisson's ratio, s_{avg} is the approximate applied strain, N_c is the number of scan lines in a single ultrasound image, L_v is the distance between samples of the two windowed RF echo segments in the axial direction and L_i is the length of the 1-D RF window. Note that s_{avg} is not the actual strain but an effective strain that is being estimated as it is not always possible to know the exact stress being applied to the material. Therefore, the estimated strain value is the relative strain value of tissue components. The value of j in $r_2^{(i_s,j_s)}$ may deviate from j_s due to the expected lateral shift (Fig. 3.2). It is observed from Fig. 3.2 that if the column index j_s has a value
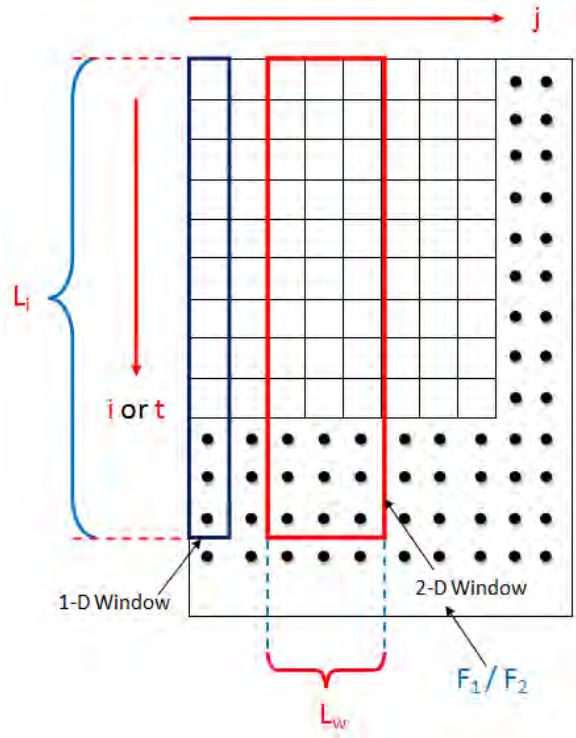
Figure 3.1: 1-D and 2-D window selection from RF echo frame for 1-D DASE and 2-D DASE, respectively. Here, L_i is the axial length of the RF window (for both, the 1-D DASE and 2-D DASE methods) and L_w is the number of A-lines in 2-D RF window (for the 2-D DASE method).

(say, j_{s1}) in the pre-compression RF echo segment, then the post-compression RF echo segment will have a different column index. However, we can assume $j_s \approx j$ for low applied strain. Therefore, in selecting the post-compression signal window from the RF frame, Poisson's ratio is used to reduce the lateral shift effect in axial strain calculation while considering no lateral motion at the transducer face and at the supporting base with closely satisfied non-slip boundary condition. For well-behaved axial stress, lateral motion is zero around the center of the application area and increases with increasing distance (Fig. 3.2).

After stretching the post-compression echo window $r_2^{(i_s,j_s)}$ by a factor δ (≤ 1), i.e., $r_\delta^{(i_s,j_s)}(i) = r_2^{(i_s,j_s)}(\delta i)$, the NCC coefficient $\zeta_\delta^{1D}(k)$ between $r_1^{(i_s,j_s)}$ and $r_\delta^{(i_s,j_s)}$ is
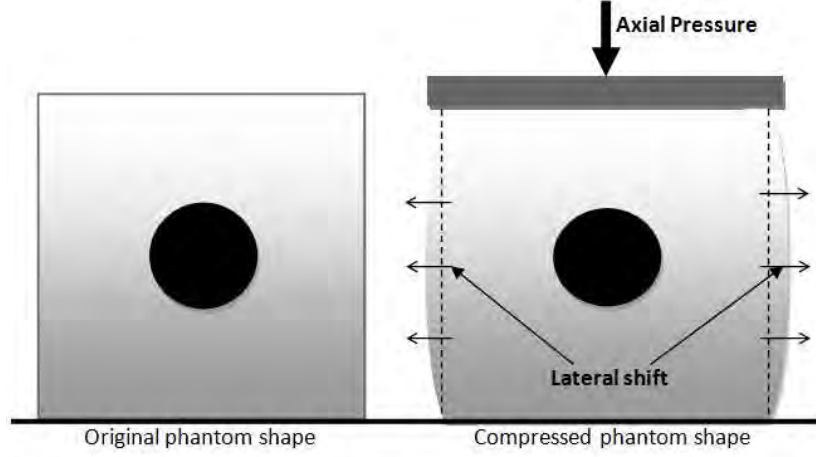
Figure 3.2: Representation of lateral shift due to axial applied pressure in non-slip boundary condition. This lateral shift can be incorporated by using expected lateral shift from the Poisson's ratio in selecting signal window.

calculated as [61],

$$\zeta_{\delta,1D}^{(i_s,j_s)}(k) = \frac{\sum_{i=1}^{L_i} r_1^{(i_s,j_s)}(i) \cdot r_\delta^{(i_s,j_s)}(i+k)}{\sqrt{\sum_{i=1}^{L_i} \{r_1^{(i_s,j_s)}(i)\}^2 \sum_{i=1}^{L_i} \{r_\delta^{(i_s,j_s)}(i)\}^2}}. \tag{3.7}$$

The peaks of $\zeta_{\delta,1D}^{(i_s,j_s)}(k)$ can be calculated by using any sub-pixel interpolation algorithm (e.g., cosine interpolation, parabolic interpolation) for different values of δ. However, in this work we have used parabolic interpolation. Therefore,

$$k_p = \arg\max_k \{\zeta_{\delta,1D}^{(i_s,j_s)}(k)\} \tag{3.8}$$

$$M_\delta^{1D}(i_s, j_s) = \zeta_{\delta,1D}^{(i_s,j_s)}(k_p) \tag{3.9}$$

Here, M_δ^{1D} is a 2-D matrix consisting of the cross-correlation peaks. A weighting function $w^{(i_s,j_s)}(i_1, j_1)$ is defined so that the RF windowed segments of increasing distance are properly weighted to be less "emphasized" (Fig. 3.3). As the stiffness of a tissue element is more similar to the nearer neighboring elements than the distant ones, an exponential weight function is introduced that ensures relatively larger weights to the nearest cross-correlation peaks that decays rapidly with distance:

$$w^{(i_s,j_s)}(i_0, j_0) = e^{-|\chi_a(i_0-i_s)|-|\chi_l(j_0-j_s)|} \tag{3.10}$$
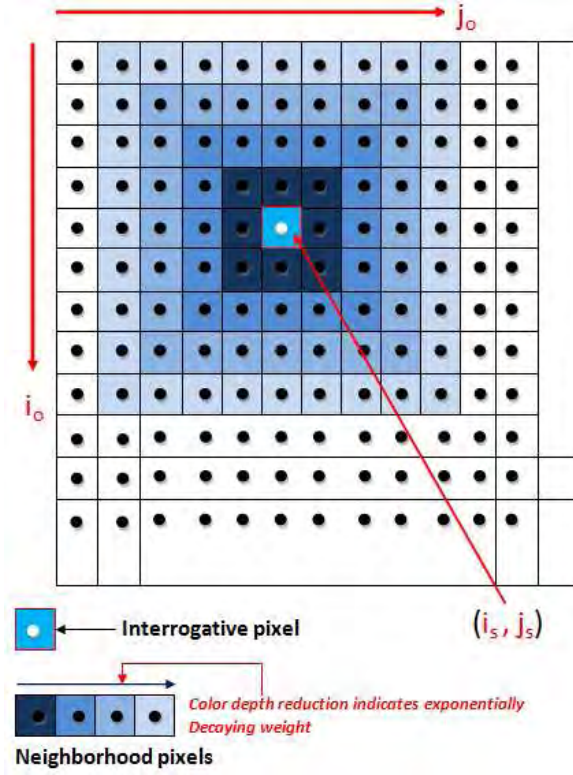
Figure 3.3: Illustration of the neighboring window's contribution in the estimation of effective strain for a particular point (i_s,j_s) in the correlation peak map for a particular strain s. Note that some neighboring (here four) pixel values weighted exponentially are also used to estimate the effective strain at (i_s,j_s) point.

where χ_a and χ_l are the weighting factors in the axial and lateral directions, respectively, and, $i_s - L_a \leq i_0 \leq i_s + L_a$ and $j_s - L_l \leq j_0 \leq j_s + L_l$. It is clear from eqn. (5.9) that $w^{(i_s,j_s)}(i_0, j_0)$ has a maximum value of unity at $(i_0, j_0) = (i_s, j_s)$. To estimate the *average* strain, a cost function is defined from M_δ^{1D} (eqn. (5.7)) and weight function $w^{(i_s,j_s)}(i_0, j_0)$ as

$$J_\delta^{(i_s,j_s)} = \sum_{i_1=i_s-L_a}^{i_s+L_a} \sum_{j_1=j_s-L_l}^{j_s+L_l} w^{(i_s,j_s)}(i_1, j_1)\, M_\delta^{1D}(i_1, j_1) \tag{3.11}$$

where L_a and L_l are the nearest neighbor (NN) factors in the axial and lateral directions, respectively. Unless otherwise specified, we use $L_a = 3$, $L_l = 3$ in this study. Increase in the value of L_a and L_l causes more smoothing of the strain image. $J_\delta^{(i_s,j_s)}$

is calculated for different values of $\delta(\delta_{min} \leq \delta \leq \delta_{max})$. Generally, δ_{max} is set to 1 (zero strain) and δ_{min} is set to a lower value than $(1 - s_{avg})$. The desired value of δ is calculated for which $J_\delta^{(i_s,j_s)}$ is maximum as

$$\delta_o^{(i_s,j_s)} = \arg\max_\delta\{J_\delta^{(i_s,j_s)}\}. \qquad (3.12)$$

And, finally, the effective strain at (i_s, j_s) is estimated as

$$S_o(i_s, j_s) = 1 - \delta_o^{(i_s,j_s)}. \qquad (3.13)$$

It is important that $\delta = \delta_o^{(i_s,j_s)}$ is indirectly partially dependent on the range of values of $M_\delta^{1D}(g_s, h_s)$ $(i_s - L_a \leq g_s \leq i_s + L_a; j_s - L_l \leq h_s \leq j_s + L_l)$ via the cost function. It is a clear contrast to the instantaneous cost function-based approaches in adaptive spectral stretching or adaptive stretching-based strain estimation. Therefore, the neighboring cross-correlation peaks governed by the weight function have a significant impact in the calculation of $S_o(i_s, j_s)$ and estimated strain is expected to be much more well behaved.

Two significant advantages of the DASE compared to the conventional adaptive stretching based strain estimation [36] can be summarized as:

1. Reducing the lateral shift due to axial stress (using ν in eqn. (5.4)) before the selection of pre- and post-compression RF segments; and

2. Estimating the average strain directly by taking the nearest neighbors into account.

Note that we also discuss a 2-D direct average strain estimation method in the next subsection. But the word "DASE" will, by default, indicate the 1-D direct average strain estimation, unless otherwise specified.

3.3.2 2-D Direct Average Strain Estimation

In this method, we chose 2-D pre- and post-compression windows of three consecutive scan-lines according to eqns. (5.3) and (5.4) with $\nu = 0$ (i.e., no incorporation of the

Poisson's ratio). After stretching the post-compression windowed signal in the axial direction, the NCC coefficient $\zeta_{\delta,2D}^{(i_s,j_s)}(k,p)$ is calculated as [61]

$$\zeta_{\delta,2D}^{(i_s,j_s)}(k,p) = \frac{A}{B} \tag{3.14}$$

where

$$A = \sum_{i=1}^{L_i} \sum_{n=1}^{L_w} r_1^{(i_s,j_s)}(i,n).r_\delta^{(i_s,j_s)}(i+k,n+p),$$

$$B = \sqrt{\sum_{i=1}^{L_i} \sum_{n=1}^{L_w} \{r_1^{(i_s,j_s)}(i,n)\}^2 \{r_\delta^{(i_s,j_s)}(i,n)\}^2}$$

n denotes the scan-line index and L_w denotes the width of the 2-D windowed echo segment. The peaks of $\zeta_{\delta,2D}^{(i_s,j_s)}(k,p)$ are calculated by using the parabolic sub-pixel interpolation algorithm for different values of δ and M_δ^{2D} is computed in a similar fashion like M_δ^{1D} (eqn. (5.7)). Similarly, the cost function for the 2-D case is defined as in eqn. (5.8) for the 1-D case by using the same weight function defined in eqn. (5.9). Finally, by finding the corresponding δ for the maximum cost, the average strain S_o at (i_s,j_s) is estimated for the 2-D case.

3.4 Elasticity Estimation From Average Displacement

The proposed DASE technique can generate very high quality strain images as demonstrated in the results section, but at the cost of very high computational time like other published direct strain estimation techniques. Therefore, in spite of noise susceptibility, gradient-based strain estimation is more popular, especially for real-time and near-real-time implementations. In this technique, effective strain is calculated as the spatial derivative of the axial displacement. Various techniques are available in the literature to denoise the displacement field like the smoothing spline method [47], least-squares approach [52], regularization based approach [53], etc. As noise is unavoidable in free-hand elastography, we develop here a robust algorithm for estimation

of the average displacement. We assume that the displacement of the neighboring tissue elements along each of the A-lines at the same distance from the ultrasound probe would be the same in response to the equally applied external pressure.

In many gradient-based strain estimation techniques, post-compression echo is temporally stretched to reduce de-correlation. But this approach leads to increased noise in stiffer lesion areas where the post-compression signal undergoes less compression. In our proposed GBASE method, we use two different values of δ (i.e., $\delta_{max} = 1$ and $\delta_{avg} = 1 - s_{avg}$) for stretching the post-compression signal to compute the cross-correlation $\zeta_\delta^{(i_s,j_s)}(k)$ (eqn. (5.6)). We have used $\delta_{max}=1$ for the purpose of detecting hard objects (e.g., lesions) in the material being scanned. If a hard inclusion is present, then the post-compression RF echo signal will not be a compressed replica of the pre-compression one as assumed in the signal model. Therefore, to detect the hard inclusions we do not stretch the post-compression RF echo signal and setting δ_{max} equal to 1 serves the purpose. Then, two cost functions are calculated as

$$\tilde{J}_\delta^{(i_s,j_s)}(k) = \sum_{j_1=j_s-L_l}^{j_s+L_l} w^{(i_s,j_s)}(i_s,j_1)\, \zeta_\delta^{(i_s,j_s)}(k) \tag{3.15}$$

where $\delta = \delta_{max}$ & δ_{avg}. We calculate the stretching factor δ via the strain s as $\delta = 1 - s$ and, therefore, the δ_{max} corresponds to the no compression (strain) case and the δ_{avg} corresponds to the approximate applied strain case. From the maximum of the cost functions, the displacement is calculated as

$$k_\delta^{(i_s,j_s)} = \arg\max_k\{\tilde{J}_\delta^{(i_s,j_s)}(k)\}, \text{for } \delta = \delta_{max} \ \& \ \delta_{avg}. \tag{3.16}$$

Finally, the displacement matrix is calculated as

$$D(i_s,j_s) = \begin{cases} k_{\delta_{avg}}^{(i_s,j_s)} + k_{comp} + \frac{L_i}{2}s_{avg} \ ; & \beta \geq \gamma \\ k_{\delta_{max}}^{(i_s,j_s)} + k_{comp} \ ; & \text{otherwise} \end{cases} \tag{3.17}$$

where $\beta = \tilde{J}_{\delta_{avg}}^{(i_s,j_s)}(k_{\delta_{avg}}^{(i_s,j_s)})$, $\gamma = \tilde{J}_{\delta_{max}}^{(i_s,j_s)}(k_{\delta_{max}}^{(i_s,j_s)})$ and $k_{comp} = round((i_s-1)\delta_{avg}L_v) - (i_s-1)L_v$. Here, k_{comp} is inserted to compensate the effect of using the shifting factor $(1 - s_{avg})$ for the window selection in eqn. (5.4). As we stretch the post-compression signal before cross-correlation operation, we used the third part $(\frac{L_i}{2}s_{avg})$ in eqn. (4.12)

to incorporate the effect of signal stretching on echo displacement. Finally, the effective strain $S_g(i_s, j_s)$ is calculated from $D(i_s, j_s)$ using the least-square-error-based strain estimation method [52] with 4-points per strain estimate.

In the cost functions (eqn. (3.15)) above, we can use an error function that defines the conservation of echo amplitude to avoid relatively computationally expensive NCC-based shift measurements (eqn. (5.6)). A simple sum of absolute differences (NSAD) or the sum of squared differences (NSSD) [61] between the pre- and stretched post-compression RF segments can be also used to calculate the error function as in the following:

$$\zeta_\delta^{(i_s,j_s)}(k) = \sum_{i=1}^{L_i} \left[\frac{r_1^{(i_s,j_s)}(i)}{\sqrt{\sum_{i=1}^{L_i} r_1^{(i_s,j_s)}(i)^2}} - \frac{r_\delta^{(i_s,j_s)}(i+k)}{\sqrt{\sum_{i=1}^{L_i} r_\delta^{(i_s,j_s)}(i)^2}} \right]^\gamma$$

(3.18)

where γ (=1 for NSAD and =2 for NSSD) is a constant. However, it is well established that NSSD performs better than NSAD. The cost function in eqn. (3.15) shall be minimized in this case.

3.5   Simulation and Experimental Results

We first present the efficacy of different salient features of the proposed methods. Then, we provide comparative results of our proposed methods with the adaptive strain estimator (AS) for elastography [36] and analytic minimization (AM) [53] method using the FEM phantom, CIRS experimental phantom and the *in vivo* patient data. In addition to subjective evaluation by visual inspection, we compare the performances of different methods in terms of several numerical metrics: elastographic signal-to-noise ratio (SNRe) [64], elastographic contrast-to-noise ratio (CNRe) [65], peak signal-to-noise ratio (PSNR) and mean structural similarity (MSSIM) [66].

3.5.1 Effectiveness of the Salient Features of the Proposed Methods

We use the FEM simulation phantom for checking the performance of different salient features of the proposed methods. A rectangular 40mm × 40mm FEM phantom was simulated using the analysis software Algor (Algor Inc., Pittsburgh, PA). In this simulation, the total number of nodes was 30372. A 2D FEM model was used and, therefore, it did not model out-of-plane motion. Total number of scatterers used in the simulation was 30372. This phantom had a homogeneous background with stiffness of 60kPa with four circular inclusions of 7.5mm diameter each (Fig. 5.3(a)). The stiffness of the four inclusions were as follows: (a) the bottom left one was 10dB stiffer, (b) the top one was 20dB stiffer, (c) the bottom right one was 30dB stiffer, and (d) the middle one was 40dB stiffer than the background. The phantom was compressed from the top using a larger-width planar compressor. The phantom was placed on a planar surface and allowed to freely expand (free-slip condition at top and bottom surfaces). An ultrasonic transducer of *center frequency,* $f_0 = 5$MHz and *band-width* $= 60\%$ was used to scan the phantom from the top by a non-diffracting beam of *width* $= 1.5$mm. The total number of scan lines was 128. Sonographic SNR of 40dB [47] was simulated with the addition of zero-mean white noise. Fig. 5.3(b) shows the ideal elastogram for 2% applied strain. The ideal strain profile of the marked line in Fig. 5.3(b) is plotted in Fig. 5.3(c) and we observe that there are two well defined "strain wells" due to 10dB and 30dB lesions indicating very small strain values in lesion regions. This strain profile also indicates that there are strain variations in the background region due to interaction between lesions, although the phantom has a uniform stiffness background.

To show the efficacy of Poisson's ratio, first we generate the baseline strain image (Fig. 3.5(a)) using the conventional adaptive stretching-based concept [36] by setting $\nu = 0$ (i.e., not using the Poisson's ratio to reduce the lateral shift effect) to select the RF window segment in eqn. (5.4) and $L_a = L_l = 0$ (i.e., not taking advantage of using the physical proximity of neighborhood) in computing the cost function in eqn. (5.8). The image in Fig. 3.5(a) is severely distorted. Now, setting $\nu = 0.25$

32
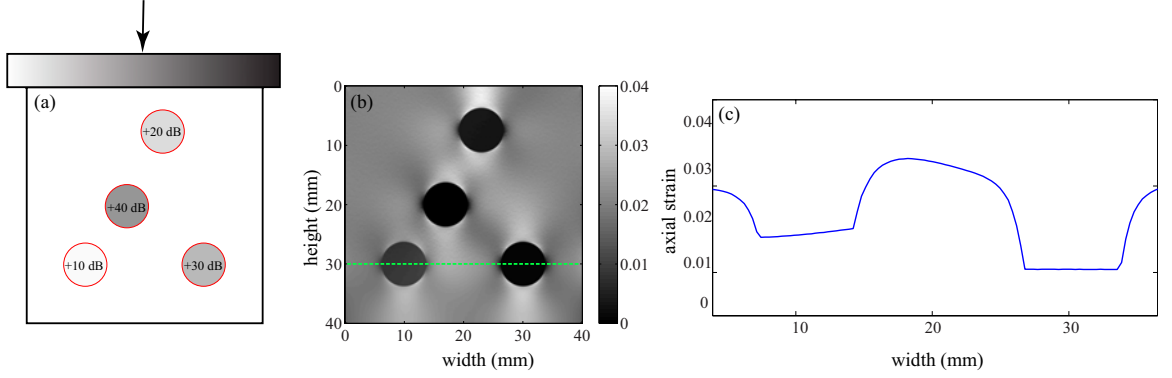
Figure 3.4: FEM simulation phantom. (a) Stiff inclusions in a homogeneous background of 60kPa, (b) corresponding ideal elastogram, (c) strain profile of the marked line in (b).

arbitrarily and $L_a = L_l = 0$, we generate Fig. 3.5(b) to demonstrate the reduction of noise that can be achieved in the left and right boundaries. The Poisson's ratio used in the simulation of the FEM phantom is 0.495 and, therefore, the selection of $\nu = 0.25$ does not generate noise-free strain image though the noise is reduced significantly. The impact of using the NN factor is observed in Fig. 3.5(c). In Fig. 3.5(c), we get an almost noise-free image for using the NN factor by setting $L_a = L_l = 3$. Note that the built-in smoothing by using the NN factor gives much better results than that of the median smoothing result in Fig. 3.5(d). Also note that the performance of the proposed method is sensitive to the setting of the Poisson's ratio for a large applied strain. Moreover, if the assumed Poisson's ratio is of the order of the true value, e.g., $0.5\nu_{vt} \leq \nu \leq 1.5\nu_{vt}$ (where ν_{vt} is true Poisson's ratio) at high strain, then NN factor would not affect the perceptual quality of the strain image noticeably.

To demonstrate the efficacy of the proposed cost function, we plot the mean of the NCC peaks $M_\delta^{1D}(g_s, h_s)$ ($i_s - 1 \leq g_s \leq i_s + 1$ and $j_s - 1 \leq h_s \leq j_s + 1$) and the proposed cost function ($J_\delta^{(i_s,j_s)}$) for strain map at (i_s, j_s) against the applied axial strain in Fig. 3.6. 25 realizations of the FEM simulation phantom described in Fig. 5.3(a) under 8% applied strain are used to generate Fig. 3.6. We can see from Fig. 3.6 that the abscissa of the mean NCC peak conventionally used for the instantaneous strain estimation at (i_s, j_s) is much deviated from the expected strain value (i.e., 0.08). But
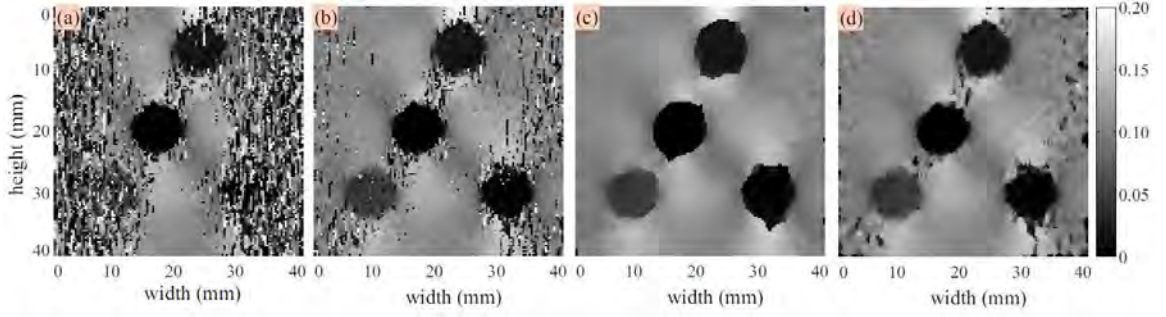
Figure 3.5: Effect of Poisson's ratio (ν) and lateral and axial NN factors in the strain estimation. Strain images generated by the (a) conventional direct strain estimator [36] for 10% applied strain, (b) proposed DASE method (using $\nu = 0.25$ and $L_a = L_l = 0$) for 10% applied strain, (c) proposed DASE method (using $\nu = 0.25$ and $L_a = L_l = 3$) for 10% applied strain, (d) median filtered strain image of (b).

the strain value at the maximum of the mean cost function ($J_\delta^{(i_s, j_s)}$), defined from the NCC peaks of the interrogative window and its neighborhood, is exactly equal to the approximate applied strain 0.08. In addition, the standard deviation of the cost peak is much lower than that of the instantaneous NCC peak. This shows a clear advantage of using the proposed cost function rather than using the instantaneous NCC peaks to calculate the strain.

Like the proposed DASE technique, the proposed GBASE method has the built-in smoothing feature in the displacement domain. If no lateral windows are considered in displacement estimation (i.e., $L_l = 0$ in eqn. (3.15)), then the instantaneous estimate of the displacement is obtained and is shown in Fig. 3.7(a). The displacement field is not smooth as evident from the zoomed view in Fig. 3.7(a). On the contrary, as shown in Fig. 3.7(b), it is smooth and continuous when the lateral windows ($L_l = 5$) are also considered in the displacement estimation of the interrogative window.

Along with the smoothing approach, the proposed GBASE method has another notable difference with the conventional gradient based strain estimators, it uses two different temporal stretching in the estimation of the displacement matrix. Figs. 3.8(a-b) now demonstrate the effect of two types of temporal stretching on the estimated strain images. Fig. 3.8(a) shows a strain image generated by the proposed GBASE
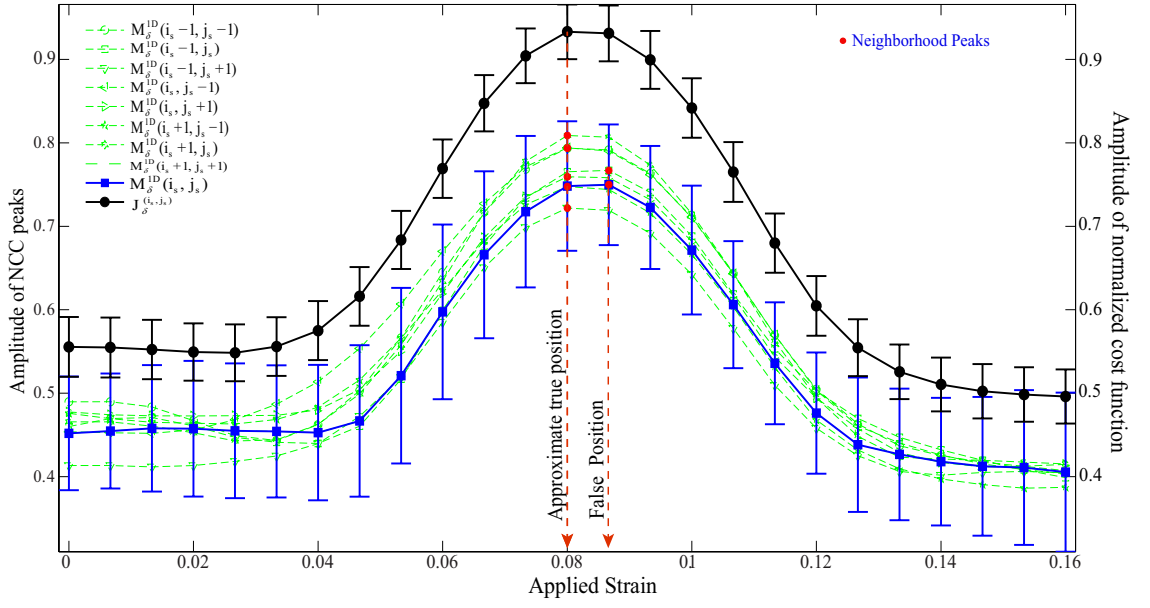
Figure 3.6: Representation of instantaneous mean NCC peaks $M_\delta^{1D}(g_s, h_s)$ $(i_s - 1 \leq g_s \leq i_s + 1$ and $j_s - 1 \leq h_s \leq j_s + 1)$ and the proposed mean cost function $(J_\delta^{(i_s, j_s)})$ for strain map at (i_s, j_s) using FEM phantom (under 8% applied strain) against the applied strain. We use 25 different speckle/noise realizations to generate error bar plots.

method using only one stretching factor (δ_{avg}). In this generated strain image, the hard inclusions are not appearing clearly. But if we use two stretching factors, then the hard inclusions are visualized clearly as evident from Fig. 3.8(b).

3.5.2 Comparison Using FEM Simulation

Before presenting the comparative results, we provide the definitions of four numerical performance metrics, e.g., SNRe, CNRe, PSNR and MSSIM. The quality metrics are defined as
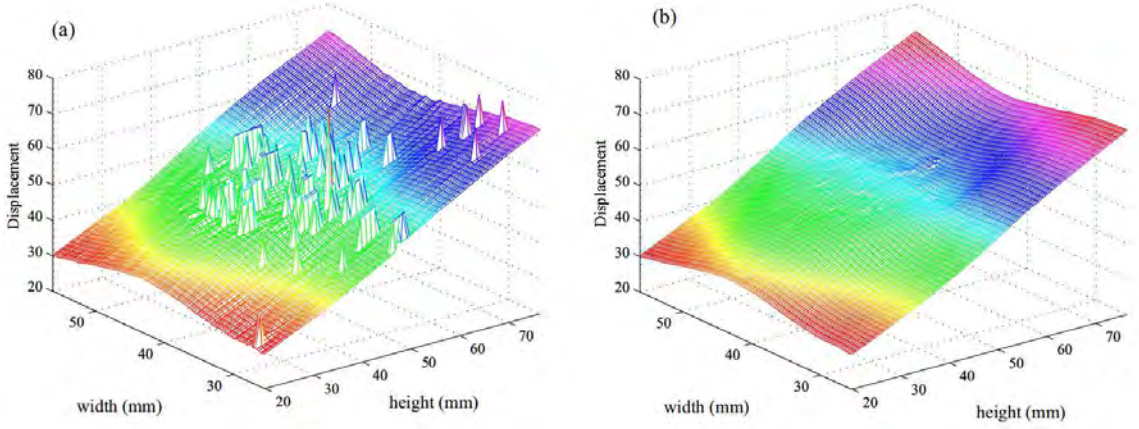
Figure 3.7: Effect of lateral NN factor in the displacement estimation. Displacement images generated by the proposed GBASE method using $L_l = 0$ for 3% applied strain (left image (a)) and the proposed GBASE method using $L_l = 5$ for 3% applied strain (right image (b)).

SNRe [64]:

$$SNRe = \frac{\mu_s}{\sigma_s} \tag{3.19}$$

here, μ_s and σ_s denote the statistical mean and standard deviation of the strain computed in a homogeneous area, respectively.

CNRe [65]:

$$CNRe = \frac{2(\mu_l - \mu_b)^2}{\sigma_l^2 + \sigma_b^2} \tag{3.20}$$

here, μ is the mean strain and σ is the standard deviation of the strain in a homogeneous area. The sub-subscript l and b refer to the lesion and background, respectively.

PSNR:

$$PSNR = 20log_{10}\left(\frac{M_I}{\sqrt{(MSE)}}\right) dB \tag{3.21}$$

where,

$$MSE = \frac{1}{PQ}\sum_{p=0}^{P-1}\sum_{q=0}^{Q-1}[S_X(p,q) - S_Y(p,q)]^2 \tag{3.22}$$

here, $S_X|_{P\times Q}$ and $S_Y|_{P\times Q}$ are the actual and estimated strain images, respectively, and M_I is the dynamic range of the strain image.

MSSIM [66]:

The MSSIM is shown to be an excellent predictor of the image perceptual quality. It considers contrast, luminance and structural similarity between the estimated and actual strain images to compute the value of the index. For calculating the MSSIM index, at first the actual and estimated strain images are locally windowed. Each of the windowed actual and estimated signals, $x(x = [x_1\ x_2.....x_N])$ and $y(y = [y_1\ y_2.....y_N])$, respectively, are of length N. Then these two signal vectors are Gaussian function ($w = [w_1\ w_2.....w_N]$) weighted, with a standard deviation of 1.5 samples, where $\sum_{i=0}^{N} w_i = 1$. Then the estimates of local statistics of x and y are calculated as

$$\mu_x = \frac{1}{N}\sum_{i=1}^{N} w_i x_i, \tag{3.23}$$

$$\mu_y = \frac{1}{N}\sum_{i=1}^{N} w_i y_i, \tag{3.24}$$

$$\sigma_x = \sqrt{\frac{1}{N-1}\sum_{i=1}^{N} w_i(x_i - \mu_x)^2}, \tag{3.25}$$

$$\sigma_y = \sqrt{\frac{1}{N-1}\sum_{i=1}^{N} w_i(y_i - \mu_y)^2}, \tag{3.26}$$

$$\sigma_{xy} = \frac{1}{N-1}\sum_{i=1}^{N} w_i(x_i - \mu_x)(y_i - \mu_y). \tag{3.27}$$

37
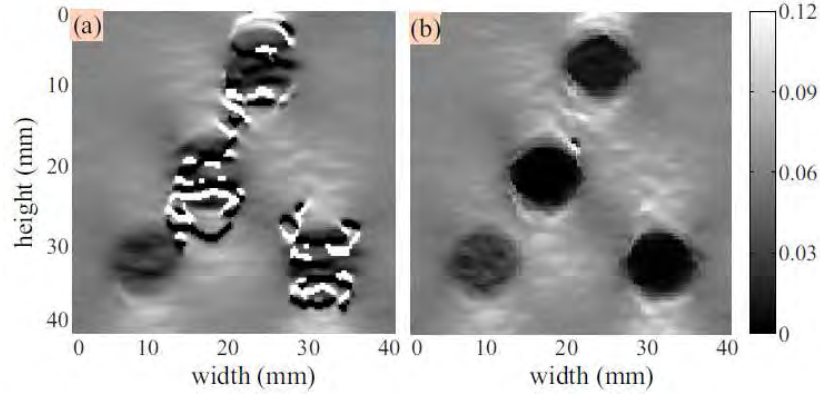
Figure 3.8: Effect of two stretching factors in the strain estimation. Strain images generated by the (a) proposed GBASE method using only one stretching (δ_{avg}) for 4% applied strain, (b) proposed GBASE method using two stretching (δ_{avg} and δ_{max}) for 4% applied strain. For both the cases, Poisson's ration, $\nu = 0.5$ is used.

The *SSIM* index between the signals $x(x = [x_1 \ x_2.....x_N])$ and $y(y = [y_1 \ y_2....y_N])$ is calculated as [66]

$$SSIM = \frac{(2\mu_x\mu_y + C_1)(2\sigma_{xy} + C_2)}{(\mu_x^2 + \mu_y^2 + C_1)(\sigma_x^2 + \sigma_y^2 + C_2)} \tag{3.28}$$

where $C_1 = (K_1M_I)^2$, $C_2 = (K_2M_I)^2$, $K_1 = 0.01$ and $K_2 = 0.03$. Here, M_I is the dynamic range of the pixel values. Finally, the mean *SSIM (MSSIM)* is calculated as:

$$MSSIM = \frac{1}{M}\sum_{j=1}^{M} SSIM(x_j, y_j) \tag{3.29}$$

where x_j and y_j are the image contents at the jth local window and M is the number of local windows in the image.

The four numerical performance metrics are calculated for different applied strains (1%-8%) on 25 realizations of the FEM simulation phantom. The calculated values are graphically presented with error bars in Figs. 4.7(a-g). The SNRe values indicate that our proposed methods (DASE, 2-D DASE and GBASE) perform significantly better than the AS and AM methods. Although the AM method shows better performance than the AS method for up to 2% applied strain, the SNRe of the AM method falls at higher strains. In Fig. 4.7(b), although the PSNR values of the AS method are

better than that of the proposed GBASE method at high strain, the DASE and 2-D DASE methods show significantly better performance. Like the SNRe, the PSNR of the AM method also falls at higher strains. From the MSSIM values in Fig. 4.7(c), we see that the DASE, 2-D DASE methods perform significantly better and the GBASE method performs much better than the AS method. The AM method shows as usual poor performance at higher strains. For the conventional methods, generally there is a decreasing trend of the quality metrics with increasing strain. But the SNRe, PSNR and MSSIM values are more consistent from low to high strains for the proposed DASE and 2-D DASE methods indicating the robustness of the methods to decorrelation noise. In Figs. 4.7(d-g), we plot the CNRe values for four lesions of different stiffness in the FEM phantom. For the 10dB and 20dB lesions (Figs. 4.7(d-e)), CNRe of the proposed GBASE method is comparable to that of the AS method and much better than the AM method; the proposed DASE and 2-D DASE methods significantly outperform the other methods and display an increasing trend in CNRe with the increase of applied strain. However, for the 30dB and 40dB lesions (Figs. 4.7(f-g)), the CNRe values of all the proposed methods show significantly better performance than the AS and AM methods. The results in Figs. 4.7(f-g) also indicate that the GBASE method is particularly suitable for detecting the stiffer lesions. Due to excessive smoothing, the CNRe values of the AM method lie at the bottom. We also observe that the AM method is very sensitive to the tuning parameters' setting. The presented results are due to the choice of most suitable parameters.

For a qualitative evaluation of the perceptual quality of the strain images generated by the AS, AM, and proposed GBASE and DASE methods, we present strain images of the FEM simulation phantom for four (2%, 4%, 6% and 8%) different applied strains in Fig. 5.4. In all the analysis, we have used a data window (L_i) of size 2.28mm and an inter-window shift (L_v) of 0.28mm. We have also used different values of NN factors ($L_a=L_l=1$ and $L_a=L_l=3$) for generating strain images by the DASE method. Thus, for 2% strain, all the methods produce satisfactory images, although the AS and AM methods produce somewhat noisier strain images. For 6% and 8% strains, images generated by the AS method is significantly distorted in left and right boundaries and
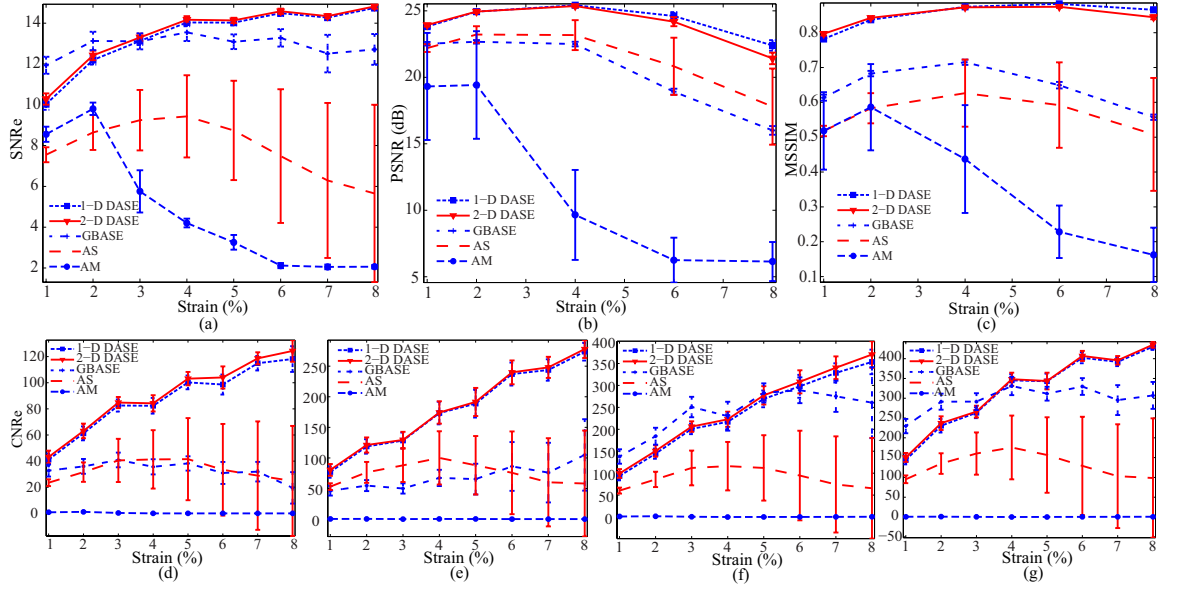
Figure 3.9: Performance comparisons of different methods using numerical performance metrics. (a) SNRe vs. applied strain (b) PSNR vs. applied strain (c) MSSIM vs. applied strain and CNRe vs. applied strain for (d) 10dB (e) 20dB (f) 30dB (g) 40dB lesions.

the strain images generated by the AM method is severely distorted. For the AM method, the inclusions except the 40dB are nearly invisible at higher applied strains. For the AS method, the strain image is noisy at 8% strain and the 10dB and 30dB lesions cannot be clearly observed. The GBASE method produces good "quality" strain images for low strains. At high applied strains, though the inclusion boundaries are distorted, the inclusions are clearly distinguishable from the homogeneous background. In contrast, the DASE method for both NN factors generates very clean strain images at all strains from 2% to 8% indicating the superiority of this method. We notice from these figures that we can control the degree of smoothing by changing the NN and weighting factors which in turn gives us control on spatial resolution. If it is required to increase the spatial resolution, then reducing the value of NN factors will serve the purpose. Though increasing the NN factors reduce somewhat the spatial resolution, the generated strain images for high NN factors are more noise free.

To observe the distortion in the strain image, horizontal 1-D strain profiles are
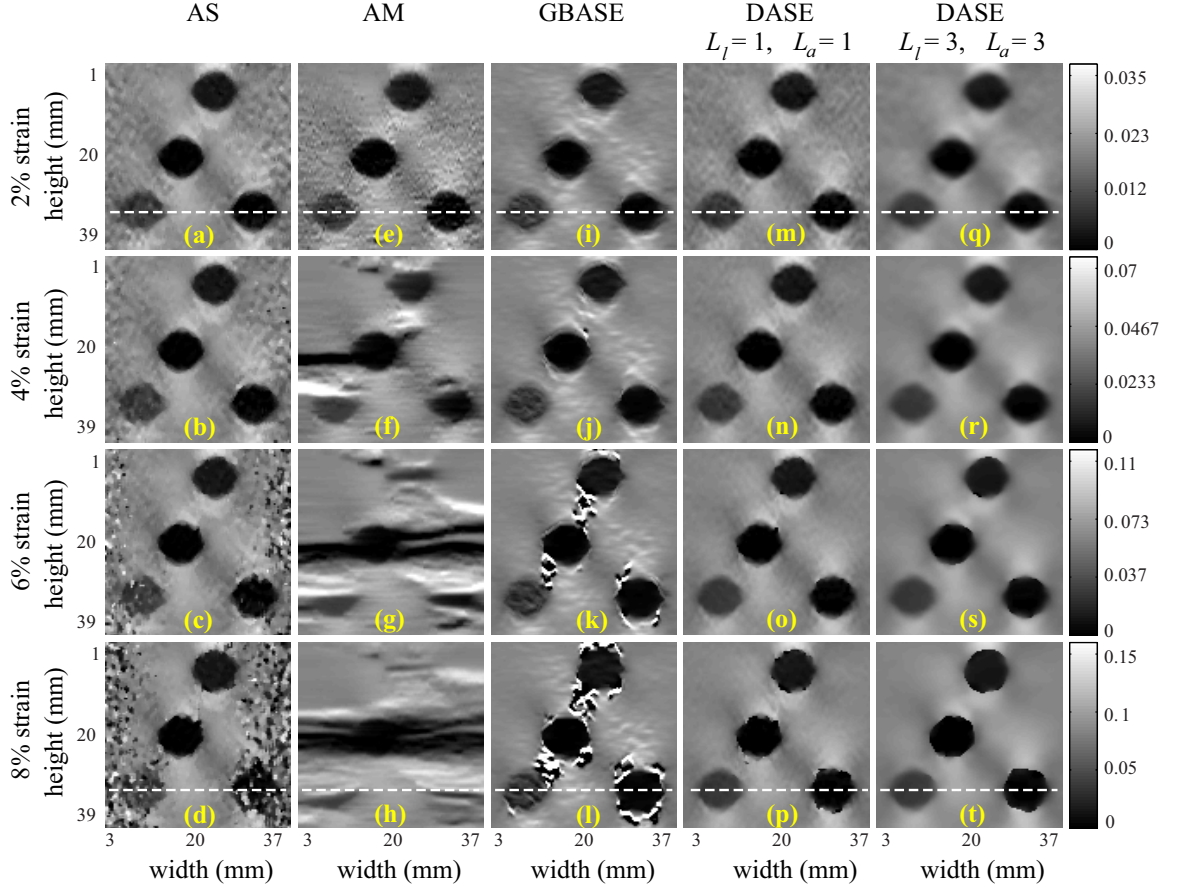
Figure 3.10: Strain images of the FEM simulation phantom generated by different methods. Results (a-d) are produced by the AS, (e-h) are produced by the AM, (i-l) are produced by the proposed GBASE (L_l=3, χ_l=0.25, ν=0.5), (m-p) are produced by the proposed DASE (L_a=1, L_l=1, χ_a=χ_l=0.25, ν=0.5) and (q-t) are produced by the proposed DASE (L_a=3, L_l=3, χ_a=χ_l=0.25, ν=0.5).

depicted for two different applied strains in Fig. 3.11 for the AS, AM and proposed methods. The profiles are selected so that the variation of stiffness in the 10dB and 30dB lesions are included (dashed horizontal line in Fig. 5.3(b)). We have calculated two parameters from this strain plot. The first one is the total MSE between the ideal and the estimated strain profile and the second parameter is the lesion width. The true width of both the lesions is 7.50mm. The estimated values of these quantities by different methods are shown in Tables 5.1 and 5.2 for 2% and 8% applied strain,

41

Table 3.2: Total MSE and lesion width for the 10 and $30dB$ inclusions for 2% applied strain (True lesion width is $7.50mm$)

	Total MSE $(\times 10^{-6})$	Lesion width (mm)	
		10dB	30dB
AS	2.9757	7.50	7.55
AM	11.311	7.56	7.56
GBASE	2.9066	7.55	7.52
DASE with $L_a=L_l=1$	2.1564	7.52	7.53
DASE with $L_a=L_l=3$	1.9411	7.56	7.54

respectively. From Tables 5.1 and 5.2, it is clear that the total MSE is the least for the proposed DASE method with $L_a=L_l=3$ for both the cases. The estimated widths for the 10dB and 30dB lesions are more accurate for the DASE method with $L_a=L_l=1$ and the DASE method with $L_a=L_l=3$ for low strain (2%) and high strain (8%), respectively. We note that the AS method is essentially the DASE method with $L_a=L_l=0$ and $\nu=0$. Thus, use of nonzero NN factors significantly improves MSE. In addition, by decreasing the NN parameters (L_a, L_l) for low strain, we can improve spatial resolution (lesion width) at little cost to MSE. However, due to increased decorrelation noise at high strain, higher L_a and L_l parameters show the best performance. The GBASE method also shows significantly better performance than the AM method. Regarding the gradient-based strain estimation techniques for low strain (2%), although the spatial resolution in terms of lesion widths are slightly better for the GBASE method than the AM method, at high applied strain (8%), the AM method completely fails while the GBASE method performs well.

It can be concluded from the above discussion that we can significantly increase the SNR of the strain images (in turn reduce the MSE) with a little reduction in spatial resolution. Moreover, we can control the degree of the spatial resolution by changing the NN and weighting factors.
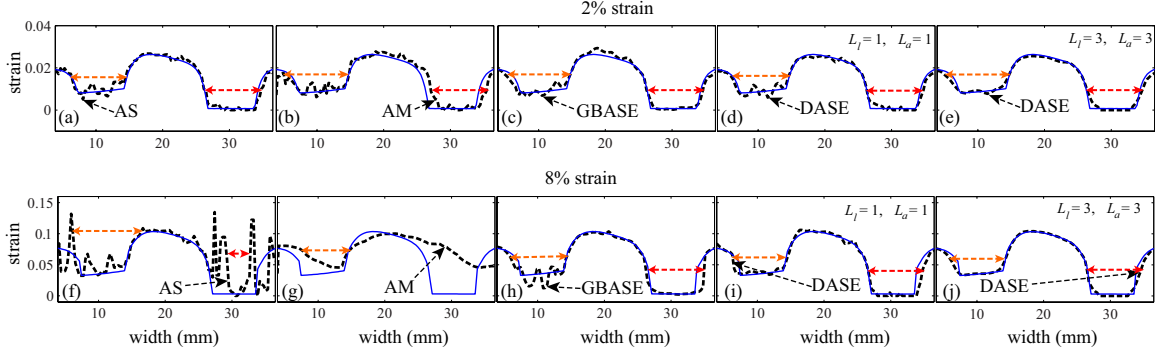
Figure 3.11: Strain curves generated for the FEM simulation phantom at 2% and 8% applied strain by using different methods. (a-e) Lateral strain profile for 2% applied strain at a depth of 30.7mm that includes the 10dB and 30dB inclusions. Comparisons with ideal strain curve are shown for (a) AS (b) AM (c) proposed GBASE (d) proposed DASE for $L_a=L_l=1$, $\nu=0.5$ (e) proposed DASE for $L_a=L_l=3$, $\nu=0.5$. (f-i) Lateral strain profile for 8% applied strain at a depth of 30.7mm that includes the 10dB and 30dB inclusions. Comparisons with ideal strain curve are shown for (f) AS (g) AM (h) proposed GBASE (i) proposed DASE for $L_a=L_l=1$, $\nu=0.5$ (j) proposed DASE for $L_a=L_l=3$, $\nu=0.5$.

3.5.3 Comparison Using Experimental Phantom

We performed elastography experiments with a tissue-mimicking (TM) phantom of dimensions $90 \times 90 \times 120$ mm^3 with a 3-times stiffer (compared to the surrounding) cylindrical inclusion of 2-cm diameter (CIRS, Inc. Norfolk, VA). An ATL (Bothell, WA) Ultramark 9 scanner with a 7.5MHz linear-array transducer was used to acquire RF echo-signals from this CIRS phantom. The RF-echo data were sampled at 20MHz and quantized at 14 bits/sample and we upsampled it to 50MHz prior to processing in the digital domain. Time-gain-control (TGC) data were acquired and before processing the RF data were corrected for TGC in order to simulate the condition in a clinical ultrasound machine. Although TGC is not necessarily a linear function in the way it affects the RF data, the performance of our strain estimator for this phantom data is observed to be very much insensitive to this correction.

Table 3.3: Total MSE and lesion width for the 10 and $30dB$ inclusions for 8% applied strain (True lesion width is $7.50mm$)

	Total MSE $(\times 10^{-6})$	Lesion width (mm)	
		10dB	30dB
AS	100.47	7.58	4.18
AM	113.12	7.04	-
GBASE	11.843	7.56	7.59
DASE with $L_a=L_l=1$	7.0589	7.57	7.58
DASE with $L_a=L_l=3$	3.0905	7.54	7.55

Figs. 4.8(a-p) demonstrate the strain images generated by the AS, AM, proposed GBASE and proposed DASE methods for four different applied external forces. The strain images for four different compressions indicate that the DASE method performs the best amongst all the methods being compared, though some noise is observed in Fig. 4.8(p) at 6% applied strain. In contrast, for 6% applied strain, the AM method generates almost a null image. The strain images produced by the AS and GBASE methods are too noisy at 6% applied strain but perform well up to 4% applied strain.

In Fig. 3.13, we provide a quantitative comparison of the proposed methods with the AS and AM methods for this experimental phantom. Since it is not possible to obtain the ideal strain image for this phantom, the PSNR and MSSIM performance metrics cannot be calculated. Thus, we compare the performances of different methods using SNRe and CNRe. The variation of these two performance metrics are shown in Fig. 3.13 for the proposed, AS and AM methods. The DASE performs the best amongst all other methods for both performance metrics. The GBASE method shows higher SNRe compared to the AS and AM methods, but the CNRe of the AS method is slightly greater than the GBASE method. As evident from Fig. 3.13, the AS, GBASE and DASE methods are all superior to the AM method in terms of both the performance metrics.

44
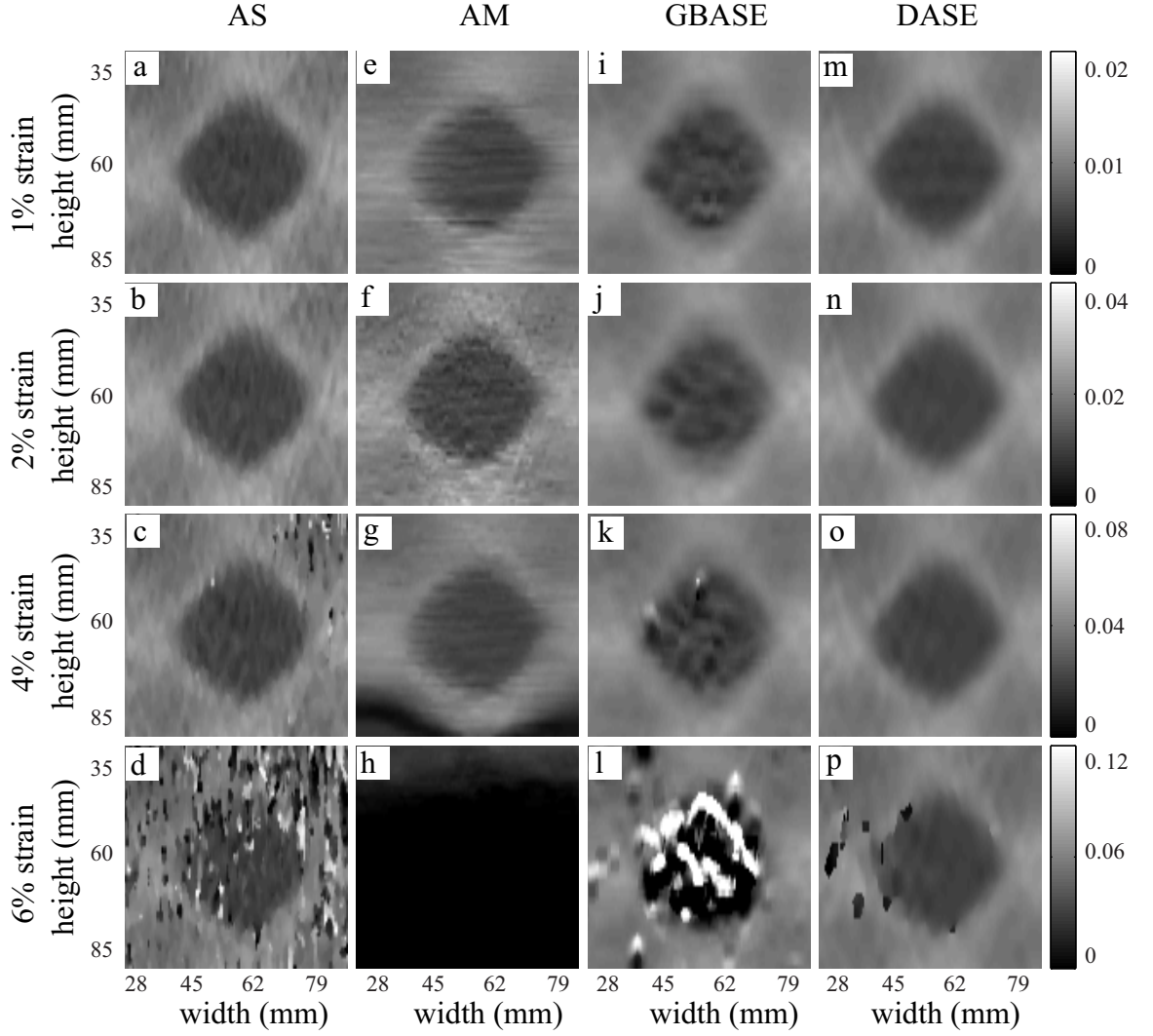
Figure 3.12: Strain images of the experimental phantom generated by different methods. Results (a-d) are produced by the AS method, (e-h) are produced by the AM method, (i-l) are produced by the proposed gradient-based average strain estimation (GBASE) (L_l=3, χ_l=0.25, ν=0.5) and (m-p) are produced by the proposed direct average strain estimation (DASE) (L_a=3, L_l=3, χ_a=χ_l=0.25, ν=0.5).

3.5.4 Comparison Using *In Vivo* Breast Data

The *in vivo* breast data used in the work were chosen from an existing database of 33 cases (age: 20-75 years). These data were acquired with free-hand compression
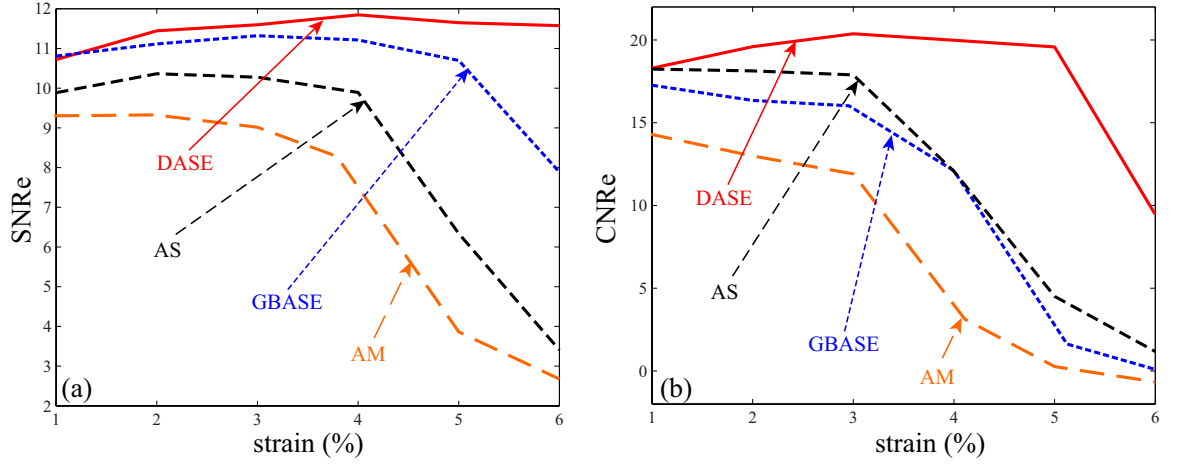
Figure 3.13: Performance comparison of different methods using numerical performance metrics for the experimental phantom data. (a) *SNRe* vs. applied strain, (b) *CNRe* vs. applied strain.

and include both fibroadenomas and cancers. Benign and malignant cases were confirmed by histopathological reports. These data were acquired by using a Sonix SP500 (Ultrasonix Medical Corporation, Richmond BC, Canada) scanner integrated with a L14-5/38 probe operating at 10MHz (nominal) at the University of Vermont Medical Center, USA. The study was approved by the institutional review board (IRB) and informed consent was obtained from every patient. Out of thirty-three cases, four are selected in this work. Three of them represent malignant breast tumors and the other one represents a benign case. The associated B-mode images of patient-I (Age: 28/Tumor type: Fibroadenoma), patient-II (Age: 38/Tumor type: Adenocarcinoma), patient-III (Age: 63/Tumor type: Adenocarcinoma) and patient-IV (Age: 58/Tumor type: Adenocarcinoma) are shown in Figs. 5.7(a), (f), (k), (p), respectively. Malignant breast lesions appear smaller in ultrasonic B-mode images than in elastograms [3]; for fibroadenoma, they generally are larger or similar in size in B-mode images. From Figs. 5.7(a-e), it is clear that the hard lesion size in B-mode and strain images are almost the same as expected. Note that we do not know the approximate applied strain (s_{avg}) for *in vivo* data. To estimate this, we choose a region from the background data and calculate NCC peaks of multiple pre- and post-compression RF echo windows se-

lected from that region for a large range of strain. These peaks are averaged for the corresponding strain value and the position of the maximum average peak is chosen as s_{avg}. Figs. 5.7 (b-e), (g-j), (l-o) and (q-t) show the strain images produced by the AS, AM and proposed GBASE and DASE methods, respectively. We observe from these figures that the AM method can generate a useful strain image only for patients III and IV, though the lesion sizes are not accurate. All the other methods are fairly successful in extracting the lesions from the backscattered ultrasound RF signals for patients I-III. As stated before, the size of the malignant (Adenocarcinoma) object in strain image is found larger than that in the B-mode image for our malignant cases (Figs. 5.7(f), (k), (p)). It is clear that the contrast and boundary of the cancerous tissue in our proposed GBASE method are better than that in the strain images generated by the other algorithms. The proposed DASE method shows the most smooth background with distinguishable lesion compared to the other approaches. The most interesting case in these four patients is the last case (patient - IV). The last patient suffers from adenocarcinoma with a very small lesion. This small lesion is not visible in the B-mode image (Figs. 5.7(p)). We observe that only the GBASE method identifies the lesion clearly and with high contrast, whereas the other methods show the lesion but with an unclear boundary. Note that the strain images for patient IV *in vivo* breast data are estimated at sufficient low strain. Therefore, for the detection of small lesions, GBASE outperforms direct strain estimation methods, e.g., AS and DASE.

We also have plotted the 1-D strain for patients III and IV in Fig. 3.15 for a better understanding of the efficacy of the proposed methods. The height of the lesions mentioned in the histology report are 11mm and 3mm for patient III and IV, respectively. The 1-D strain plot in Fig. 3.15(a) indicates that the strain variation for the AM, proposed GBASE and DASE methods are free from abnormal jump. The width of the strain well for the AM method is smaller than the GBASE and DASE methods which is a clear mismatch with the histology report. It is found from Fig. 3.15(a) that the estimated height of the lesion for the AS, AM, GBASE and DASE methods are 6.17mm, 11.26mm, 11.18mm and 11.28mm, respectively. However, it is almost impossible for an automated detection system to accurately detect the height of the lesion by

the AS method because the AS method produces an abnormal jump inside the strain well. Therefore, it can be said that the proposed methods outperform the AS method in detecting lesions or for estimating the size of the lesions. On the other hand, only the GBASE method demonstrates a clear strain well for patient IV *in vivo* breast data and the estimated lesion height is 3.07mm (close to histology report that reveals 3mm).

3.6 Evaluating Performance In Terms of Computation Time

A comparison of the four (AM, AS, DASE and GBASE) methods in terms of computation time reveals that the displacement based AM method requires the shortest time to generate the strain image. On the other hand, the AS and DASE methods take comparatively greater time than that of GBASE method. The computation time (CPU: Core 2 Duo, 2.5GHz, RAM: 2 GB, software: MATLAB®) of our implementation of the AM, AS, DASE and GBASE methods for generating the strain images (*in vivo* breast experiment: Patient I) are 1.41 sec, 197.83 sec, 200.47 sec and 31.87 sec, respectively. Note, however, that the AM method uses mex files but the others do not.

3.7 Conclusions

In this chapter, we have discussed two novel methods for the estimation of average displacement and strain in the time domain. We have shown that the average displacement and strain can be estimated by maximizing our proposed weighted cost function derived from the information of the neighboring windowed RF echoes. The effect of considering the lateral shift in the selection of 1-D RF pre- and post-compression segments has been also demonstrated for DASE as well as GBASE methods. Though the DASE method generally produces higher quality strain images, the GBASE technique is more computationally efficient. Moreover, the GBASE technique, unlike the conventional gradient based strain estimators, images the hard inclusions accurately. We also have used a 2-D signal window to implement a 2-D DASE method. For the 2-D

Patient I: 28/Fibroad, Patient II: 38/Adenocar, Patient III: 63/Adenocar, Patient IV: 58/Adenocar
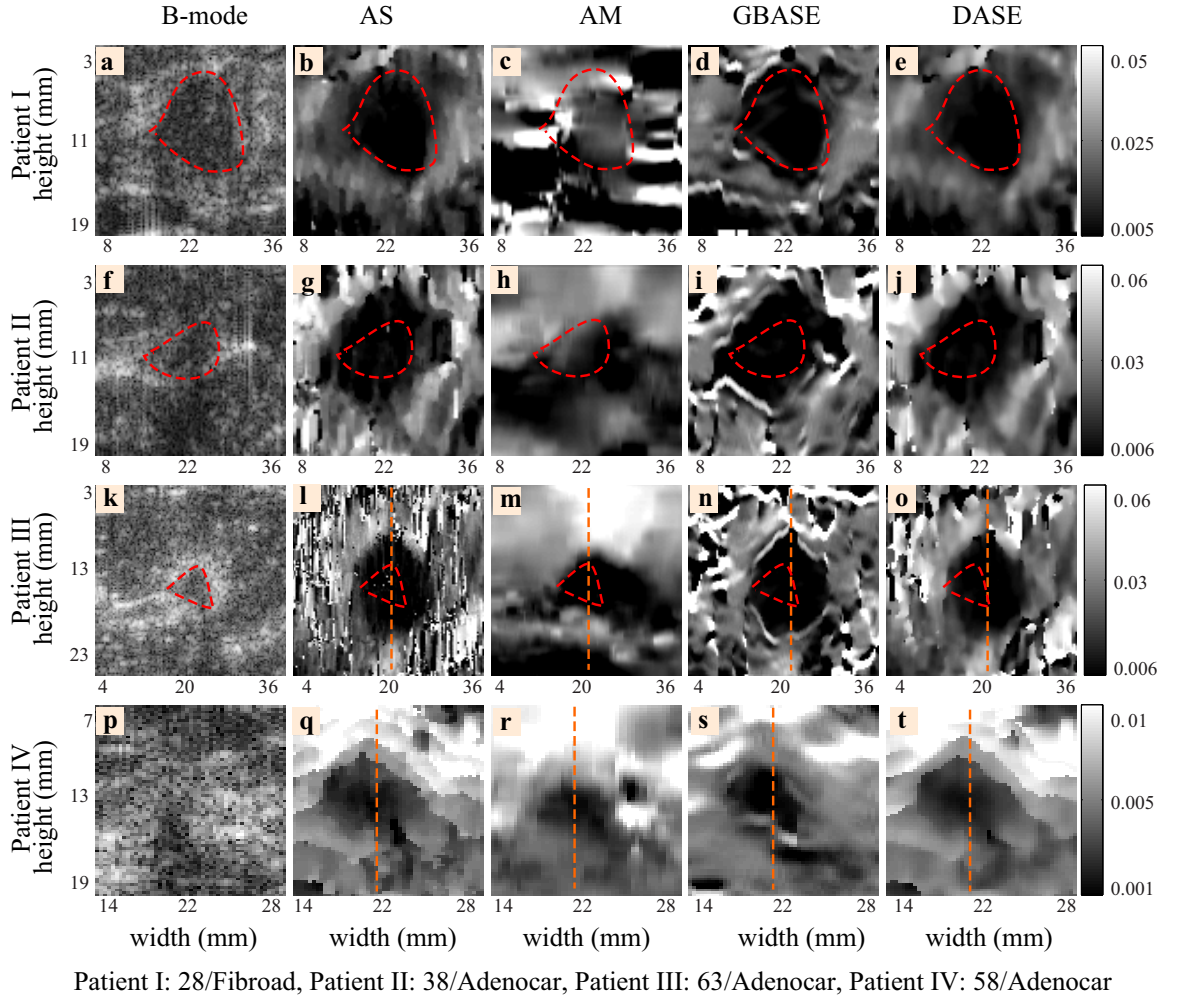
Figure 3.14: Strain images generated by different methods using *in vivo* breast ultrasound data. (a), (f), (k), (p) represent B-mode images of four patients. Results (b), (g), (l), (q) are produced by the AS method; (c), (h), (m), (r) are produced by the AM method; (d), (i), (n), (s) are produced by the proposed GBASE (L_l=3, χ_l=0.25, ν=0.5) and (e), (j), (o), (t) are produced by the proposed DASE (L_a=3, L_l=3, χ_a=χ_l=0.25, ν=0.5). The red dashed contours are drawn to compare the lesion sizes exposed in strain images with that of their corresponding B-mode images. For patient IV the shape of the lesion is not understood. The size of the malignant objects in the strain images are larger than that in the corresponding B-mode images.
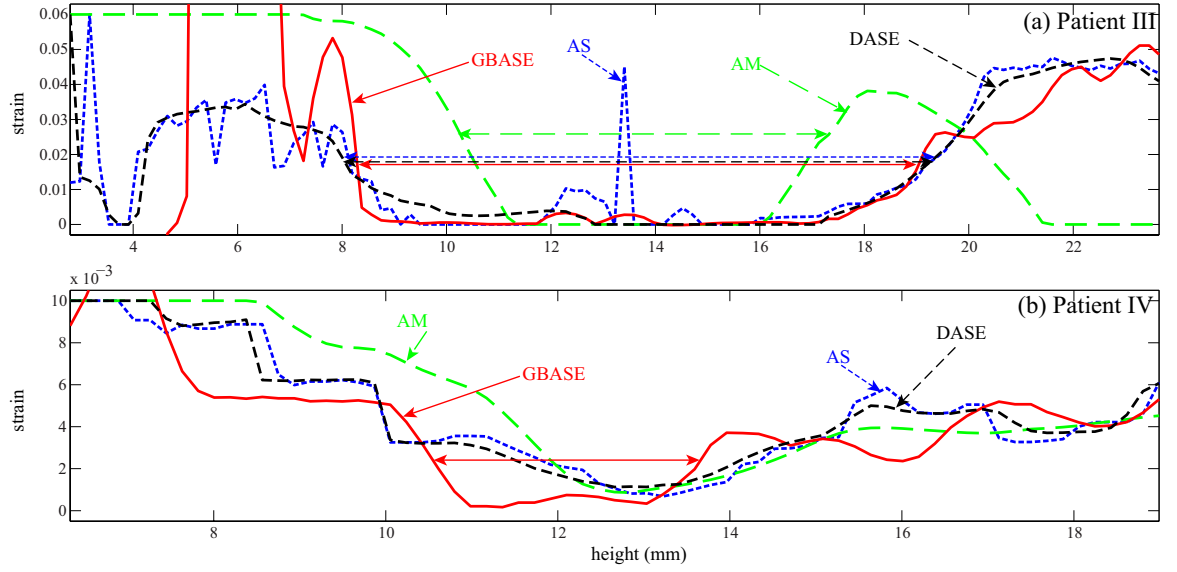
Figure 3.15: Strain curves obtained for patients III and IV *in vivo* breast data by using different methods. Axial strain profile in an arbitrary scan line including the inclusion (as marked in Fig. 5.7). Estimated height of the lesion of patient III for the AS, AM, GBASE and DASE methods are 6.17mm, 11.26mm, 11.18mm and 11.28mm, respectively. The height of the lesion mentioned in the histology report is 11mm. On the other hand, only the GBASE method shows a clear strain well for patient IV and the lesion height is found to be 3.07mm (close to the histology report that reveals 3mm).

DASE method, we have plotted the numerical performance metrics and have seen that the 2-D DASE performs better than the DASE method though it has higher computational complexity. However, it has been shown by simulation and experimental results that the proposed two methods are more robust for a wide range of strain values than the comparing techniques. We have shown strain profiles for the FEM phantom and calculated the overall MSE which depict the superiority of our proposed methods over the other reported techniques. We also have plotted the strain profiles for very small and larger *in vivo* breast lesions where lesion dimensions estimated by our proposed methods matched well with that of the histology. Furthermore, only the proposed GBASE method successfully depicted the tiny lesion with correct dimension. The val-

50

ues of the quantitative performance metrics for the FEM and experimental phantom also indicate that the proposed methods generate higher quality and higher SNR strain images than the techniques compared with in this paper. The salient feature of our technique is that, due to robustness to signal de-correlation, the stiff masses can be clearly viewed in the strain image and the lesion boundary can also be more clearly identified compared to the other methods.

Chapter 4

Robust Strain Estimation Using Combined RF and Envelope Cross-correlation

4.1   Introduction

In quasi-static elastography, some reported strain estimators use only the envelope signal or the RF signal in conjunction with the envelope for strain estimation [55]-[58]. [55] discuss a theoretical framework for envelope cross-correlation based strain estimation by characterizing the noise performance and demonstrates a composite strain filter approach to increase the dynamic range in the elastogram by using a combination of RF and envelope signals to estimate strain. [56] uses the pre- and post-compression envelope window cross-correlation to calculate the sparse displacement (seed) in the tissue at the preliminary stage and in the subsequent stages the primary seeds are used to track the displacement in a gradual finer grid by using envelope cross-correlation. In [57], downsampled 2-dimensional envelope signal is used to track the tissue motion upon physical compression and using the tracking, strain is calculated from the 2-dimensional pre- and post compression rf echo cross-correlation. But according to [55], strain estimation variance is high and SNRe is low for the envelope signal compared

to that of the RF signal at low strain. So, the preliminary estimated seeds or tracking parameters used in [56] and [57] may be misleading at low strain. [58] uses RF auto-correlation to find phase shift followed by unwrapping it by the extracted information from envelope cross-correlation.

In this chapter, we propose a novel approach for robust strain estimation using a combined piecewise-linear-weighted RF normalized cross-correlation (NCC) and envelope NCC followed by denoising by a diffusion filter. Displacement map computed from the RF echo NCC is known to be "clean" at low strain while very noisy at high strain due to echo decorrelation. On the other hand, displacement map computed from the envelope NCC is less precise and often noisy at low strain while robust to echo decorrelation noise at high strain. Our novel algorithm combines the advantages of both the approaches by defining an applied-strain dependent piecewise linear weight via which the RF and envelope NCC functions are added to find the final peak. As by the increase of applied strain echo decorrelation increases, therefore, in the "addition" operation, contribution of the RF NCC and envelope NCC functions are controlled by a weight that depends on strain and consequently, decorrelation noise. Instead of a single global stretching, we use non-stretched and globally stretched post-compression RF echo windows with pre-compression counterpart RF window to find the NCC peak to account for the fact that the RF signal experiences less or no compression in the lesion volume. We also estimate and correct for lateral shift by using the Poisson's ratio [67]. Finally, we introduce the diffusion filtering in the field of elastography. A geometric non-linear diffusion filtering [71] is performed on the calculated strain image. To demonstrate the efficacy of our algorithm, we evaluate and compare the performance of our algorithm with other reported algorithms using the simulation data by FEM, experimental phantom data, and *in vivo* breast data.

4.2 The Signal Model

The backscattered ultrasound RF signals before and after compression can be written in the simplified 1-D form as [36]:

$$r_1(t) = s_1(t) + v_1(t) = s(t) \otimes p(t) + v_1(t) \tag{4.1}$$

$$r_2(t) = s_2(t) + v_2(t) = s\left(\frac{t}{a} - t_0\right) \otimes p(t) + v_2(t) \tag{4.2}$$

where, $r_1(t)$ and $r_2(t)$ represent, respectively, the pre- and post-compression RF echo signals, $s(t)$ represents the 1-D ultrasound scattering function, $p(t)$ represents the point spread function (PSF), a represents the compression factor caused by axial-mechanical pressure to the medium, $v_1(t)$ and $v_2(t)$ are the uncorrelated random noise profiles and $\otimes$ represents the convolution operation. The strain ϵ is related to the compression factor $1/a$ as [28],

$$\epsilon = 1 - a \tag{4.3}$$

where, $a \leq 1$ and $\epsilon << 1$.

4.3 Strain Estimation

Let $RF_1(i,j)$ and $RF_2(i,j)$ be the pre- and post-compression RF echo frames, respectively. i represents the axial depth index and j represents RF A-line index. Strain at a particular point on the strain map (i_s, j_s) is calculated from a corresponding pair of 1-D windowed pre- and post-compression RF segments, $r_1^{(i_s,j_s)}$ and $r_2^{(i_s,j_s)}$, respectively. These segments are selected as,

$$r_1^{(i_s,j_s)}(i) = RF_1((i_s - 1)D_v + i, j), \tag{4.4}$$

$$\text{for } 1 \leq i \leq L_i \text{ and } j = j_s$$

$$r_2^{(i_s,j_s)}(i) = RF_2(round((i_s - 1)(1 - s_{ap})D_v) + i, j), \tag{4.5}$$

$$\text{for } 1 \leq i \leq L_i \text{ and } j = j_s + (j_s - \frac{N_a}{2})s_{ap}\nu_v$$

where, s_{ap} represents the approximate applied strain, N_a represents the total number of A-lines in the ultrasound images, D_v represents the distance between samples of the two RF echo segments in the axial direction and L_i represents the length of the 1-D rf window. The axial mechanical stress causes a lateral shift of tissue segments. So, the value of j in $r_2^{(i_s,j_s)}$ deviates from actual j_s. Therefore, the Poisson's ratio is used to interpolate the post-compression data window for reducing the lateral shift effect in axial strain calculation. It is assumed that the center A-line (i.e., $round(N_a/2)$) experiences no lateral shift but the zero-lateral-shift line may differ slightly from a straight line and may not go through the middle exactly.

Before displacement estimation, global stretching on post-compression signal window is performed to reduce decorrelation noise. If the post-compression signal is stretched by a factor α, then Eq. (4.2) yields [36],

$$\begin{aligned}
r_\alpha(t) = r_2(\alpha t) &= s_\alpha(t) + v_\alpha(t) \\
&= s\left(\frac{\alpha}{a}t - t_o\right) \otimes p(\alpha t) + v_2(\alpha t) \tag{4.6}
\end{aligned}$$

In a similar fashion, after stretching the post-compression echo window $r_2^{(i_s,j_s)}$ by a factor α (≤ 1), i.e., $r_\alpha^{(i_s,j_s)}(i) = r_2^{(i_s,j_s)}(\alpha i)$, the NCC coefficient $\rho_\alpha^{rf}(k)$ between $r_1^{(i_s,j_s)}$ and $r_\alpha^{(i_s,j_s)}$ is calculated as [61],

$$\rho_\alpha^{rf}(k) = \frac{\sum_{i=1}^{L_i} r_1^{(i_s,j_s)}(i) \cdot r_\alpha^{(i_s,j_s)}(i + k)}{\sqrt{\sum_{i=1}^{L_i} \{r_1^{(i_s,j_s)}(i)\}^2 \sum_{i=1}^{L_i} \{r_\alpha^{(i_s,j_s)}(i)\}^2}}$$

$$\tag{4.7}$$

Eq. (4.7) becomes maximum for $\alpha = a$ with the approximation of $p(\alpha t) \cong p(t)$. This approximation is valid for lower applied strain. If the effect of PSF could be analyzed at higher strain then the bias in the strain estimates could be removed. However,

lesion area experiences much less or no compression depending on the stiffness of the mass. Therefore, to image the lesion boundary well, global stretching is to be avoided in the lesion area. As the position of the lesion is normally unknown, therefore, we take an approach to calculate NCC of pre- and post-compression signal windows with and without global stretching. We use two different values of α (i.e., $\alpha_{max} = 1$ and $\alpha_{ap} = 1 - s_{ap}$) for stretching the post-compression signal to compute the NCC $\rho_\alpha(k)$.

We compute the envelopes of the interrogative pre- and post-compression (stretched and non-stretched) data windows using the Hilbert transform (Eqs. (4.8) & (4.9)). Due to its asynchronous nature, Hilbert transform does not need the center frequency of the ultrasound system to compute the envelope.

$$e_1^{(i_s,j_s)}(i) = |Hilbert[r_1^{(i_s,j_s)}(i)]| \tag{4.8}$$

$$e_\alpha^{(i_s,j_s)}(i) = |Hilbert[r_\alpha^{(i_s,j_s)}(i)]| \tag{4.9}$$

where, $Hilbert$ denotes the Hilbert transform. Like Eq. (4.7), the envelop NCC function $\rho_\alpha^{env}(k)$ is calculated as,

$$\rho_\alpha^{env}(k) = \frac{\sum_{i=1}^{L_i} e_1^{(i_s,j_s)}(i) \cdot e_\alpha^{(i_s,j_s)}(i+k)}{\sqrt{\sum_{i=1}^{L_i} \{e_1^{(i_s,j_s)}(i)\}^2 \sum_{i=1}^{L_i} \{e_\alpha^{(i_s,j_s)}(i)\}^2}}$$

For robust strain estimation, we add weighted NCC functions $\rho_\alpha^{rf}(k)$ and $\rho_\alpha^{env}(k)$ computed for the same interrogative data windows to generate a true peak. A piecewise linear weight LW is defined from our observation to control the contribution of RF and envelope NCC functions in the combined NCC function. It is to be noted that the amount of echo decorrelation due to increase of the applied strain may depend on the data types (e.g., computer simulated phantom, tissue mimicking phantom, $in\ vivo$ patient data, etc.). However, at a very low strain, RF NCCF alone works better than the sum. The effectiveness of using the weighted summation of the RF NCCF and envelope NCCF are illustrated in Fig. 4.1. A particular point on the strain map is chosen from the homogeneous background of the FEM simulation phantom. The RF NCCF, envelope NCCF, and the sum of the equally weighted RF and envelope NCCFs
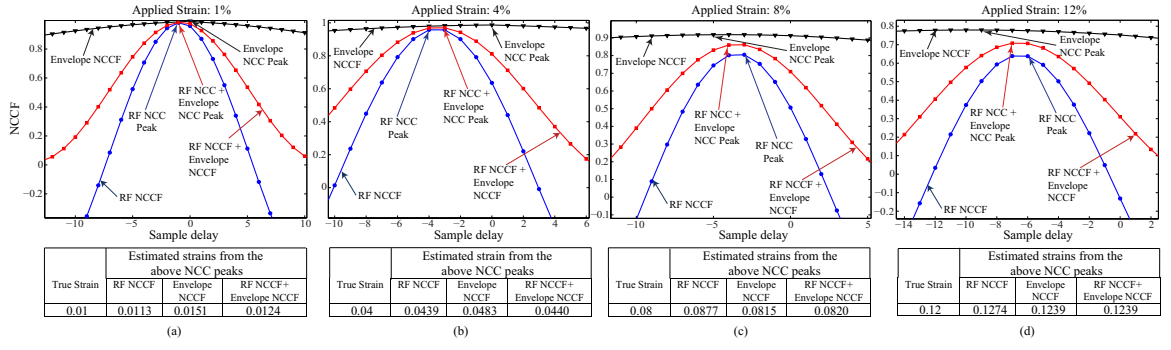
Figure 4.1: Zoomed views of the normalized cross-correlation functions (NCCF) *vs* sample delay for a particular point on the strain image of the FEM phantom at (a) 1%, (b) 4%, (c) 8% and (d) 12% strain. The point is chosen from the homogeneous background. Corresponding true and calculated strain values are also shown in tabular form at the bottom of the respective NCCF plot.

of that particular point are plotted for 1%, 4%, 8% and 12% applied strain in Figs. 4.1(a-d), respectively. The strain values calculated from these plotted peaks of the RF NCCF, envelope NCCF, and the sum of the equally weighted RF and envelope NCCFs are shown at the bottom of each plot. We can see from Figs. 4.1(a-d) that with the increase of applied strain, the RF NCCF estimate of the strain deteriorates. In contrast, the envelope NCCF generates strain closer to the true value with the increase of the applied strain. Consequently, the sum of the weighted RF NCCF and envelope NCCF generates better strain values than that of the RF NCCF at high applied strain. We can also see from Figs. 4.1(c-d) for 8% and 12% applied strains that the peaks of the RF NCC falls below 0.9 which is a clear depiction of the increased echo decorrelation.

Considering the above discussed facts, a piecewise linear weight (LW) is defined as (details are discussed in the result section),

$$LW = \begin{cases} 0 & \text{for} \quad s_{ap} \leq s_{knee} \\ \frac{0.5(s_{ap}-s_{knee})}{s_{max}-s_{knee}} & \text{for} \quad s_{knee} < s_{ap} \leq s_{max} \\ 0.5 & \text{for} \quad s_{ap} > s_{max} \end{cases} \quad (4.10)$$

Here, s_{knee} denotes the "knee strain", s_{max} denotes the maximum strain and s_{ap} denotes the approximate applied strain.

57

Using *LW*, the robust NCC function $\rho_\alpha(k)$ is calculated as,

$$\rho_\alpha(k) = LW \times \rho_\alpha^{env}(k) + (1 - LW) \times \rho_\alpha^{rf}(k) \tag{4.11}$$

From the NCC functions, the discrete time-lag is calculated as,

$$k_\alpha^{(i_s,j_s)} = \arg\max_k\{\rho_\alpha(k)\}, \quad \text{for} \quad \alpha = \alpha_{max} \ \& \ \alpha_{ap}$$

We use parabolic interpolation algorithm to calculate the sub-sample time-lag values. Finally, the displacement is calculated as,

$$D(i_s, j_s) = \begin{cases} k_{\alpha_{ap}}^{(i_s,j_s)} + k_{comp} + \frac{L_i}{2}s_{ap} & \text{for} \quad \beta \geq \gamma \\ k_{\alpha_{max}}^{(i_s,j_s)} + k_{comp} & \text{for} \quad Otherwise \end{cases} \tag{4.12}$$

where, $\beta = \rho_{\alpha_{ap}}^{(i_s,j_s)}(k_{\alpha_{ap}}^{(i_s,j_s)})$, $\gamma = \rho_{\alpha_{max}}^{(i_s,j_s)}(k_{\alpha_{max}}^{(i_s,j_s)})$ and $k_{comp} = round((i_s - 1)\alpha_{max}D_v) - (i_s - 1)D_v$. k_{comp} is the displacement compensated in the shifting operation $(1 - s_{ap})$ for the window selection in Eq. (5.4). The compensated displacement in the stretching operation of the post-compression signal before cross-correlation operation is reinstated by $(\frac{L_i}{2}s_{ap})$ in Eq. (4.12). Finally, from the displacement map $D(i_s, j_s)$, strain $S(i_s, j_s)$ is calculated using the least-square-error based strain estimation method [52] with 4-points per strain estimate.

4.4 Diffusion Filtering

In this thesis, we also introduce diffusion filtering in elastography for strain image denoising. Preserving the lesion edge while denoising is very important in the field of medical imaging. Diffusion filter performed well in this regard in the field of X-ray and CT imaging. Here, we use the geometric non-linear diffusion filter [71]. The strain image update equation is,

$$\begin{aligned} I_S^n &= I_S^{n-1} + \triangle t[C(D_x, P_x) \cdot (\nabla_E + \nabla_W) \\ &+ C(D_y, P_y) \cdot (\nabla_N + \nabla_S)]^{n-1} \end{aligned}$$

Here, I_S^0 is the original strain image and $I_S^n (n > 0)$ is the diffused strain image at the nth step, $\nabla_p = I_p - I_S (p = E, W, N \text{and} S)$ denotes the difference between the interrogative pixel and one of the east, west, north, and south pixels, respectively, n is the iteration number, $\triangle t$ is the integration constant and C is the sigmoid diffusivity function defined as,

$$C(D_a, P_a) = \frac{1}{1 + \exp\{(-|P_a| - |D_a|) \times 50\}}$$

where, a represents x or y directions, D_a denotes the a-directional intensity difference in a 3×3 window and P_a is defined from D_a depending on a threshold value of the image intensity of the interrogative pixel [71]. We use $1 \leq n \leq 10$ and $\triangle t = 0.15$.

4.5   Simulation and Experimental Results

In this section, at first we define the piecewise linear weight to be used in strain calculation for different types of data. In the subsequent subsections, we show the efficacy of using the Poisson's ratio and provide comparative results of our proposed method with the novel spline-based approach for robust strain estimation in elastography (SBSE) [47] and ultrasound elastography performance enhancement using wavelet denoising (UPWD) [68] method using the FEM phantom, CIRS experimental phantom and the *in vivo* patient data. In addition to subjective evaluation by visual inspection, we compare the performances of different methods in terms of several numerical indices: elastographic signal-to-noise ratio (SNRe) [64], elastographic contrast-to-noise ratio (CNRe) [65] and mean structural similarity (MSSIM) [66].

4.5.1   Piecewise Linear Weight

We observed in our investigation that equal weight to both the RF NCCF and envelope NCCF works the best at high strain. The maximum value of the strain (defined as s_{max} in eqn. (5.9)) may be assumed to be equal or greater than 0.1, 0.05 and 0.03 for the FEM simulation, experimental phantom and *in vivo* breast data, respectively, as greater than these values might be unrealistic for each of the cases. However, at
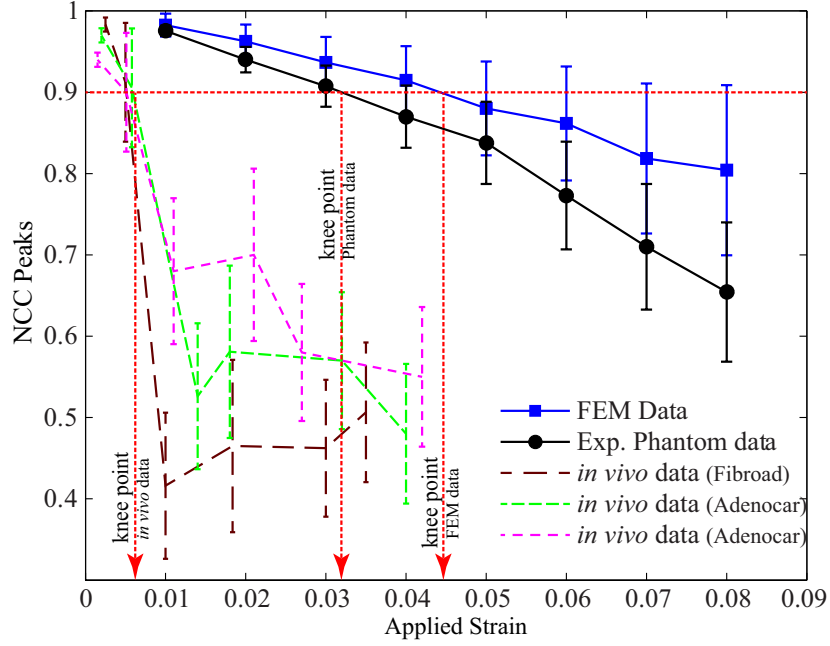
Figure 4.2: Representation of the Normalized cross-correlation (NCC) peaks *vs* applied strain for the FEM phantom, experimental phantom and *in vivo* data. By taking NCC peak value 0.9 as threshold, some "knee" strain points are defined for the FEM phantom, experimental phantom and *in vivo* data.

a low strain, the RF NCCF alone works better than the sum. Therefore, we define some "knee" strain points for the FEM phantom, experimental phantom and *in vivo* data in terms of the NCC peaks, and the envelope NCCF is to be added with the RF NCCF for better strain estimation only when the applied strain is greater than this "knee" value. For defining the "knee" for a particular data type, NCC peaks are calculated for an arbitrarily selected background region of the respective strain map. We know that, with the increase of applied strain, echo decorrelation increases by different rates depending on the data types, and consequently, the NCC peaks falls off rapidly. We choose 0.9 as the NCC peak threshold and the "knee" point is defined as that particular value of the applied strain, greater than which the NCC peak falls below this threshold (see Fig. 4.2). However, the envelope NCC peak may be greater than 0.9 for a large range of the applied strain, even for the strain greater than the

60

knee point for all the three types of data. But the peak position is not enough precise at a low strain, thereby leading to a very noisy strain image. To define a "knee" point for the *in vivo* data in Fig. 4.2, we use 3 patient cases where one is Fibroadenoma and two are Adenocarcinoma cases.

Figure 4.3: Graphical presentation of the piecewise linear weight (LW) for different data types at different percentages of the applied strain.

In Fig. 4.3, the piecewise linear weight is graphically presented and from this figure, "knee strain" can be assumed to be 0.045, 0.03 and 0.005 for the FEM phantom, experimental phantom and *in vivo* data, respectively.

4.5.2 FEM Simulation

A rectangular phantom of 40mm × 40mm dimensions was simulated using finite-element (FEM) analysis software Algor (Algor, Inc., Pittsburgh, PA). It has homogeneous background with the stiffness of 60kPa. 60kPa stiffness is close to the average stiffness of normal glandular tissue in the breast [69]. The phantom has four circular inclusions of 7.5mm diameter each (Fig. 5.3(a)). The bottom left, top, bottom right

Figure 4.4: (a) FEM simulation phantom. It contains four stiff inclusions in a homogeneous background of 60kPa. (b) Corresponding ideal elastogram.
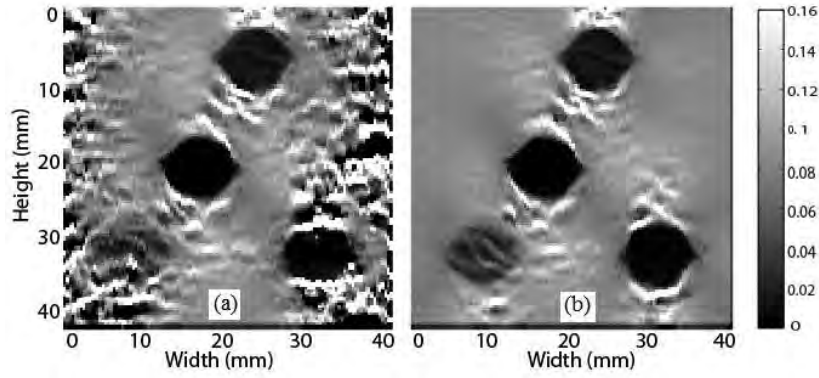
Figure 4.5: Effects of using Poisson's ratio at 8% strain. Strain images generated (a) without using Poisson's ratio and (b) using Poisson's ratio.

and middle inclusions were 10, 20, 30 and 40dB (or 3.16, 10.00, 31.62 and 100.00 times) stiffer than the background, respectively. The bottom of the phantom was placed on a planar surface and the phantom was in full-slip condition. During the simulation, the Poisson's ration was used as 0.495. The phantom was scanned from the top with a probe of center frequency, $f_0 = 5$MHz and band-width $= 60\%$. A non-diffracting transducer beam was simulated with a beam width of 1.5mm. The total number of A-line was 128. White noise of random nature was added to simulate a sonographic

62
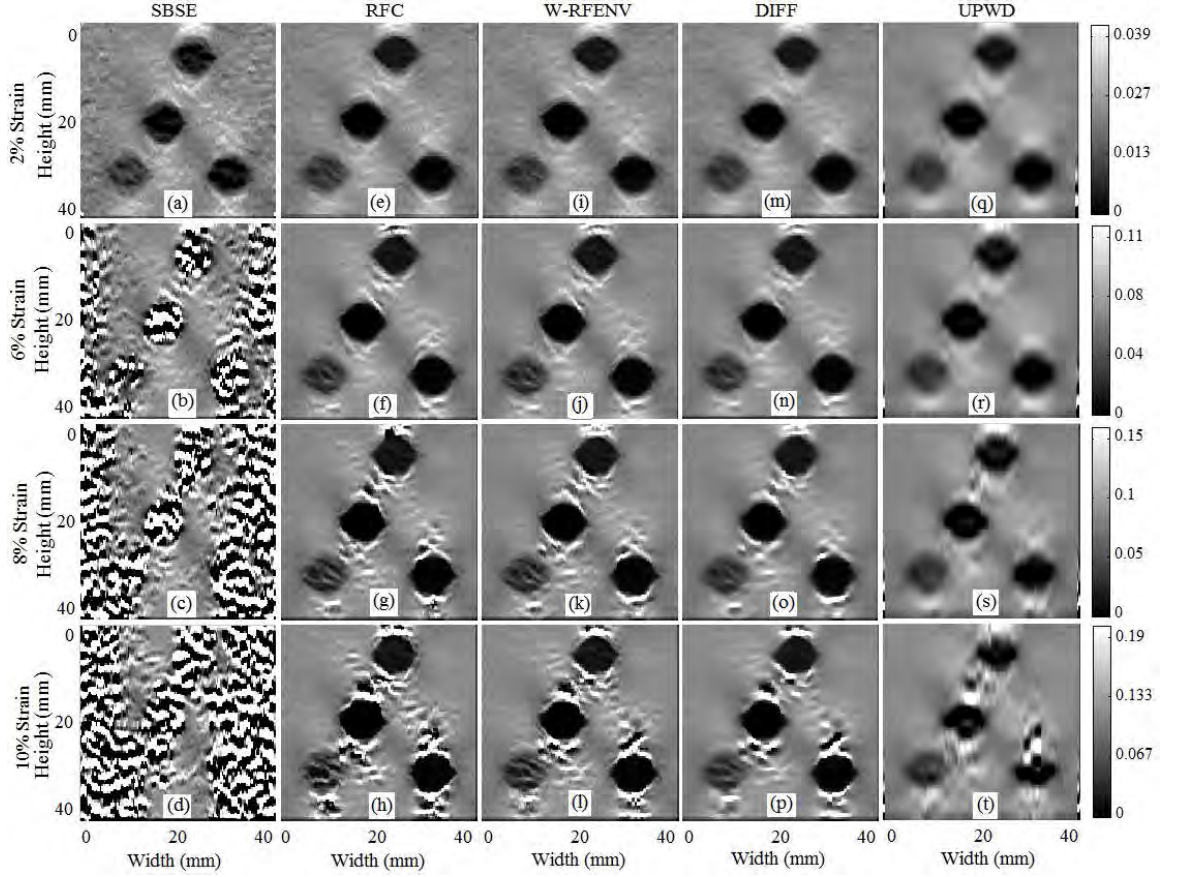
Figure 4.6: Strain images of the FEM simulation phantom generated by different methods. Results (a-d) are produced by the SBSE [47], (e-h) are produced by the RFC ($\nu_v = 0.5$), (i-l) are produced by the W-RFENV ($\nu_v = 0.5$), (m-p) are the diffusion filtered images of (i-l) and (q-t) are produced by the UPWD [68].

SNR of 40dB [47]. Fig. 5.3(b) represents the ideal elastogram for a 2% applied strain.

To show the effect of using the Poisson's ratio for strain estimation, we generate two strain images at 8% applied strain in Fig. 4.5. It is clear from Fig. 4.5(a) that it is very noisy in both the left and right sides due to which lesion edges at bottom are not clearly visible. On the other hand, Fig. 4.5 (b) does not suffer from the same noise.

In Fig. 5.4(a-t), we show the strain images generated by the SBSE, eqn. (4.12) with RF NCC (RFC), eqn. (4.12) with weighted RF and envelope NCC (W-RFENV), proposed DIFF method (W-RFENV with diffusion filtering) and UPWD with W-

RFENV as the basic method for four different applied strains. In all the methods, we have used a data window (L_i) size of 2.28mm and an inter-window shift (D_v) of 0.28mm. From these figures it is easily observable for 2% strain that the SBSE produces somewhat noisy strain image in contrast to the images formed by the proposed method. The distortion is severe in Figs. 5.4(b-d) for 6%-10% strains, respectively and the inclusions disappear. The strain image for the RFC method is degraded by noise at 8% and 10% strains. On the contrary, the W-RFENV method generates very clean strain image at all strain from 2% to 8% while a little noisy at 10% indicating the superiority of this method. The diffusion filtered strain images produced by the W-RFENV method (DIFF) are the best for each of the strain cases and the background has become almost smooth with each of the lesions edges preserved. The wavelet based UPWD method smoothes all the images without lesion edges preserved.
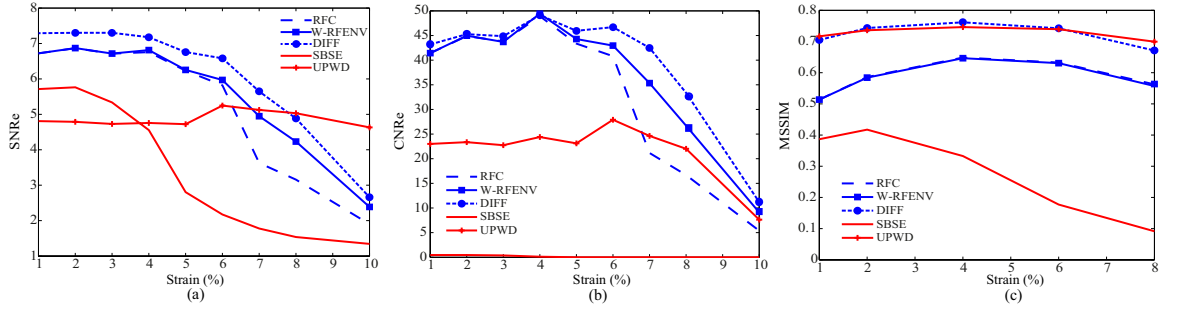
Figure 4.7: Performance comparisons of different methods using numerical indices. (a) SNRe vs. applied strain (b) CNRe vs. applied strain and (c) MSSIM vs. applied strain.

Three numerical indices e.g., the elastographic signal-to-noise ratio (SNRe), the elastographic contrast-to-noise ratio (CNRe) and the mean structural similarity (MSSIM) are graphically presented to evaluate the strain image quality generated by the SBSE, RFC, W-RFENV, DIFF and UPWD with the basic method W-RFENV. In SNRe plot, the W-RFENV shows better performance than the RFC at high strains and the DIFF can be said the best among all the methods. Although the UPWD shows better performance but it does not preserve the lesion edges at all (Fig. 5.4(s-t)). In CNRe plot,
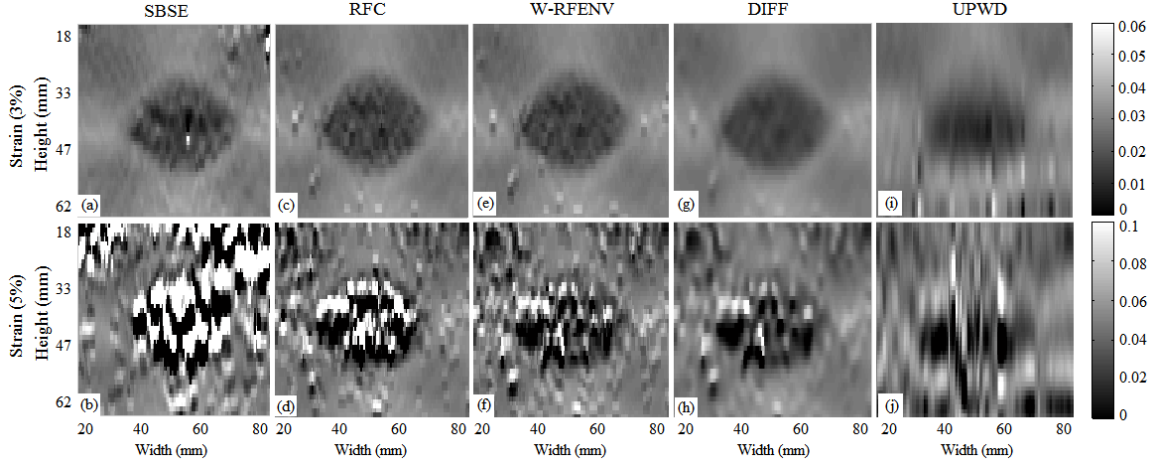
Figure 4.8: Strain images of the CIRS experimental phantom generated by different methods. Results (a-b) are produced by the SBSE, (c-d) are produced by the RFC ($\nu_v = 0.5$), (e-f) are produced by the W-RFENV ($\nu_v = 0.5$), (g-h) are the diffusion filtered images of (e-f) (DIFF) and (i-j) are produced by the UPWD.

the W-RFENV shows better performance than the the RFC at higher strains and the DIFF shows the expected best performance but the UPWD makes the performance worse than its basic method while the SBSE is at the bottom. In MSSIM plot, although the DIFF and UPWD are close, the latter has bad impact on the lesion edges as evident from Fig. 5.4. Therefore, the DIFF can be said the best.

4.5.3 Phantom Experiment

We use a tissue-mimicking (TM) phantom of dimension $90 \times 90 \times 120$ mm^3 with a 3-times stiffer (compared to the surrounding) cylindrical inclusion of 2cm diameter (CIRS, Inc. Norfolk, VA) to perform the elastography experiment. In the experiment, an ATL (Bothell, WA) Ultramark 9 scanner with a 7.5MHz linear array transducer was used to acquire RF echo-signals from this CIRS phantom. The RF-echo sampling frequency was 20MHz and quantized at 14 bits/sample. Before processing the RF data, it was corrected for time-gain-control (TGC).

Figs. 4.8(a-j) exhibit the strain images generated by the SBSE, RFC, W-RFENV,

DIFF and UPWD with the basic method W-RFENV for two different strains, respectively. The strain image generated by the DIFF method (Fig. 4.8(g)) performs the best amongst all the methods for 3% strain while other methods are fairly good except that the UPWD method smooths the strain image (Fig. 4.8(i)) in such a level that the lesion visibility is significantly reduced. At 5% strain, the SBSE method produces very noisy strain map but the strain map generated by the RFC method is less noisy in the background. Lesion area of the strain image generated by the W-RFENV method is less noisy than that of the RFC method for 5% strain. The DIFF method produces much smoother strain map and therefore, the lesion and the background are distinguishable in the presence of noise at 5% applied strain. The UPWD method smoothes the strain map without preserving the lesion edge (Fig. 4.8(j)).

Methods	SNRe		CNRe	
	Strain (3%)	Strain (5%)	Strain (3%)	Strain (5%)
SBSE	11.7263	2.3572	12.7334	0.0153
RFC	11.0563	3.3183	39.5125	0.0918
W-RFENV	11.4713	4.5315	55.1831	1.8351
DIFF	13.0081	5.8701	75.8201	2.8563
UPWD	7.2315	2.3180	24.7815	0.7013
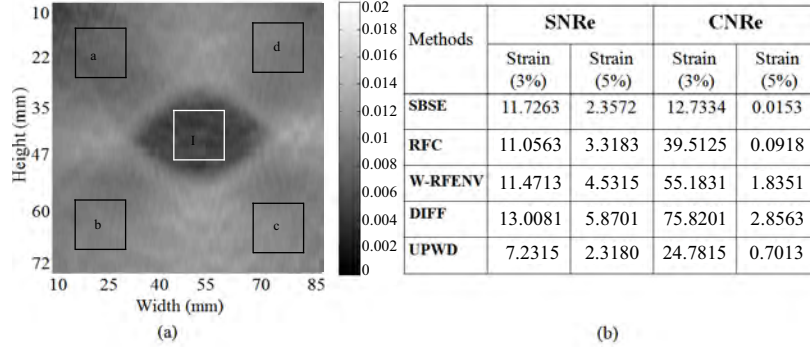
Figure 4.9: (a) Strain image of the CIRS experimental phantom showing the Lesion window-I and four background windows-a, b, c, d for the SNRe and CNRe calculation. (b) Table showing the SNRe and CNRe values for different methods at two different strains.

To evaluate the strain image quality of the CIRS phantom at two different applied strains, the SNRe and CNRe are presented in a table for the SBSE, RFC, W-RFENV, DIFF and UPWD with the basic method W-RFENV (Fig. 4.9(b)). Regarding SNRe, it is seen from the table that the DIFF shows the best performance among all the methods for 3% strain. At 5% strain, the W-RFENV shows better performance than the RFC, SBSE and UPWD methods as expected while the DIFF generated strain image exhibits highest SNRe value. Regarding CNRe, we see from the table that

66

the RFC shows better performance than the SBSE and UPWD methods, and DIFF shows the best performance for 3% strain. At 5% strain, W-RFENV shows better performance as expected than the RFC, SBSE and UPWD methods and the CNRe value of the DIFF generated strain image is found to be the maximum.

4.5.4 *In Vivo* Breast Experiment

We chose *in vivo* breast data for this work from an existing database of 33 cases (Patients' age: 20-75 years). These data were acquired with free-hand compression; benign and malignant cases were confirmed by histopathological reports. A Sonix-500RP (Ultrasonix Medical Corporation, Richmond BC, Canada) scanner operating at 10MHz (nominal) was used to acquire these data at the University of Vermont, USA. Institutional review board (IRB) approved this study and consent was obtained from patients. Out of thirty-three cases, two cases are selected in this work, one of which is a high strain frame (applied strain is approximately 2.5%, patient age is 63 years and, having adenocarcinoma) and another one is a low strain frame (applied strain is approximately 0.7%, patient age is 38 years and, having fibroadenoma).

In Figs. 5.7(b-f), strain images are produced by the SBSE, RFC, W-RFENV, DIFF and UPWD with the basic method W-RFENV, respectively for patient-I and, in Figs. 5.7(h-l), strain images are produced by the SBSE, RFC, W-RFENV, DIFF and UPWD with the basic method W-RFENV, respectively for patient-II. We have also calculated the MSSIM of each of the images by choosing two strain images (Fig. 4.11(a), (c)) generated by [67] as references for patient-I and patient-II, respectively. For patient-I, we can see from Fig. 5.7 (b-f) that except the SBSE and UPWD, all other methods show good performance in extracting the cancerous lesion from the backscattered ultrasound RF signals. For patient-II, only the SBSE method performs poorly among all other methods (Fig. 5.7 (h)). The DIFF method shows the smoother background compared to other approaches. In Figs. 5.7 (c-d), strain images generated by the RFC and W-RFENV techniques are seem similar in open eyes. But from the MSSIM table in Fig. 4.11(b), (d), it is seen that the W-RFENV shows better performance than the RFC. The DIFF shows the best performance in terms of MSSIM
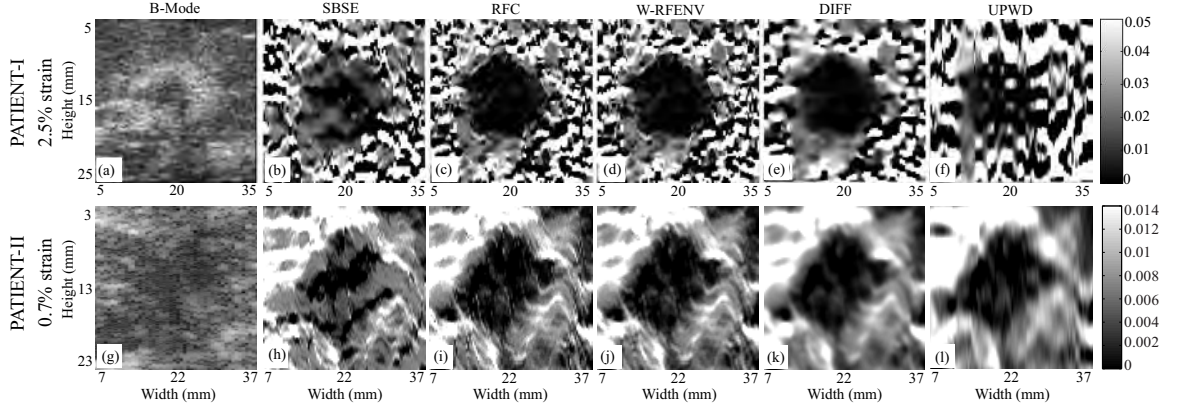
Figure 4.10: Strain images generated by different methods using *in vivo* breast ultrasound data. (a) and (g) represent B-mode images of two patients. Results (b) and (h) are produced by the SBSE method, (c) and (i) are produced by the RFC method ($\nu_v = 0.5$), (d) and (j) are produced by the W-RFENV method ($\nu_v = 0.5$), (e) and (k) are the diffusion filtered (DIFF) images of (d) and (j), respectively and, (f) and (l) are produced by the UPWD method.

(Fig. 4.11 (b), (d)). However, the UPWD shows very poor performance in generating the strain image (Figs. 5.7 (f) and 4.11(b)) for patient-I while satisfactory for patient-II (Figs. 5.7 (l) and 4.11(d)). Therefore, we can say that the UPWD method performs better in the low strain.

4.6 Conclusions

In this chapter, we have discussed a noise-robust displacement and strain estimation algorithm in the time domain. We have shown that the combined RF and envelope NCC can produce better strain images than the RF or the envelope NCC alone. We have also introduced the diffusion filtering to denoise the strain map. Compared to other denoising filters, diffusion filter has the ability to preserve edges and therefore, lesion edges can be preserved while denoising. The effect of considering the lateral shift in the selection of 1-D RF pre- and post-compression segments has also been shown in our method. Unlike the conventional gradient based strain estimators, our proposed

method can image the hard inclusions accurately. It has been shown by the simulation phantom, experimental phantom as well as by the *in vivo* breast data results that the proposed method is robust for a wide range of strain values than the other techniques used for comparison in this chapter. The quantitative performance indices also indicate that the proposed method can generate high quality strain images at high strain than that of the techniques compared in this literature.

Methods	MSSIM (%)
SBSE	1.63
RFC	1.75
W-RFENV	1.81
DIFF	2.83
UPWD	0.47

Patient Specification: 63/Adenocar

(b)

Methods	MSSIM (%)
SBSE	11.02
RFC	19.16
W-RFENV	21.52
DIFF	29.99
UPWD	26.94

Patient Specification: 38/Fibroad

(d)
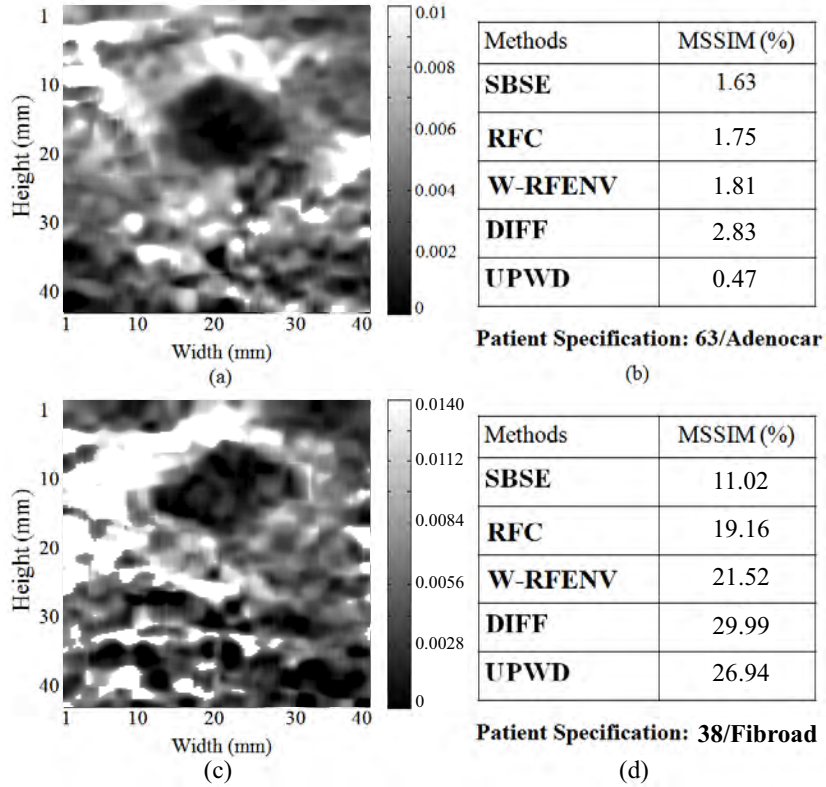
Figure 4.11: (a) Strain image of the *in vivo* breast data, generated by [67] for patient-I (a) at approximately 0.5% applied strain is chosen as references to calculate the MSSIM, (b) Table showing the MSSIM values for the different methods at 2.5% approximate applied strain. (c) Reference strain image generated by [67] for patient-II at approximately 0.5% applied strain, (d) Table showing the MSSIM values for the different methods at 0.7% approximate applied strain.

Chapter 5

Lesion Edge Preserved Direct Average Strain Estimation

5.1   Introduction

Elastography is an emerging medical imaging modality for detecting the abnormal changes in soft tissue via the assessment of tissue stiffness usually in terms of strain. In quasi-static elastography, various strain estimation methods have been developed for the detection and classification of lesions and/or tissue pathology change. Some of them are gradient-based techniques [1], [41], [44]–[47] where the strain is typically computed as the spatial gradient of local tissue displacements, and some are direct-strain-estimation techniques [36], [49] where the strain is directly estimated from the pre- and post-compression RF echo waveforms or spectra.

The gradient-based strain estimators face challenges in maintaining displacement continuity due to pre- and post-compression echo decorrelation, and different other noise artifacts [36], [45]. The gradient operation over the displacement map further amplifies these high frequency noise while estimating strain [47], [49]. To obtain a noise reduced strain map, a smoothing technique based on least-squares-linear-regression [52] or least-squared-error-based smoothing-spline [47] can be applied on the displacement matrix before the gradient operation. In addition, some of the recent methods designed

to ensure displacement continuity (and thus strain continuity) use estimates from the previous window in estimating the interrogative window displacement [39]–[41], [53]. In all these techniques, strain continuity is achieved only at the cost of lesion edge blurring along with the smoothing of the natural stiffness variation inside the lesion.

Noise in the strain map resulting from the derivative operation in the gradient-based methods can be avoided by using direct-strain-estimation methods that exist both in the time [36], [70] and frequency domain [49], [67]. Though these methods show better SNRe performance than the gradient-based techniques, they also face challenges to ensure strain continuity among neighborhood due to echo decorrelation. To ensure strain continuity, in [67] and [70], a cost function is defined for an interrogative point on the strain map from its exponentially weighted neighboring window pre- and post-compression RF spectral sum-of-square-differences (SSD) or echo cross-correlation peaks, respectively, in both the axial and lateral directions. However, though lesion edge preservation while ensuring the strain continuity is of great importance, none of these techniques are intelligent enough to detect and preserve the lesion edge as well as its natural stiffness variation inside.

In this paper, we propose a lesion edge preserved direct average strain estimation (LEP-DASE) method for elastography. We modify the direct average strain estimation (DASE) technique proposed in [70] by introducing a built-in edge preservation criterion into the average strain estimating cost function. A modified scheme based on [71] is proposed here for lesion edge detection with the use of a local 2-D matrix containing the cross-correlation peaks of the interrogated and neighborhood windows. According to this extracted edge information, only the cross-correlation peaks corresponding to the tissue points having similar stiffness to that of the interrogated tissue point are weighted to form the cost function. Consequently, the lesion edges are left unaffected while ensuring strain continuity among the neighborhood via the cost function maximization. We also use the Poisson's ratio to compensate for the lateral shift of RF data due to axial stress on the tissue surface. The performance of this algorithm is evaluated using a FEM phantom, experimental phantom as well as *in vivo* patient data, and compared with other recently reported regularized strain estimation algorithms.

5.2 Brief Review of the Direct Average Strain Estimation

The simplified 1-D model of the backscattered ultrasound RF signals before and after compression are given by [36]:

$$r_1(t) = s_1(t) + v_1(t) = s(t) * p(t) + v_1(t), \qquad (5.1)$$

$$r_2(t) = s_2(t) + v_2(t) = s\left(\frac{t}{a} - t_0\right) * p(t) + v_2(t), \qquad (5.2)$$

where $s(t)$ denotes the 1-D scattering function of the elastic target, $p(t)$ denotes the point-spread-function (PSF), a denotes the compression factor due to axial deformation of the target medium, t_0 denotes the time delay, $v_1(t)$ and $v_2(t)$ denote the uncorrelated random noise profiles, $r_1(t)$ and $r_2(t)$ denote the pre- and post-compression rf echo signals, respectively, and * indicates the convolution operation. The strain s is related to the compression factor $1/a$ as [28], $s = 1 - a$ where $a \leq 1$ and $s << 1$.

[70] proposed a method for direct average strain estimation (DASE) using the weighted nearest neighbor method in order to compensate for the signal de-correlation due to non-axial motion of tissue scatterers and thereby to introduce a built-in smoothing feature in the strain estimation algorithm. Calculated strain from a pair of windowed RF segments for a particular tissue point is assumed to be similar to the strains in the neighboring tissues due to their physical proximity. This assumption, however, works well unless there is a sudden change in the tissue stiffness.

Let $F_1(i,j)$ and $F_2(i,j)$ are the pre- and post-compression ultrasound RF echo frames, respectively. Here, i is the axial depth index and j is the RF A-line index. An effective strain at a point (i_s, j_s) on the strain map can be estimated from a corresponding pair of 1-D windowed RF segments $r_1^{(i_s,j_s)}$ and $r_2^{(i_s,j_s)}$ selected from the pre- and post-compression ultrasound image frames as [70]

$$r_1^{(i_s,j_s)}(i) = F_1((i_s - 1)L_v + i, j), \quad \text{for } 1 \leq i \leq L_i \text{ and } j = j_s \qquad (5.3)$$

$$r_2^{(i_s,j_s)}(i) = F_2(round((i_s - 1)(1 - s_{avg})L_v) + i, j), \qquad (5.4)$$

$$\text{for } 1 \leq i \leq L_i \text{ and } j = j_s + (j_s - \frac{N_c}{2})s_{avg}\nu$$

where ν represents the Poisson's ratio, N_c represents the number of scan lines in the RF frame, L_v is the axial separation between two successive RF windows in samples and L_i represents the length of the 1-D RF window. The assumption that the approximate applied strain s_{avg} is known a priori is a drawback of the DASE method [70]. In this paper, instead of assuming that s_{avg} is a known constant, we adaptively define it from the estimated previous window strain $S_o(i_s - 1, j_s)$ as [72]

$$
s_{avg} = \begin{cases} 0; & i_s = 1 \\ S_o(i_s - 1, j_s); & \text{otherwise.} \end{cases} \tag{5.5}
$$

After stretching the post-compression echo segment $r_2^{(i_s,j_s)}$ by a factor α (≤ 1), the normalized cross-correlation (NCC) coefficient $\rho_\alpha(k)$ between $r_1^{(i_s,j_s)}$ and $r_\alpha^{(i_s,j_s)}$ is estimated as [61],

$$
\rho_\alpha^{(i_s,j_s)}(k) = \frac{\sum_{i=1}^{L_i} r_1^{(i_s,j_s)}(i) \cdot r_\alpha^{(i_s,j_s)}(i+k)}{\sqrt{\sum_{i=1}^{L_i} \{r_1^{(i_s,j_s)}(i)\}^2 \sum_{i=1}^{L_i} \{r_\alpha^{(i_s,j_s)}(i)\}^2}}. \tag{5.6}
$$

The peaks of $\rho_\alpha^{(i_s,j_s)}(k)$ are calculated by using the cosine interpolation for different values of α:

$$
M_\alpha(i_s, j_s) = \rho_\alpha^{(i_s,j_s)} \left(\arg \max_k \{\rho_\alpha^{(i_s,j_s)}(k)\} \right), \tag{5.7}
$$

where M_α is a matrix that contains the NCC peaks. For average strain estimation, a cost function is defined as

$$
J_\alpha^{(i_s,j_s)} = \sum_{i_0=i_s-L_a}^{i_s+L_a} \sum_{j_0=j_s-L_l}^{j_s+L_l} w^{(i_s,j_s)}(i_0, j_0) M_\alpha(i_0, j_0) \tag{5.8}
$$

where

$$
w^{(i_s,j_s)}(i_0, j_0) = e^{-|\lambda_a(i_0-i_s)|-|\lambda_l(j_0-j_s)|}, \tag{5.9}
$$

$$
\text{for} \quad i_s - L_a \leq i_0 \leq i_s + L_a; j_s - L_l \leq j_0 \leq j_s + L_l
$$

Here, λ_a and λ_l are the weighting factors, and L_a and L_l are the nearest neighbor (NN) factors in the axial and lateral directions, respectively. The weight function $w^{(i_s,j_s)}$ is

defined in such a way so that the RF windows of increasing distance from the inter-rogated window are least "emphasized". However, there is no constraint incorporated for the lesion edge preservation in the cost function (Eqn. (5.8)). Thus, instead of a sharp change in the strain profile, a slowly decaying nature of the estimated strain is seen at the lesion edge regions.

5.3 Lesion Edge Preserved Direct Average Strain Estimation (LEP-DASE)

In detecting an edge along a line of intensity pixels, we may face two types of pixels: the noise pixel and the edge pixel (Fig. 5.1). A noise pixel is one which has much higher or lower intensity than the adjacent pixels having similar intensities. The edge pixel is one which is either on an inclining slope or on a declining. From these topology, we can define the following necessary parameters [71]:
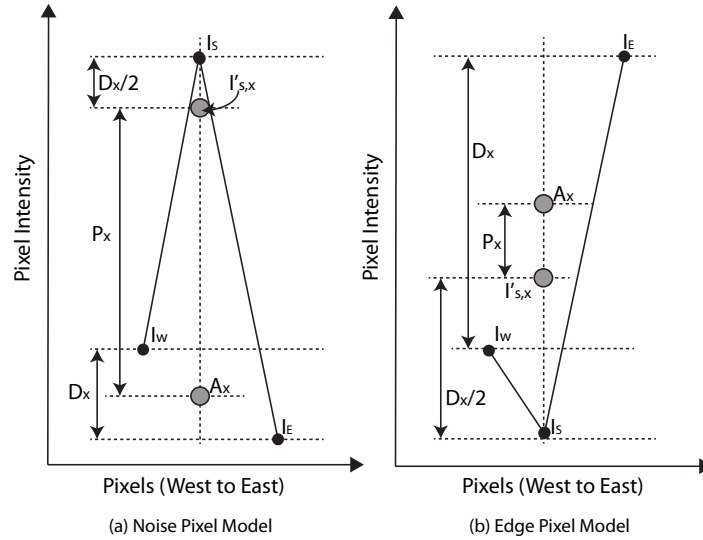
Figure 5.1: Representation of (a) a typical noise pixel and (b) a typical edge pixel.

$$D_x = \begin{cases} \mid I_E - I_W \mid -\delta; \ \ if \mid I_E - I_W \mid > \delta \\ 0; \qquad\qquad\quad \text{otherwise,} \end{cases} \tag{5.10}$$

74

$$A_X = \frac{1}{2}(I_E + I_W),\tag{5.11}$$

$$I'_{S,x} = \begin{cases} I_S - \frac{1}{2}D_X; & if \ I_S > A_X \\ I_S + \frac{1}{2}D_X; & if \ I_S \leq A_X, \end{cases}\tag{5.12}$$

$$P_X = I'_{S,x} - A_X,\tag{5.13}$$

where I_E and I_W represent the image intensity values at the east and west neighboring pixels, A_X represents the average of the neighboring pixels in the $x-$direction (East-West), $I'_{S,x}$ is an intermediate intensity value of the interrogated pixel, and P_X is the difference between $I'_{S,x}$ and A_X. We define an auxiliary parameter $\delta \in [0, \sigma]$ to prevent small noise regions to be identified as edges, where σ is the standard deviation of the image noise. In the proposed method, median absolute deviation (MAD) is used for automatic computation of δ [73]. From Fig. 5.1, we see that P_X is greater than D_X for the noise-like pixel, and P_X is less than D_X for the edge-like pixel. For the $y-$direction (North-South), similar parameters D_Y, A_Y, $I'_{S,y}$, and P_Y can be estimated. These estimated parameters can be used for the edge detection in a whole intensity image. As shown in Fig. 5.2, in the proposed method, we modify the edge detection scheme [71] originally designed for a whole intensity image. In Fig. 5.2(a), we show a portion from the FEM simulation phantom having two different stiffness. The NCC peaks for the interrogated (i_s, j_s) and neighborhood tissue points for different stretching factor α are shown in Fig. 5.2(b). It is expected that the window NCC peaks of different tissue points having similar stiffness will be maximized at the same stretching factor. Therefore, to check for the tissue points with identical stiffness to that of the interrogated tissue point, we need to find the reference stretching factor α_r at which the interrogated window NCC peak becomes maximum with respect to the stretching factor α and it can be estimated as

$$\alpha_r = \arg\max_{\alpha}\{\rho_{\alpha}^{(i_s,j_s)}\}.\tag{5.14}$$

Now, $M_{\alpha_r}(i_r, j_r)$ plane for $i_s - L_a \leq i_r \leq i_s + L_a$ and $j_s - L_l \leq j_r \leq j_s + L_l$ is considered as the reference image, and assumed equivalent to an intensity image for edge detection. A

(a) A tissue scenario with two different stiffness creating an edge

(b) NCC peaks for different stretching factor, α

(c) Reference plane, $M_{\alpha r}(i_r, j_r)$
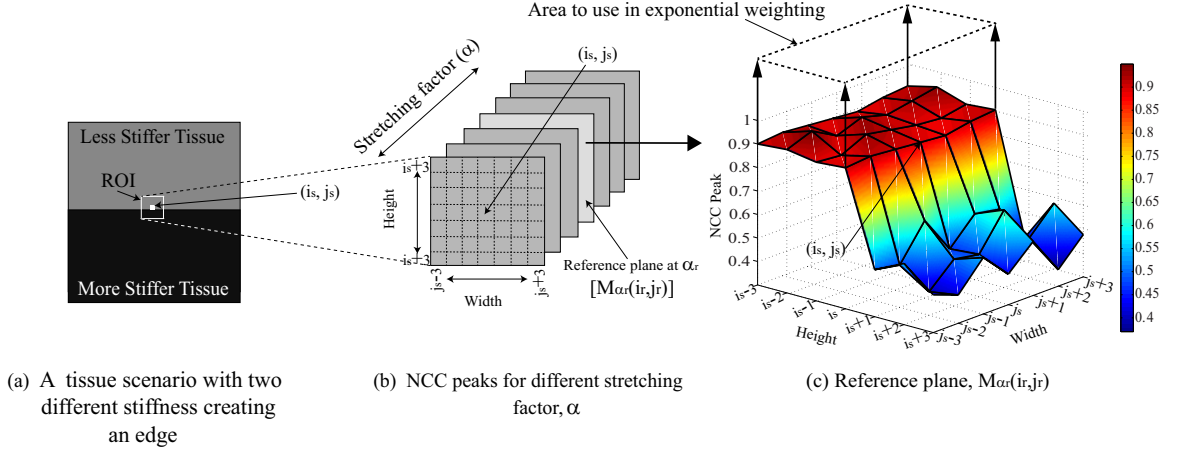
Figure 5.2: Schematic and mesh diagrams illustrating the edge detection procedure, and tissue points selection for using in the exponential weighting. (a) A portion (as shown in Fig. 5.4(b) with dashed box "T") of the FEM simulation phantom with two different stiff areas creating an edge, (b) NCC peaks of the interrogated and neighborhood windows for different stretching factor, and (c) 2-D plot of the reference plane $M_{\alpha_r}(i_r, j_r)$.

mesh plot showing the reference plane $M_{\alpha_r}(i_r, j_r)$ is depicted in Fig. 5.2(c). The region-of-interest (ROI) ($i_s - L_a \leq i_r \leq i_s + L_a$ and $j_s - L_l \leq j_r \leq j_s + L_l$) that includes the interrogated and neighborhood tissue points consists of two homogeneous areas of highly different stiffness. Therefore, the compression factor in the post-compression signal windows inside this ROI will be much less in the stiffer area than the softer one. Note that the interrogated tissue point is on the border of the less stiff area (see Fig. 5.2(a)). In this case, since the NCC function between the interrogated pre- and post-compression signal windows will be maximum for the stretching factor α_r (Eqn. (5.14)), the neighborhood NCC functions estimated from the corresponding pre- and post-compression windowed signals in the less stiff area of the ROI are also expected to be close to the maximum for the same stretching factor α_r due to their stiffness similarity to the interrogated one. However, using the same stretching factor α_r for the post-compression windowed signals in the stiffer area of the ROI will result in much lower NCC peaks as depicted in Fig. 5.2(c). An informative NCC peak plane (i.e.,

76

the reference plane $M_{\alpha_r}(i_r, j_r)$) can, therefore, be formed as shown in Fig. 5.2(c) that has a very sharp edge at the interface of two dissimilar stiffness areas, where the edge detection scheme can be applied. Also note that instead of detecting edge in the entire $M_{\alpha_r}(i_r, j_r)$ plane, only the interrogated pixel (i.e., the NCC peak) is tested whether it is on an edge or not. The idea behind the edge detection on M_{α_r} is that if the interrogated pixel is on a lesion edge, P_X would be less than D_X and/or P_Y would be less than D_Y in $x-$ and $y-$directions, respectively. Note that we calculate σ for the whole M_{α_r} plane.

Now the exponential weight defined in Eqn. (5.9) needs to be modified to preserve the edge. The spreading of the exponential weight is to be controlled so that it does not include the smaller NCC values and thus, avoid interference of NCC values of different stiffer region into the cost function (Fig. 5.2(c)). However, from Eqns. (5.10)-(5.13), we can only know whether the interrogated NCC peak is on an edge or not, but no indication of the position (i.e., East, West, North and South) of different stiffer region with respect to it. Let the interrogated, East, West, North and South pixels are defined as $I = M_{\alpha_r}(i_s, j_s)$, $E = M_{\alpha_r}(i_s, j_s + 1)$, $W = M_{\alpha_r}(i_s, j_s - 1)$, $N = M_{\alpha_r}(i_s - 1, j_s)$ and $S = M_{\alpha_r}(i_s + 1, j_s)$, respectively. Then, the modified ranges from East (R_E) to West (R_W) and North (R_N) to South (R_S) of the weight function defined in Eqn. (5.9) can be chosen as

$$R_E = \begin{cases} j_s; & \text{if} \quad |I - E| > |I - W| \\ j_s + L_l; & \text{otherwise,} \end{cases} \tag{5.15}$$

$$R_W = \begin{cases} j_s; & \text{if} \quad |I - E| < |I - W| \\ j_s - L_l; & \text{otherwise,} \end{cases} \tag{5.16}$$

$$R_N = \begin{cases} i_s; & \text{if} \quad |I - N| > |I - S| \\ i_s - L_a; & \text{otherwise,} \end{cases} \tag{5.17}$$

$$R_S = \begin{cases} i_s; & \text{if} \quad |I - N| < |I - S| \\ i_s + L_a; & \text{otherwise.} \end{cases} \tag{5.18}$$

Now, by using these modified ranges for all the stretching factors, the modified cost function is defined for a particular strain point (i_s, j_s) on the strain map as

$$\tilde{J}_\alpha^{(i_s,j_s)} = \sum_{i_0=R_N}^{R_S} \sum_{j_0=R_W}^{R_E} w^{(i_s,j_s)}(i_0,j_0) M_\alpha(i_0,j_0). \qquad (5.19)$$

Then, the desired value of α is calculated as

$$\alpha_o^{(i_s,j_s)} = \arg\max_\alpha \{\tilde{J}_\alpha^{(i_s,j_s)}\}. \qquad (5.20)$$

And, finally, the effective average strain at (i_s, j_s) is estimated as

$$S_o(i_s, j_s) = 1 - \alpha_o^{(i_s,j_s)}. \qquad (5.21)$$

5.4 Simulation and Experimental Results

We provide comparative results of our proposed method with the 2-D analytic minimization (AM2D) [53] and direct average strain estimation (DASE) [70] methods using the FEM phantom, CIRS experimental phantom and the *in vivo* patient data. In addition to the evaluation by visual inspection, we compare the performances of different methods in terms of the SNRe [64], CNRe [65] and EMSE. The AM2D is a real-time elastography technique based on analytic minimization of a regularized cost function that incorporates similarity of RF data intensity and displacement continuity. The strain field is computed from the displacement field using Kalman filtering.

5.4.1 FEM Simulation

A rectangular 40mm × 40mm FEM phantom was modeled using the analysis software ANSYS (ANSYS Inc., Canonsburg, PA) and ultrasound simulation was performed over the model using Field II [74]. In this simulation, the total number of nodes was 54574. Due to using a 2-D model, it did not model out-of-plane motion. This phantom had a homogeneous background with stiffness of 10kPa with a rectangular inclusion of dimension 10mm × 20mm (Fig. 5.3(a)). The stiffness of the inclusion was 80kPa. The phantom was compressed from the top using a larger-width planar compressor.

An ultrasonic transducer of *center frequency*, $f_0 = 5$MHz and *band-width* $= 50\%$ was used to scan the phantom from the top. The total number of scan lines was 128.
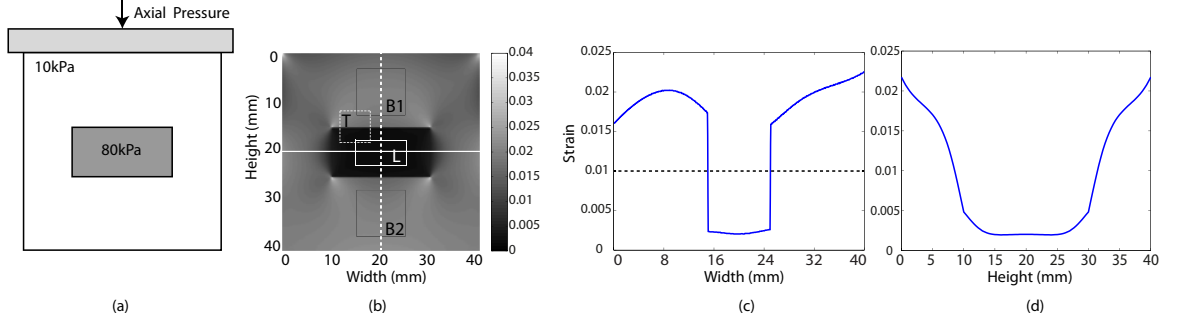
Figure 5.3: FEM simulation phantom. (a) Stiff inclusions in a homogeneous background of 10kPa, and (b) corresponding actual elastogram. The rectangular boxes "B1", "B2", and "L" are selected from the homogeneous regions to calculate the SNRe and CNRe of the strain images generated by the proposed and other techniques compared with. The region marked by the dashed rectangular box "T" is used to produce Fig. 5.2. (c) Strain profile of the vertical dashed line in (b), (d) strain profile of the horizontal solid line in (b).

For qualitative evaluation of the perceptual quality of the strain images generated by the AM2D, DASE and LEP-DASE methods, we present strain images of the FEM simulation phantom for three different applied strains (2%, 4% and 6%) in Fig. 5.4. For the DASE and LEP-DASE methods, we have used a data window (L_i) of 2.28mm and an inter-window shift (L_v) of 0.28mm. For all strains, all methods produce satisfactory strain images. However, strain images produced by the DASE and LEP-DASE methods are merely similar except the edge blurring performance. Due to no edge preserving constraint in the cost function-based average strain estimation of the DASE method, the inclusion edge is much blurred than that of the LEP-DASE method. This edge blurring effect can be well understood from the vertical 1-D strain profiles presented in Figs. 5.4(j)-(l). The profiles are selected so that the variation of stiffness in the inclusion is included (dashed vertical line in Fig. 5.3(b)). In Figs. 5.4(j)-(l), we see that the edges of the strain well produced by the DASE method are not enough steep compared to the actual ones resulting in a broadened transition width of the strain

79
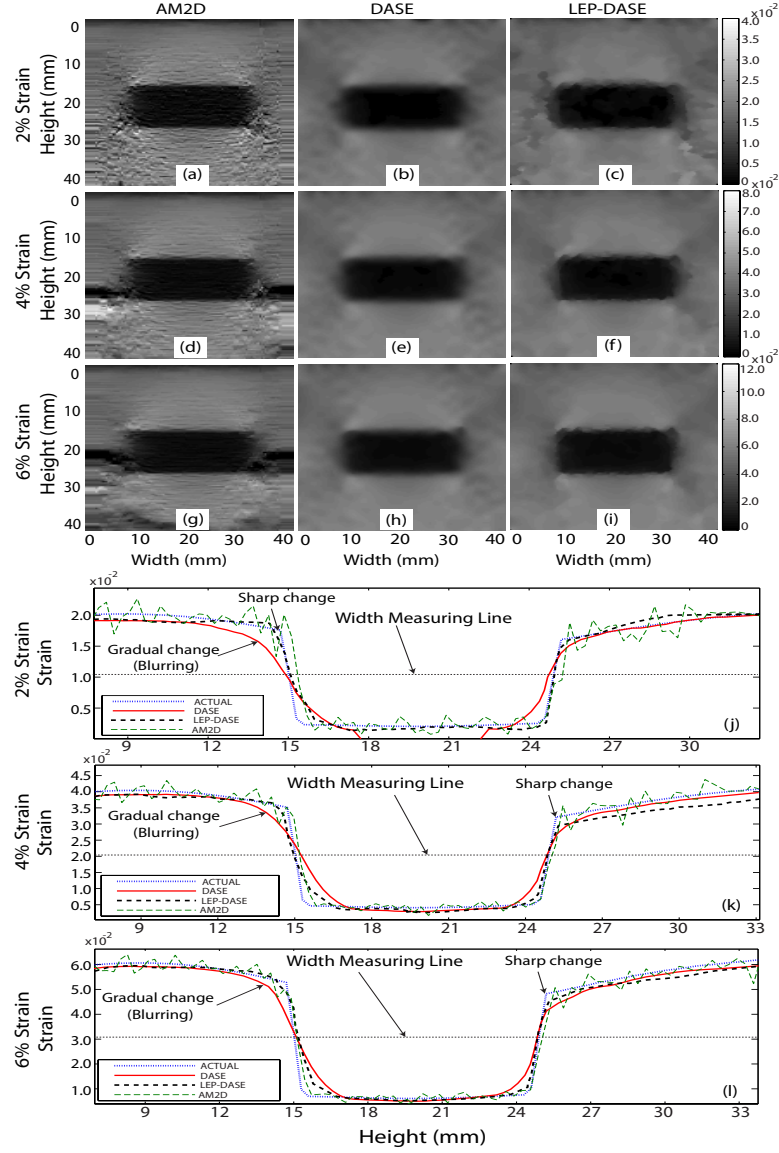
Figure 5.4: Strain images of the FEM simulation phantom generated by different methods. Results (a, d, g) are produced by the AM2D, (b, e, h) are produced by the DASE (L_a=4, L_l=4, λ_a=λ_l=0.25, ν=0.5), (c, f, i) are produced by the proposed LEP-DASE (L_a=4, L_l=4, λ_a=λ_l=0.25, ν=0.5), and (j, k, l) represent the strain profiles of different methods at 2%, 4% and 6% strains, respectively.

well due to blurring. On the other hand, we appropriately downsample the strain profile produced by the AM2D method to match the data length with that of the LEP-

DASE and DASE methods. We can see from Figs. 5.4(j)-(l) that the strain profiles estimated by the proposed LEP-DASE method is more closer to the actual ones. For quantitative evaluation of the edge preserving performance, we calculate the EMSE between the actual and the estimated strain profiles, and also the inclusion width. The EMSE is calculated as

$$EMSE = \frac{1}{P} \sum_{p=0}^{P-1} [U(p) - V(p)]^2, \tag{5.22}$$

where U and V are the actual and estimated strain profiles of length P, respectively. On the other hand, the measured width of the inclusion at the width measuring line in Fig. 5.3(c) is 9.82mm. We fit the width measuring line approximately at the mid-height of the strain well. The estimated values of EMSE and inclusion widths by different methods are shown in Table 5.1. Note that the presented EMSE values for all methods denote the minimum value obtained from the properly aligned actual and estimated strain profiles. It is evident that the estimated EMSE is the least for the proposed LEP-DASE method for all the three applied strain values. The EMSE performance of the AM2D method is the worst for all the cases. However, the estimated inclusion widths are fairly accurate for all the three methods.
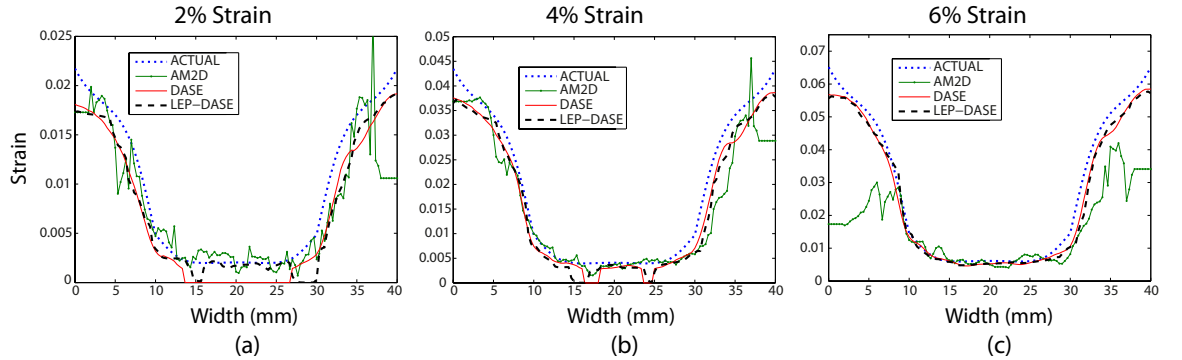
Figure 5.5: Illustration of lateral strain profiles produced by the proposed, DASE and AM2D methods at (a) 2%, (b) 4%, and (c) 6% applied strain, respectively

We also show the horizontal 1-D strain profiles for the FEM simulation phantom at three different applied strains in Fig. 5.5. These profiles are selected in a way that the

Table 5.1: EMSE and lesion width for the stiffer inclusion at 2%, 4% and 6% applied strains

Methods	2% Strain		4% Strain		6% Strain	
	EMSE $(\times 10^{-5})$	Width (mm)	EMSE $(\times 10^{-5})$	Width (mm)	EMSE $(\times 10^{-5})$	Width (mm)
AM2D	0.88	9.95	3.22	9.90	2.70	9.94
DASE	0.53	9.90	1.90	9.62	1.94	9.70
LEP-DASE	0.40	9.72	1.21	9.84	1.44	9.70

variation of stiffness in the inclusion is included (solid horizontal line in Fig. 5.3(b)). From Fig. 5.3(d), it can be seen that the actual strain profile does not show sharp edges at the two sides of the inclusion. The estimated strain profiles in Fig. 5.5 by the DASE and LEP-DASE methods for 2%, 4%, and 6% applied strain satisfactorily follow the actual strain profile. But the strain profiles produced by the AM2D method at 2% and 4% applied strain have noticeable variations though following the actual trend while at 6% strain, it is significantly distorted (see Figs. 5.5(a-c)).

From Fig. 5.4, it may appear that the proposed LEP-DASE method preserves the inclusion edge at the cost of smoothing performance. Therefore, for quantitative performance evaluation of the proposed and other two methods, two numerical performance metrics (i.e., SNRe and CNRe) are calculated at different applied strain (e.g., 2%, 4% and 6%) for the FEM simulation phantom. The performance metrics SNRe [64] is defined as

$$SNRe = \frac{\mu_s}{\sigma_s} \qquad (5.23)$$

where, μ_s and σ_s denote the statistical mean and standard deviation of the strain computed in a homogeneous area, respectively. Similarly, the performance metrics CNRe [65] is defined as

$$CNRe = \frac{2(\mu_l - \mu_b)^2}{\sigma_l^2 + \sigma_b^2} \qquad (5.24)$$

where, μ is the mean strain and σ is the standard deviation of the strain in a homoge-

Table 5.2: SNRe and CNRe performance of different methods at 2%, 4% and 6% applied strains

Methods	Strain 2%		Strain 4%		Strain 6%	
	SNRe (dB)	CNRe (dB)	SNRe (dB)	CNRe (dB)	SNRe (dB)	CNRe (dB)
AM2D	19.73	19.86	22.92	23.74	24.53	25.30
DASE	26.28	28.20	26.71	27.61	27.07	28.90
LEP-DASE	26.00	27.46	26.38	27.01	26.84	28.61

neous area. The sub-subscript l and b refer to the lesion and background, respectively. For estimating the SNRe and CNRe of the FEM simulation, the selected homogeneous background regions, B1 and B2, and the homogeneous lesion area, L are shown in Fig. 5.3(b) with rectangular boxes. The calculated SNRe and CNRe values are presented in Table 5.2. From this Table, we can see that the SNRe and CNRe values of the strain images produced by the LEP-DASE method is pretty close to those of the DASE method although the SNRe and CNRe performance of the DASE method is the best among other methods. Nevertheless, the visual quality of the strain images by the LEP-DASE method appears to be better because of its lesion edge preserving performance (see Figs. 5.4, 5.6 and 5.7)). The AM2D method shows the worst performance among the techniques compared with.

5.4.2 Experimental Phantom Results

We have used a tissue-mimicking (TM) experimental phantom of dimension 40mm $\times$ 40mm (CIRS Inc., Norfolk, VA) to evaluate the performances of the proposed and other two techniques in this paper. The phantom has a homogeneous background of stiffness 33kPa with an inclusion of stiffness 56kPa inside. It was axially compressed 0.2 inch using a linear compressor which resulted in an average strain of 6%. An Antares Siemens system (Issaquah, WA) with a 7.27MHz linear array transducer was used to collect RF data at a sampling rate of 40MHz.
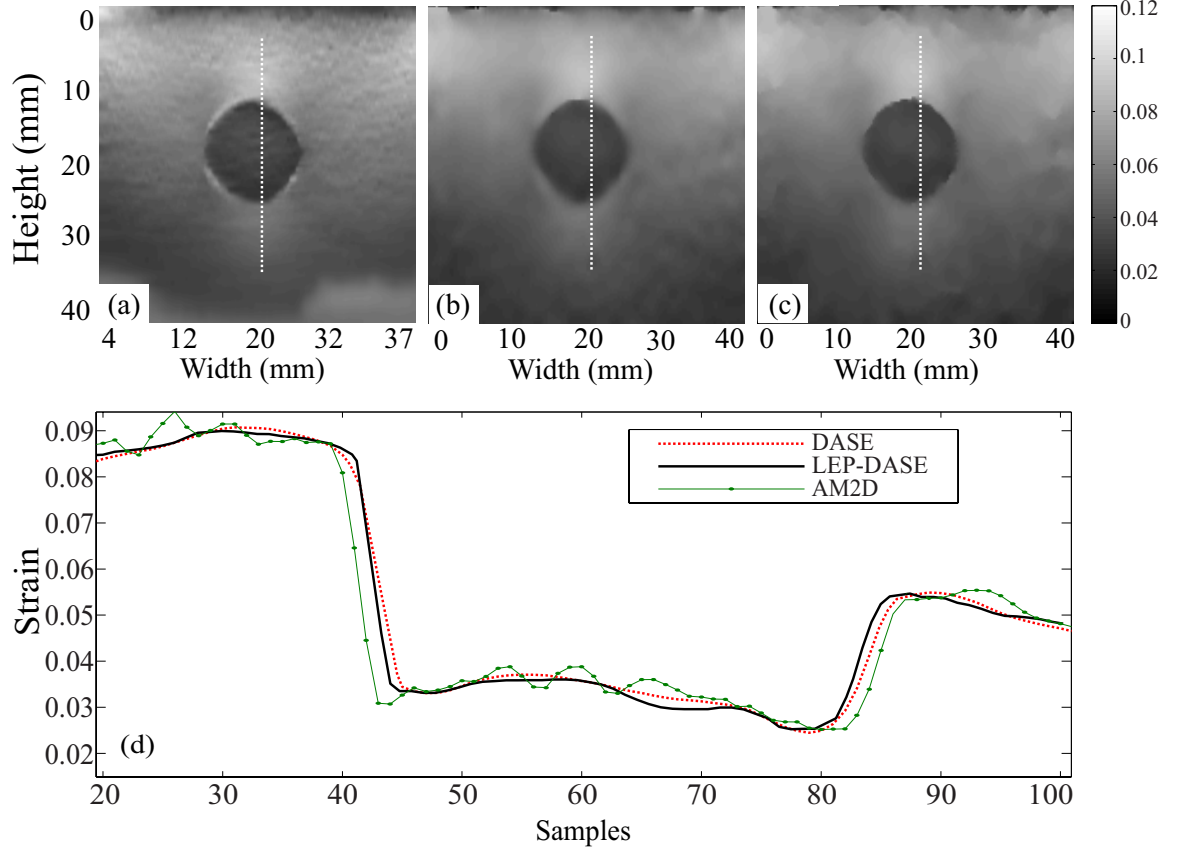
Figure 5.6: Strain images of the experimental phantom generated by different methods at 6% applied strain: (a) AM2D, (b) DASE (L_a=4, L_l=4, $\lambda_a=\lambda_l$=0.25, ν=0.2), (c) proposed LEP-DASE (L_a=4, L_l=4, $\lambda_a=\lambda_l$=0.25, ν=0.2). (d) The strain profiles of different methods (white-dashed lines in (a)-(c)).

We show the strain images of the experimental phantom generated by the AM2D, DASE and LEP-DASE methods in Fig. 5.6. From this figure, we see that the strain images produced by the DASE and LEP-DASE methods are smoother than that of the AM2D method. However, the lesion edge is seen blurred for the DASE method (Fig. 5.6(b)). But in Fig. 5.6(c), we see that the lesion edge is well preserved by the LEP-DASE method. We also show the strain profiles for the white-dashed lines in Figs. 5.6(a), (b), (c) in Fig. 5.6(d). We appropriately downsample the strain profile produced by the AM2D method to match the data length with that of the LEP-DASE

and DASE methods. From these strain profile plots, we see that the lesion edge is steeper for the LEP-DASE method than that of the DASE method while the profile produced by the AM2D method is not as smooth as those of the LEP-DASE and DASE methods.

5.4.3 Comparison Using *In Vivo* Breast Data

We have chosen three sets of *in vivo* breast data from an existing database of 194 cases (age: 14-63 years). These data were acquired by using a SonixTOUCH Research (Ultrasonix Medical Corporation, Richmond BC, Canada) scanner integrated with a L14-5/38 probe operating at 10MHz (nominal) at Bangladesh University of Engineering and Technology (BUET) Medical Center, Dhaka, Bangladesh. An institutional review board (IRB) approved the study. In addition, prior consent was taken from every patient for further use of these data in research. Note that data were acquired with free-hand compression of the ultrasound probe. Two of them represent benign breast tumors (Fibroadenoma) and the other one represents a malignant case. The B-mode images of patient-I (Age: 38/Tumor type: Fibroadenoma), patient-II (Age: 15/Tumor type: Fibroadenoma) and patient-III (Age: 25/Tumor type: Adenocarcinoma) are shown in Figs. 5.7(a), (e), (i), respectively.

We observe from Fig. 5.7 that the AM2D method smooths the lesions to such a degree for patient-I and II (Figs. 5.7(b), (f)) that the stiffness variation inside the lesions is totally lost. In case of patient-III, this method cannot perfectly extract the lesion from the background. In addition, because of the absence of any edge preserving constraint in the algorithm, the AM2D method smooths the lesion edges as well, which is clearly depicted in Fig. 5.7(b). The DASE method though shows promise to be a better smoother, for the similar reason as stated above, it also smooths the lesion edges (Figs. 5.7(c), (g), (k)). On the other hand, the proposed LEP-DASE method smooths the strain images with the lesion edges preserved. In Figs. 5.7(d), (h), (l), we have traced the lesion edges with small arrows around them. As can be seen, the edges are much sharper and the smoothing of the stiffness variation inside the lesions is significantly less prominent than that of the original DASE method.

85
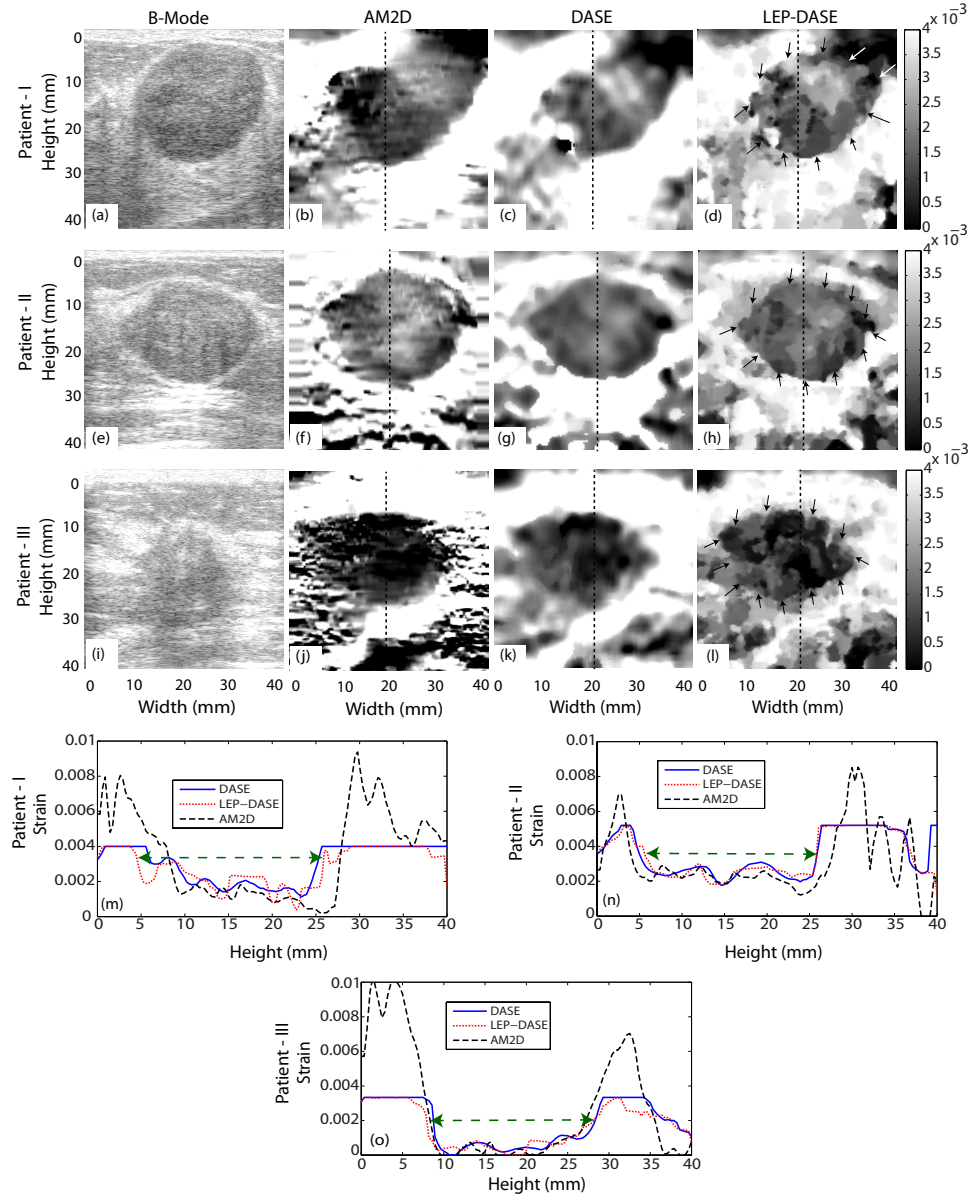
Figure 5.7: B-mode (a, e and i) and strain images of the *in vivo* breast data generated by different methods. Result (b, f and j) are produced by the AM2D, (c, g and k) are produced by the DASE (L_a=4, L_l=4, λ_a=λ_l=0.25, ν=0.5), (d, h and l) are produced by the proposed LEP-DASE (L_a=4, L_l=4, λ_a=λ_l=0.25, ν=0.5), and (m, n and o) represent the strain profiles of different methods (black-dashed lines in b-d, f-h and j-l for patient-I, II and III, respectively).

For better understanding of the lesion edge preservation scenario, we plot the 1-D strain profiles for patient-I, II and III in Figs. 5.7(m)-(o), respectively. For each case, we see that the proposed LEP-DASE method produces a steeper edge on both sides of the lesions so that the lesion widths are clearly visible (indicated by arrows in Figs. 5.7(m)-(o)). Whereas the DASE method smooths the edge and the lesion width cannot be comfortably detected. On the other hand, the strain profile produced by the AM2D method has high degree of smoothing at the lesion edge for the patient-I (Fig. 5.7(m)), has much variation in the strain values for the patient-II (Fig. 5.7(n)), and is satisfactory for detecting edges for the patient-III (Fig. 5.7(o)). We can also observe from the strain profiles produced by the proposed LEP-DASE method for the patient-I and II (Fibroadenoma) that the estimated strain inside the lesions is about 2% on average. Whereas for the patient-III (Adenocarcinoma), the estimated strain by the proposed LEP-DASE method inside the lesion is almost close to zero. Thus, the typical assumption that malignant lesions are stiffer than benign ones hold true in this case.

5.5 Discussion

The performance of the proposed LEP-DASE method has been demonstrated both quantitatively and qualitatively in the results section. The distinct feature of the proposed LEP-DASE method that differentiate it from the other strain continuity ensuring methods, such as [53], [67], [70] is the detection of inclusion/lesion edges prior to strain estimation and formulate the cost function accordingly in a way that the inclusion/lesion edges are well preserved while ensuring strain continuity among neighborhood tissues. However, the computational complexity is slightly increased due to the incorporation of the edge detection algorithm that requires some extra processing for each interrogated signal windows. The computation time (CPU: Core i5, 2.3 GHz, RAM: 2 GB, software: MATLAB, The MathWorks, Natick, MA) of our implementation of the AM2D, DASE, and LEP-DASE methods for generating the strain images (*in vivo* breast experiment: patient-I) are 0.35, 79.36, and 94.60 *s*, respectively. The

results show that the AM2D method is very fast compared to others. However, the AM method uses mex files but the others do not. By using mex files, the computational time of the DASE and proposed method can also be reduced.

To compensate for the lateral shift of the RF data without using a 2-D search region, the Poisson's ratio, ν has been used in Eqn. (5.4) to save some extra computation [67]. It has been varied from 0 to 1 at an interval of 0.25 in order to choose an appropriate value and the optimum image quality for all the strain images shown has been observed for $\nu = 0.5$. This value agrees with that reported in [72]. In addition, it is assumed that $p(\alpha t) \cong p(t)$ while similarity between $r_1^{(i_s, j_s)}$ and $r_\alpha^{(i_s, j_s)}$ is computed in Eqn. (5.6). However, this assumption is reasonably accurate at low strain [36], [50]. Further study on the estimation of PSF $(p(t))$ is necessary to compensate for this effect.

As the ultrasound RF signal gets attenuated while propagating along depth, the signal-to-noise ratio decreases. However, this attenuation effect is less observed in the correlation-based techniques (i.e., DASE and proposed LEP-DASE) as these methods seek for the RF waveform similarity between the the pre- and post-compression signal windows. On the contrary, as the AM2D method is based on pixel intensity similarity between the pre- and post-compression signals, it is highly sensitive to ultrasound attenuation effect. Moreover, the algorithm has been observed to be highly sensitive to setting of the several other parameters.

5.6   Conclusions

In this paper, we have presented a lesion edge preserving direct average strain estimation method for high quality quasi-static elasticity imaging. To prevent blurring of the lesion edge while ensuring strain continuity, an intelligent edge preservation criterion is incorporated in the exponential weighting process of the strain determining cost function. It has been shown by the simulation, experimental and *in vivo* patient results that the proposed method is more accurate and robust in edge preservation than the other recently reported strain estimation methods that have been designed to ensure strain continuity. The perceptual quality of the strain image obtained by

the proposed LEP-DASE method, in particular for the *in vivo* patient data, has improved significantly in the lesion area due to the reduction of the blurring effect. The proposed LEP-DASE method enhances the ultrasonic average strain imaging performance particularly by delineating the lesion edge more clearly as compared to other contemporary techniques. The lesion edge preserved strain imaging might be clinically significant for classifying tumors based on their shape and area ratio (elastographic to B-mode) and also for determining the spatial extent of tumors.

Chapter 6

Conclusions

6.1 Summary

In this thesis work, we have developed time domain techniques for direct and gradient-based average strain estimation using the exponentially weighted nearest neighbors. Unlike as in the conventional algorithms, the continuity of estimated strain is ensured without using any prior estimate of the displacement or strain. Rather, we have shown that the average displacement and strain can be estimated by maximizing our proposed weighted cost function derived from the information of the neighboring windowed RF echoes. The effect of considering the lateral shift in the selection of 1-D RF pre- and post-compression segments has been also demonstrated for DASE as well as GBASE methods. It has been shown by simulation and experimental results that the proposed DASE and GBASE methods are more robust for a wide range of strain values than the compared techniques. We have shown strain profiles for the FEM phantom and calculated the overall MSE, which depict the superiority of our proposed methods over the other reported techniques. We also have plotted the strain profiles for very small and larger *in vivo* breast lesions where lesion dimensions estimated by our proposed methods matched well with those of the histology. Furthermore, only the proposed GBASE method successfully depicted the tiny lesion with the correct dimensions. The values of the quantitative performance metrics for the FEM and experimental phan-

tom also indicate that the proposed methods generate higher quality and higher SNR strain images than the techniques compared with. For example, in FEM simulation it has been found that the proposed direct strain estimation method can improve up to approximately $2.49 \sim 8.71$ dB, $2.2 \sim 6.63$ dB, $1.5 \sim 5$ dB, and $1.59 \sim 2.45$ dB in the SNRe, CNRe, PSNR, and MSSIM compared to the traditional direct strain estimation method, respectively, and the proposed gradient-based algorithm demonstrates $2.99 \sim 16.26$ dB, $18.74 \sim 23.88$ dB, $3 \sim 9.5$ dB, and $0.6 \sim 5.36$ dB improvement in the SNRe, CNRe, PSNR and MSSIM, respectively, compared to a recently reported time-domain gradient-based technique. The range of improvement as noted above is for low to high applied strains. In addition, the comparative results using the *in vivo* breast data (including malignant or benign masses) also show that the lesion size is better defined by the proposed gradient based average strain estimation technique.

We also have developed an improved approach for robust strain estimation by combining the RF NCC and envelope NCC functions in a novel way. An applied strain-dependent piecewise-linear-weight is formulated for mixing the two functions. We have shown that the combined RF and envelope NCC can produce better strain images than the RF or the envelope NCC alone. We have also introduced the diffusion filtering to denoise the strain map. Compared to other denoising filters, diffusion filter has the ability to preserve edges and therefore, lesion edges can be preserved while denoising. The results of this algorithm demonstrated for up to 10% applied strain using FEM simulation phantom. It has been shown by the FEM simulation phantom, experimental phantom as well as by the *in vivo* breast data results that the proposed method is robust for a wide range of strain values than the other techniques compared with. It also reveals that the quantitative performance indices, SNRe and CNRe of the strain images can be improved up to approximately 1.5 times, 2.2 times, respectively, than the other algorithms compared with. In addition, the comparative results in terms of the MSSIM using the *in vivo* breast data also show that the strain image quality can be improved up to approximately 1.8 times by the proposed method than the other comparing techniques.

In addition, to overcome the drawbacks of the conventional algorithms where lesion

edges are distorted while ensuring the strain continuity, we have developed a new approach with built-in lesion edge preservation technique for high quality direct average strain imaging. To prevent blurring of the lesion edge while ensuring strain continuity, an intelligent edge preservation criterion is incorporated in the exponential weighting process of the strain determining cost function in such a way that only the NCC peaks corresponding to the neighboring tissue points having similar stiffness to that of the interrogative tissue point are weighted and included into the cost function. A modified edge detection scheme is used to check if a tissue point on a stiffness changing edge or not. The proposed algorithm demonstrates significantly better performance in terms of EMSE than the other reported regularized or average strain estimation techniques in FEM simulation, phantom experiment, and *in vivo* breast data with almost no sacrifice in SNRe and CNRe metrics. For example, The proposed algorithm demonstrates approximately $3.42 \sim 4.25$ dB improvement in terms of EMSE than the other reported regularized or average strain estimation techniques in FEM simulation with almost no sacrifice in the SNRe and CNRe metrics. Moreover, it has been observed that the proposed LEP-DASE method improves the perceptual quality of the strain image, in particular for the *in vivo* patient data, by revealing the natural stiffness variation inside the lesion.

6.2   Future works

In this highly practical field of research, we have tried to develop such processes so that the echo decorrelation, speckle and other forms of noises can be removed with help of the built in filtering scheme of the methods. However, a number of issues remain unanswered and require further study to improve the efficacy of the traditional strain estimation algorithms that are clinically used. Some of these issues are:

- Time delay: The formulation of the time delay t_o in Eqn. (5.2) still produces confusion in window-based strain estimation techniques. This signal model could be revised so that the effect of t_o is properly addressed.

- Inter-window shift: In the window-based strain estimation techniques, the inter-

window shift is considered constant during the estimation of the strain from the displacement field which is not always true. Although, some recent methods have addressed the issue but this problem is yet to be studied in finer scope.

- Tissue models: Early models assumed simple linear isotropic elastic behavior. The appropriateness and limitation of these simple models require further examination, in view of the widespread recognition of the complicated nature of tissues, including nonlinear behavior, hysteresis effects, and complex viscoelastic temporal response.

- Real-time average strain estimation: Although the proposed GBASE method is a near real-time technique, we still need to study further for developing a real-time average strain estimation technique.

List of Publications

Journals

1. **M. A. Hussain**, E. M. A. Anas, S. K. Alam, S. Y. Lee, and M. K. Hasan, "Direct and Gradient Based Average Strain Estimation by Using Weighted Nearest Neighbor Cross-correlation Peaks", *IEEE Transactions on Ultrasonics, Ferroelectrics, and Frequency Control*, vol. 59, no. 8, pp. 1713–1728, 2012.

2. **M. A. Hussain**, S. K. Alam, S. Y. Lee, and M. K. Hasan, "A Robust Strain Estimation Algorithm Using Combined Radio-frequency and Envelope Cross-correlation with Diffusion Filtering", *Ultrasonic Imaging*, vol. 34, pp. 93–109, 2012.

International Conferences

1. **M. A. Hussain**, E. M. A. Anas, S. K. Alam, S. Y. Lee, and M. K. Hasan, "Improved Elasticity Imaging By Maximizing the Weighted Peaks of the Nearest Neighbor Crosscorrelation Function", *2012 American Institution of Ultrasound in Medicine (AIUM) Annual Convention and Preconvention Program*, Phoenix, Arizona, March 29–April 1, 2012.

2. **M. A. Hussain**, S. K. Alam, S. Y. Lee, and M. K. Hasan, "A Robust Strain Estimation Algorithm Using Combined Radio-frequency and Envelope Cross-correlation", *Ultrasonic Imaging and Tissue Characterization Symposium*, Rosslyn, Virginia, June 11–13, 2012.

Submitted Journal

1. **M. A. Hussain**, F. Alam, S. A. Rupa, R. A. Sumi, S. Y. Lee, and M. K. Hasan, "Lesion Edge Preserved Direct Average Strain Estimation for Ultrasound Elasticity Imaging," *Ultrasonics*, 2012.

Bibliography

[1] J. Ophir, E. I. Céspedes, H. Ponnekanti, Y. Yazdi, and X. Li, "Elastography: A quantitative method for imaging the elasticity of biological tissue," *Ultrason. Imaging*, vol. 13, no. 2, pp. 111–134, 1991.

[2] F. Adams (ed.), "The genuine works of Hippocrates," London, UK: Adlard, 1849.

[3] B. S. Garra, E. I. Céspedes, J. Ophir, S. R. Spratt, R. A. Zuurbier, C. M. Magnant, and M. F. Pennanen,"Elastography of breast lesions: initial clinical results," *Radiology*, vol. 202, pp. 79–86, 1997.

[4] T. J. Hall, Y. Zhu, and C. S. Spalding, "*In vivo* realtime freehand palpation imaging," *Ultrasound Med. Biol.*, vol. 29, pp. 427–435, 2003.

[5] A. Itoh, E. Ueno, E. Tohno, H. Kamma, H. Takahashi, T. Shiina, M. Yamakawa, and T. Matsumura, "Breast disease: clinical application of US elastography for diagnosis," *Radiology*, vol. 239, pp. 341–350, 2006.

[6] D. M. Regner, "Breast lesions: evaluation with US strain imagingclinical experience of multiple observers," *Radiology*, vol. 238, pp. 425–437, 2006.

[7] W. E. Svensson and D. Amiras, "Ultrasound elasticity imaging," *Breast Cancer Online* vol. 9, pp. 1–7, 2006.

[8] E. S. Burnside, T. J. Hall, A. M. Sommer, G. K. Hesley, G. A. Sisney, W. E. Svensson, J. P. Fine, J. Jiang, and N. J. Hangiandreou, "Differentiating benign from malignant solid breast masses with US strain imaging." *Radiology*, vol. 245, pp. 401–410, 2007.

[9] N. Miyanaga, H. Akaza, M. Yamakawa, T. Oikawa, N. Sekido, S. Hinotsu, K. Kawai, T. Shimazui, and T. Shiina, "Tissue elasticity imaging for diagnosis of prostate cancer: a preliminary report," *Int. J. Urol.*, vol. 13, pp. 1514–1518, 2006.

[10] R. G. Barr, "Clinical applications of a real time elastography technique in breast imaging," *In Proc. 5th Int. Conf. on Ultrasonic Measurement and Imaging of Tissue Elasticity, Snowbird, UT*, pp. 112, 2006.

[11] C. L. de Korte, E. I. Céspedes, A. F. W. Van der Steen, G. Pasterkamp, and N. Bom, "Intravascular ultrasound elastography: assessment and imaging of elastic properties of diseased arteries and vulnerable plaque, " *Eur. J. Ultrasound*, vol. 7, pp. 219–224, 1998.

[12] C. L. de Korte, G. Pasterkamp, A. F. W. Van der Steen, H. A. Woutman, and N. Bom, "Characterization of plaque components with intravascular ultrasound elastography in human femoral and coronary arteries in vitro," *Circulation*, vol. 102, pp. 617–623, 2000.

[13] S. Y. Emelianov, X. Chen, B. Knipp, and D. Myers, "Triplex ultrasound: elasticity imaging to age deep venous thrombosis," *Ultrasound Med. Biol.*, vol. 28, pp. 757–767, 2002.

[14] M. Vogt and H. Ermert, "Development and evaluation of a high-frequency ultrasound-based system for *in vivo* strain imaging of the skin," *IEEE Trans. Ultrason. Ferroelectr. Freq. Control*, vol. 52, pp. 375–385, 2005.

[15] K. Kaluzynski, X. Chen, S. Y. Emelianov, S. R. Skovoroda, and M. O'Donnell, "Strain rate imaging using two-dimensional speckle tracking," *IEEE Trans. Ultrason. Ferroelectr. Freq. Control*, vol. 48, pp. 1111–1123, 2001.

[16] T. Sugimoto, S. Ueha, and K. Itoh, "Tissue hardness measurement using the radiation force of focused ultrasound," *In Proc. IEEE Ultrasonics Symp., Honolulu, HI*, vol. 3, pp. 1377–1380, 1990.

[17] R. Muthupillai, D. J. Lomas, P. Rossman, J. F. Greenleaf, A. Manduca, and R. L. Ehman, "Magnetic resonance elastography by direct visualization of propagating acoustic strain waves," *Science*, vol. 269, pp. 1854–1857, 1995.

[18] J. Bercoff, M. Tanter, and M. Fink, "Supersonic shear imaging: a new technique for soft tissue elasticity mapping," *IEEE Trans. Ultrason. Ferroelectr. Freq. Control*, vol. 51, pp. 396–409, 2004.

[19] Y.C. Fung, "Biomechanics: mechanical properties of living tissues," *Springer*, 1993.

[20] E. D. Landau and E. M. Lifshitz, "Theory of elasticity," 3rd edn., *Oxford, UK: Pergamon Press*, 1986.

[21] W. Flügge, "Viscoelasticity," 1967.

[22] M .F. Insana, C. Pellot-Barakat, M. Sridhar, and K. K. Lindfors, "Viscoelastic imaging of breast tumor microenvironment with ultrasound.," *J. Mammary Gland. Biol.*, vol. 9, pp. 393–404, 2004.

[23] A. P. Sarvazyan, A. R. Skovoroda, S. Y. Emelianov, J. B. Fowlkes, J. G. Pipe, R. S. Adler, R. B. Buxton, and P. L. Carson, "Biophysical bases of elasticity imaging," *Acoust. Imaging*, vol. 21, pp. 223–240, 1995.

[24] J. F. Greenleaf, M. Fatemi, and M. F. Insana, "Selected methods for imaging elastic properties of biological tissues," *Annu. Rev. Biomed. Eng.*, vol. 5, pp. 57–78, 2003.

[25] R. J. Housden, A. H. Gee, G. M. Treece, and R. W. Prager, "Sub-sample interpolation strategies for sensorless freehand 3D ultrasound," *Ultrasound Med. Biol.*, vol. 32, pp. 1897–1904, 2006.

[26] S. Langeland, J. d'Hooge, H. Torp, B. Bijnens, and P. Suetens, "Comparison of time-domain displacement estimators for two-dimensional RF tracking," *Ultrasound Med. Biol.*, vol. 29, pp. 1177–1186, 2003.

[27] F. Viola and W. F. Walker, "A comparison of the performance of time-delay estimators in medical ultrasound," *IEEE Trans. Ultrason. Ferroelectr. Freq. Control*, vol. 50, pp. 392–401, 2003.

[28] M. Bilgen and M. F. Insana, "Deformation models and correlation analysis in elastography," *J. Acous. Soc. America*, vol. 99, no. 5, pp. 3212–3224, 1996.

[29] L. N. Bohs and G. E Trahey, "A novel method for angle independent ultrasonic imaging of blood flow and tissue motion," *IEEE Trans. Biomed. Eng.*, vol. 38, pp. 280–286, 1991.

[30] P. Chaturvedi, M. F. Insana, and T. J. Hall, "Testing the limitations of 2-D companding for strain imaging using phantoms," *IEEE Trans. Ultrason. Ferroelectr. Freq. Control*, vol. 45, pp. 1022–1031, 1998.

[31] F. Yeung, S. F. Levinson, and K. J. Parker, "Multilevel and motion model-based ultrasonic speckle tracking algorithms," *Ultrasound Med. Biol.*, vol. 24, pp. 427–441, 1998.

[32] M. O'Donnell, A. R. Skovoroda, B. M. Shapo, and S. Y. Emelianov, "Internal displacement and strain imaging using ultrasonic speckle tracking," *IEEE Trans. Ultrason. Ferroelectr. Freq. Control*, vol. 41, pp. 314–325, 1994.

[33] A. Pesavento, C. Perrey, M. Krueger, and H. Ermert, "A time efficient and accurate strain estimation concept for ultrasonic elastography using iterative phase zero estimation," *IEEE Trans. Ultrason. Ferroelectr. Freq. Control*, vol. 46, pp. 1057–1067, 1999.

[34] X. Chen, M. J. Zohdy, S. Y. Emelianov, and M. O'Donnell, "Lateral speckle tracking using synthetic lateral phase," *IEEE Trans. Ultrason. Ferroelectr. Freq. Control*, vol. 51, pp. 540–550, 2004.

[35] J. E. Lindop, G. M. Treece, A. H. Gee, and R. W. Prager, "Phase-based ultrasonic deformation estimation," *IEEE Trans. Ultrason. Ferroelectr. Freq. Control*, vol. 55, pp. 94–111, 2008.

[36] S. K. Alam, J. Ophir, and E. E. Konofagou, "An adaptive strain estimator for elastography," *IEEE Trans Ultrason. Ferroelectr. Freq. Control*, vol. 45, pp. 461–472, 1998.

[37] G. M. Treece, J. E. Lindop, A. H. Gee, and R. W. Prager, "Freehand ultrasound elastography with a 3-D probe," *Ultrasound Med. Biol.*, vol. 34, pp. 463–474, 2008.

[38] R. J. Dickinson and C. R. Hill, "Measurement of soft tissue motion using correlation between A-scans," *Ultrasound Med. Biol.*, vol. 8, pp. 263–271, 1982.

[39] H. Rivaz, E. Boctor, P. Foroughi, R. Zellars, G. Fichtinger, and G. Hager, "Ultrasound elastography: A dynamic programming approach," *IEEE Trans. Med. Imaging*, vol. 27, no. 10, pp. 1373–1377, 2008.

[40] C. Pellot-Baraka, F. Frouin, M. F. Insana, and A. Herment, "Ultrasound elastography based on multiscale estimations of regularized displacement fields," *IEEE Trans. Med. Imaging*, vol. 23, no. 2, pp. 153–163, 2004.

[41] R. Zahiri-Azar and S. E. Salcudean, "Motion estimation in ultrasound images using time domain cross correlation with prior estimates," *IEEE Trans. Biomed. Engg.*, vol. 53, no. 10, pp. 1990–2000, 2006.

[42] S. K. Alam and J. Ophir, "Reduction of signal decorrelation from mechanical compression of tissues by temporal stretching-applications to elastography," *Ultrasound Med. Biol.*, vol. 23, no. 1, pp. 95–105, 1997.

[43] J. E. Lindop, G. M. Treece, A. H. Gee, and R. W. Prager, "Estimation of displacement location for enhanced strain imaging," *IEEE Trans. Ultrason. Ferroelectr. Freq. Control*, vol. 54, pp. 1751–1771, 2007.

[44] J. Ophir, E. I. Céspedes, B. S. Garra, H. Ponnekanti, Y. Huanga, and N. Maklad, "Elastography: Ultrasonic imaging of tissue strain and elastic modulus in vivo," *Eur. J. Ultrasound*, vol. 3, no. 1 pp. 49–70, 1996.

[45] E. I. Céspedes, J. Ophir, H. Ponnekanti, and N. Maklad, "Elastography: Elasticity imaging using ultrasound with application to muscle and breast in vivo," *Ultrason. Imaging*, vol. 15, no. 2, pp. 73–88, 1993.

[46] J. Ophir, S. K. Alam, B. S. Garra, F. Kallel, E. E. Konofagou, T. Krouskop, C. R. B. Merritt, R. Righetti, R. Souchon, S. Srinivasan, and T. Varghese, "Elastography: Imaging the elastic properties of soft tissues with ultrasound," *J. Med. Ultrasound*, vol. 29, pp. 155–171, 2002.

[47] S. K. Alam, "Novel spline-based approach for robust strain estimation in elastography," *Ultrason. Imaging*, vol. 32, no. 2, pp. 91–102, 2010.

[48] J. Ophir, S. K. Alam, B. S. Garra, F. Kallel, E. E. Konofagou, T. Krouskop, and T. Varghese, "Elastography: Ultrasonic estimation and imaging of the elastic properties of tissues," in *Proc. of the Instit. of Mechanical Engineers*, Part H: *J. Engg. Medicine*, vol. 213, no. 3, pp. 203–233, 1999.

[49] T. Varghese, E. E. Konofagou, J. Ophir, S. K. Alam, and M. Bilgen, "Direct strain estimation in elastography using spectral cross-correlation," *Ultrasound Med. Biol.*, vol. 26, no. 9, pp. 1525–1537, 2000.

[50] S. K. Alam, F. L. Lizzi, T. Varghese, E. J. Feleppa, and S. Ramachandran, "Adaptive spectral strain estimators for elastography," *Ultrason. Imaging*, vol. 26, no. 3, pp. 131–49, 2004.

[51] U. Techavipoo and T. Varghese, "Wavelet denoising of displacement estimates in elastography." *Ultrasound Med. Biol.*, vol. 30, no. 4, pp. 477–491, 2004.

[52] F. Kallel and J. Ophir, "A least-squares strain estimator for elastography," *Ultrason. Imaging*, vol. 19, no. 3, pp. 195–208, 1997.

[53] H. Rivaz, E. M. Boctor, M. A. Choti, and G. D. Hager, "Real-time regularized ultrasound elastography," *IEEE Trans. Med. Imaging*, vol. 30, no. 4, pp. 928–945, 2011.

[54] E. E. Konofagou, T. Varghese, J. Ophir, and S. K. Alam, "Power spectral strain estimators in elastography," *Ultrasound Med. Biol.*, vol. 25, no. 7, pp. 1115–1129, 1999.

[55] T. Varghese and J. Ophir, "Characterization of elastographic noise using the envelope of echo signals". *Ultras. Med. and Biol.*, vol. 24, no. 4, pp. 543–555, 1998.

[56] L. Chen, R. J. Housden, G. M. Treece, A. H. Gee, and R. W. Prager, "A hybrid displacement estimation method for ultrasonic elasticity imaging", *IEEE Trans Ultrason Ferroelectr Freq Control.*, vol. 57, no. 4, pp. 866–882, 2010.

[57] H. Shi and T. Varghese, "Two-dimensional multi-level strain estimation for discontinuous tissue." *Phys Med Biol.*, vo. 52, no. 2, pp. 389–401, 2007.

[58] T. Shiina, M. M. Doyley, and J. C. Bamber, "Strain imaging using combined RF and envelope autocorrelation processing," *IEEE Ultrasonics Symposium*, pp. 1331–1336, 1996.

[59] M. Friedrich-Rust, M. F. Ong, and E. Herrmann, "Real-time elastography for non-invasive assessment of liver fibrosis in chronic viral hepatitis," *Amer. J. Roentgen*, vol. 18, no. 8, pp. 758–764, 2006.

[60] C. L. Korte, A. F. W. Van-der-Steen, "Intravascular ultrasound elastography: an overview", *Ultrasonics*, vol. 40, pp. 859–865, 2002.

[61] B. Pan, K. Qian, H. Xie, and A. Asundi, "Two-dimensional digital image correlation for in-plane displacement and strain measurement: a review," *Meas. Sci. Technol.*, vol. 20, 062001, 2009.

[62] K. Hoyt, F. Forsberg, and J. Ophir, "Analysis of a hybrid spectral strain estimation technique in elastography," *Physics In Medicine And Biology*, vol. 51, pp. 197–209, 2006.

[63] T. Shiina, M. Yamakawa, N. Nitta, and E. Ueno, "Real Time tissue Elasticity Imaging Using the Combined Autocorreltion Method," *J. Med. Ultrasonics*, vol. 29, pp. 119–128, 2002.

[64] E. I. Céspedes and J Ophir "Reduction of image noise in elastography," *Ultrason. Imaging*, vol. 15, no. 2, pp. 89–102, 1993.

[65] T. Varghese and J. Ophir, "An analysis of elastographic contrast-to-noise ratio performance," *Ultrasound Med. Biol.*, vol. 24, no. 6, pp. 915–924, 1998.

[66] Z. Wang, A. C. Bovik, H. R. Sheikh, and E. P. Simoncelli, "Image quality assessment: From error visibility to structural similarity," *IEEE Trans. Image Processing*, vol. 13, no. 4, pp. 600–612, 2004.

[67] M. K. Hasan, E. M. A. Anas, S. K. Alam, and S. Y. Lee, "Direct Mean Strain Estimation for Elastography Using Nearest-Neighbor Weighted Least-Squares Approach in the Frequency Domain," *Ultras. Med. Biol.*, vol. 38, no. 10, pp. 1759–1777, 2012.

[68] S. Cui, C. Peng, X. Chen, X. Liu, Y. Yu, and Q. Wang, "Ultrasound elastography performance enhancment using wavelet denoising," *Int. confer. on Audio Lang. and Image Pro. (ICALIP)*, pp. 1238–1243, 2010.

[69] T. A. Krouskop, T. M. Wheeler, F Kallel,B. S. Garra, and T. Hall. "Elastic moduli of breast and prostate tissues under compression." *Ultrason. Imaging.*, vol. 20, no. 4, pp. 260–274, 1998.

[70] M. A. Hussain, E. M. A. Anas, S. K. Alam, S. Y. Lee, and M. K. Hasan, "Direct and gradient-based average strain estimation by using weighted nearest neighbor cross-correlation peaks," *IEEE Trans. Ultrason. Ferroelect. Freq. Control*, vol. 59, no. 8, pp. 1713–1728, 2012.

[71] E. Michel-Gonzjález, M. H. Cho, and S. Y. Lee, "Geometric nonlinear diffusion filter and its application to X-ray imaging," *BioMed. Engineering OnLine*, vol. 10, 2011.

[72] E. Brusseau, C. Perrey, P. Delachartre, M. Vogt, D. Vray, and H. Ermert, "Axial starin imaging using local estimation of the scaling factor from RF ultrasound signals," *Ultrason. Imag.*, vol. 22, pp. 95–107, 2000.

[73] M. J. Black, G. Sapiro, D. Marimont, and D. Heeger, "Robust anisotropic diffusion," *IEEE Trans. Image Process.*, vol. 7, pp. 421–432, 1998.

[74] J. A. Jensen, "Field: A program for simulating ultrasound systems," *In: 10th Nordicbaltic Conf. on Biomed. Imag.*, vol. 4, pp. 351–353, 1996.